The Feshbach resonances of the two-body 23Na6Li system

Haverhals, M.M.

Award date:
2012

The Feshbach resonances of the two-body ^{23}Na^{6}Li system

Maartje Maria Haverhals

Master's thesis

Supervisors: dr.ir. S.J.J.M.F. Kokkelmans
dr.ir. M.R. Goosen

Technische Universiteit Eindhoven
Department Applied Physics
Coherence and Quantum Technology Group

Eindhoven, December 2011

Abstract

The study presented in this thesis is made to explain the Feshbach resonance spectrum of the ultracold $^{23}Na^{6}Li$ system with the use of the Asymptotic Bound-state Model (ABM). This work was done in collaboration with the university of Heidelberg, where the group of prof. Oberthaler studied the system experimentally.
Earlier publications of the $^{23}Na^{6}Li$ mixture show an interpretation of the spectrum based on three magnetically induced Feshbach resonances.[1,2] The interpretation was proven to be incorrect, when the measured spectrum was increased to 24 resonances. The large set of measured resonances gives the opportunity to firmly analyze the system.

Magnetically induced Feshbach resonances are collisional resonances caused by bound states in the interatomic potential, which can be made resonant with the collision threshold by changing the magnetic field. These resonances give the opportunity to control the atomic interactions in an ultracold quantum gas. One of the great properties of Feshbach resonances is the tune-ability of the interaction strength. The system can be magnetically tuned to be attractive, repulsive or even non-interacting and it is even possible to control the conversion of atoms to ultracold molecules and vice versa.

The measured Feshbach resonance spectrum is analyzed based on the Asymptotic Bound-state Model, with this model the resonance positions can be determined by only using the least bound state energies, instead of full radial potential curves.
The analysis of the system is made as follows: first the internal energy of the two atoms is determined as function of an external magnetic field, and second, this is complemented by adding the interatomic interaction, which in principle is a function of the internuclear separation. An accurate description of the central interatomic potential was not available. However a publication by Fellows et al.[3], gives the values for the potential curve at long range and data from which a not very accurately potential at short range could be obtained. The information was used to construct the whole potential curve.
In order to improve the accuracy of the interactions, free parameters have been introduced. These parameters shift the bound state energies in the interatomic potential.
In the end, the model has three free input parameters for which we determine the corresponding resonance positions. The main task was to find those three input parameters for which the model calculates the resonances at the same location as is measured. Not only the positions are described by the system, also the width of the resonances can be obtained from the total Hamiltonian.

After writing the model for the $^{23}Na^{6}Li$ system, the influence of the input parameters was examined on the resonance position output. As a result the solution space could be reduced. In the reduced solution space, two sets of measured resonances were carefully examined and their results combined.
Finally, two different scenario's were obtained, which both can explain the measured resonance spectrum. In both cases the results could be improved by using additional correction factors which are related to the long-range part of the potential. Both the solutions have pro's and con's in explaining the spectrum, therefore it is hard to determine to which one describes reality best.
Some resonances are identified by the scenario's originating from partial p-waves. So far the experiment has not been able to discriminate between s- and p-wave Feshbach resonances. However, a careful experimental investigation should be able to see the difference. If this is possible, the results could be compared and it would be easy to verify which scenario is best.

Contents

Chapter 1

Introduction: Feshbach resonances in a nutshell

The study presented in this thesis is made in collaboration with the university of Heidelberg. In the group of Prof. Oberthaler, magnetically induced Feshbach resonances were observed in the ultracold ^{23}Na^{6}Li system. The measured resonances do not match the predictions made in the earlier publications by Gacesa et al.[2] and Stan et al[1]. These predictions were based on the observation of three resonances. The group of Prof. Oberthaler was able to increase the spectrum to 24 resonances, which disagrees with the earlier predictions but also gives a new opportunity to analyze the system. This analyze is the aim of my graduation project.
The interpretation of the data and predictions of new resonances are based on the Asymptotic Bound-state model (ABM)[4], which has several advantages with respect to the numerical Coupled-Channels calculation of Gacesa et al.

1.1 Feshbach resonances

Before turning to the ^{23}Na^{6}Li system, we focus first on the phenomenon Feshbach resonances. Magnetically induced Feshbach resonances are collision resonances caused by bound states in the interatomic potential, which can be made resonant with the collision threshold by changing the magnetic field.
Feshbach resonances occur under ultracold circumstances, typically by temperatures in the range of nanokelvin to microkelvin with densities between the 10^{12} and 10^{15} atoms cm^{-3}. Under these circumstances the thermal de Broglie wavelength will exceed the typical interparticle distance. Consequently the system can no longer be described by classical physics and should be treated wave-like, according to quantum mechanics.[5, 6]

The potential energy of the two atoms can be divided into an interatomic interaction and an internal single-atom part. The interatomic (or central) interaction potential depends on the atomic separation r. At short range a potential well arises, which makes the existence of bound states possible.
The internal energy of the atoms is the sum of hyperfine and Zeeman interactions, determined by their set of spin quantum numbers and an eventual external magnetic field,

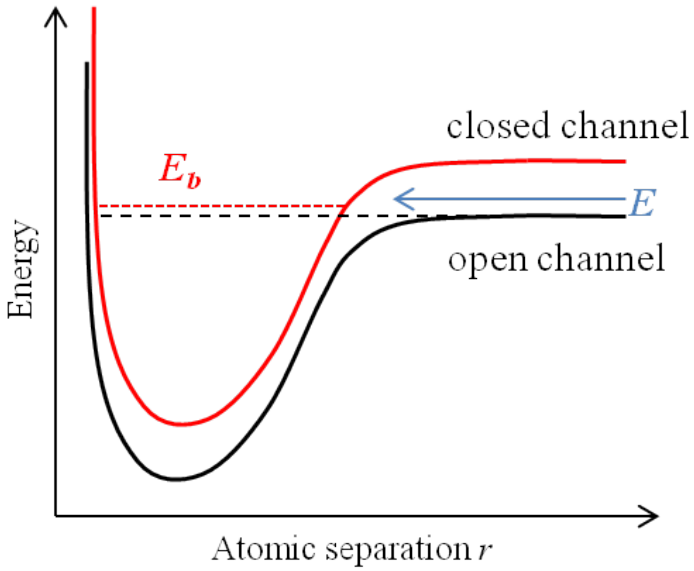

Figure 1.1: Schematic overview of a Feshbach resonance; the scatter state with energy E of the open channel (black curve) can be resonantly coupled to the bound state (energy E_b) of the closed channel as both energies approach the same value. The E_b can be vertically shifted with respect to the threshold of the open channel (black dashed line) by tuning the external magnetic field.

however it is independent of r. Due to the discrete set of possible quantum numbers, the internal energy has only a discrete set of possible energies. As result, the summation of the internal part with the interaction potential gives rise to a discrete set of potential energy curves as function of r. Each of those potential curves correspond to a channel, which is indicated by the spin quantum numbers of the atoms. Two potential curves corresponding to two different channels are drawn in figure 1.1. The relative vertical distance between the channels can be tuned by the presence of a magnetic field.
The asymptotic behavior of the potential curves, r to infinity, is defined as the threshold and is the minimum energy of two free particles in the corresponding channel (the black dashed line in the figure). The total energy of the two atoms E divides the channels into two categories. The channels which have their threshold below E are called the open channels and the channels which have their threshold above E are said to be energetically closed.
A Feshbach resonance occurs as the two particles scatter in the open (or entrance) channel and couple resonantly to a bound state of the closed channel. In other words, the system becomes resonant as the energy of the scattering atoms E is close to the molecular bound state energy E_b. The system can be tuned to resonant or non-resonant, by adjusting the external magnetic field and hence the position of the closed bound state with respect to the open channel.

As the system becomes resonant the scattering length will diverge and goes to infinity, this is shown in figure 1.2. The scattering length a is a measure of the interaction strength. Its value can be magnetically tuned in such a way, that the interaction is repulsive ($a > 0$),

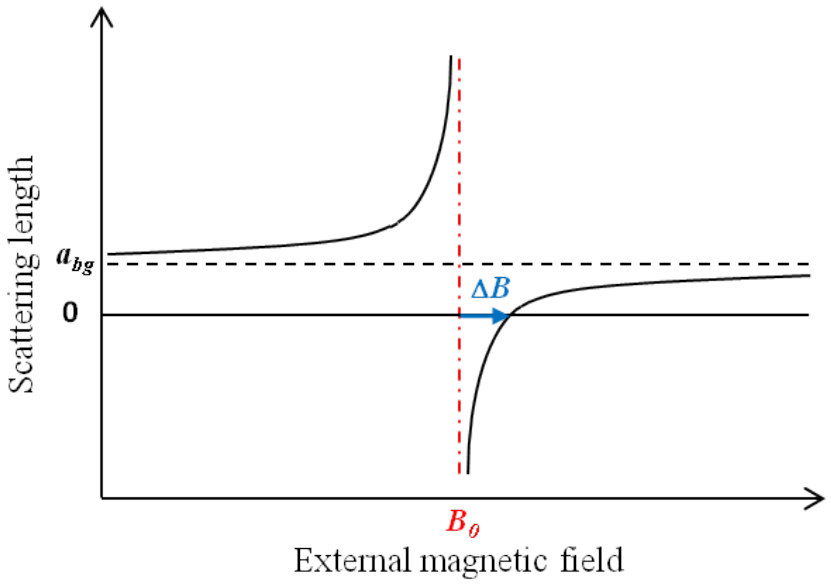

Figure 1.2: The scattering length versus the external magnetic field. As the external magnetic field approaches a Feshbach resonance (B_0), the scattering length will diverge. The width of the resonance ΔB is given by the blue arrow.

attractive ($a < 0$) or non-interactive ($a = 0$).[4] This gives a large control over the atomic interactions, and practically any value for a can be obtained.
The development of the scattering length around a resonance is characterized by the magnetic field width ΔB (indicated by the blue arrow). The field width is defined as the distance between B_0 and the magnetic field at $a(B) = 0$.[5] The broader the width the more spread out the resonance development over the magnetic field range. In other words, the field width is a measure for the Feshbach resonance width.

Observing Feshbach resonances
In the group of prof. Oberthaler, the ultracold ^{23}Na^{6}Li atomic gas is prepared in a particular entrance channel. The atomic loss is then carefully recorded as function of the magnetic field. If the magnetic field crosses a Feshbach resonance, the atomic gas is in resonant with the molecular state and therefore the number of atoms reduces. Near a resonance the atom loss is enhanced by inelastic losses, mainly the three-body recombination which scales strongly with a. The three-body recombination is the three body collision which results in one free atom and a diatomic molecule.[5,7]
The atomic loss is determined, by ramping the magnetic field to a certain value B, where the magnetic field is held constant over a hold time. The system is then ramped back to zero magnetic field, after which the remaining atoms are measured. The ramp times are taken much shorter then the hold times. By repeating this process, the whole channel can be scanned for resonances.

The position of the Feshbach resonances can also be determined theoretically by the

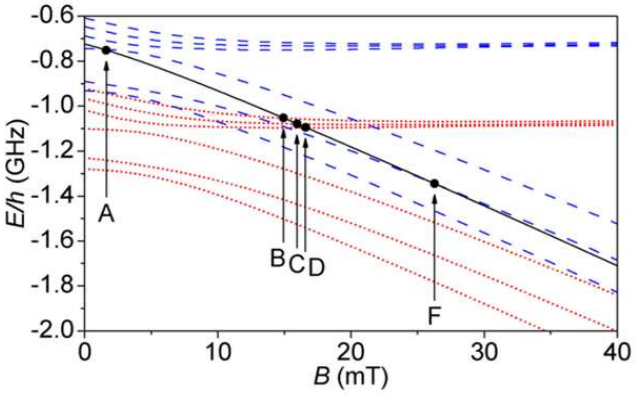

Figure 1.3: The resonances of two body $^{6}Li^{40}K$ system. The measured resonances are shown by the black dots. The black line represents the threshold, the red and blue dashed lines are the bound state energies. The resonances gained by ABM, are predicted where the bound state energies cross the threshold. This figure is obtained from a publication by E. Wille et al.[8].

Coupled Channels (CC) method. The results of this method are numerically very accurate. However this method makes use of the full interaction potentials, which are in most cases not very precisely known. One needs, in order to get better potentials, to improve them with suitably chosen potential parameters. This method can be very time consuming, in particular when the interaction potentials are bad.[4] Another drawback of this method is its complexity, through which the overview is easily lost and features of the resonance spectrum could be missed. Therefore this method is often used to only verify the final results of a simplified model.
In the case of the $^{23}Na^{6}Li$ system, the interatomic potential is not accurately known. Therefore it is desired to use a more simplified model than the CC method. In this research the Asymptotic Bound-state model is used. In the model, only the least bound states of the potentials are taken into account. This model allows a clear insight in the resonance spectrum with fast computational times.[4]
The ABM model has proven itself to be very useful in many cases. One example is the $^{6}Li^{40}K$ system, where 13 measured resonances where successful interpreted. Due to the elegant simplicity of the model, the assignments of experimental to theoretically resonances was done with only three parameters. The result is shown in figure 1.3 obtained from E.Wille et al.[8] where the black dots represent the measured resonances and the blue en red crossings with the black threshold, give the theoretically resonances.

1.2 Why the interest?

When the magnetic field is swept across a Feshbach resonance, the atoms can be converted to molecules. This is shown in figure 1.4, where free atoms in the entrance channel adiabatically turn into a molecular bound state by sweeping down the external magnetic field. The molecules formed by Feshbach resonances are called Feshbach molecules.[6]

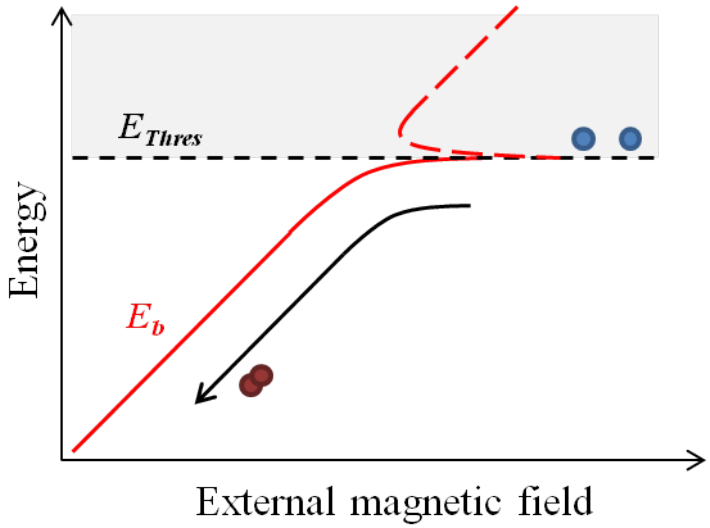

Figure 1.4: The adiabatically conversion from an atomic state into a moleculair bound state. Based on a figure shown in *Ultracold atoms, theory, Experiment, Applications*[9].

The particles that make up the Feshbach molecules can be divided into two species, the bosons and the fermions. The two species have different degenerate statistics. The bosons are allowed to be all in the same state, however fermions are forbidden to share states due to the Pauli exclusion principle. Under the ultracold circumstances the atoms will be in the lowest energy state possible, the bosons degenerate to the lowest energy state (Bose Einstein Condensation) and the fermions fill all the lowest available energy states one by one (according to the Fermi-Dirac distribution).[6,10] If we stick to the two-particle physics there are three possible combinations for the atomic mixtures, namely boson-boson, fermion-fermion and boson-fermion. The first two atomic combinations lead to molecular bosons, the third combination encounters for molecular fermions.[9] As result the ultracold atomic gas containing a boson-boson or fermion-fermion mixture could lead to a molecular BEC. In the first case one is able to switch between atomic and molecular BEC. In the second case, the atomic fermi gas has an other property, the system is able to switch between BSC (Bardeen- Cooper-Schrieffer) paring of fermions to the molecular Bose Einstein Condensate.[5]
So far, a lot of scientific attention was directed to the Feshbach resonances induced by the same species. More recently the attention is turned to the Bose-Fermi mixtures. These mixtures could lead to new phenomena, predictions are recorded such as boson-mediated Cooper pairing, phase separation and supersolid order.[1] This study is made to contribute to the scientific exploring of the properties Bose-Fermi mixtures.

The switching between the molecular and atomic state is not the only fascinating property of the Feshbach resonances, there is also tune ability of the interaction strength. For example it is possible to tune an unstable BEC to stable and vice versa. The first stable molecular BEC was obtained by the use of Feshbach resonances.[6] Another advantage of Feshbach resonances is due to the comparison between experiment and theory, which can lead to a more accurate description of the interatomic potential.[1,5]

In short the great properties of Feshbach resonances give the opportunity to couple and even switch between atom and molecular condensates, tuning the interaction strength of a quantum gas and fine-tune the interactomic potential.

1.3 Outline

The main goal of this thesis is to analyze and understand the measured ^{6}Li^{23}Na Feshbach resonances from Heidelberg. The basis of interpreting the data is set by the Asymptotic Bound-state model. In order to use this model, the potential energy of the system as function of the magnetic field is required. The potential energy can be divided by the internal and atomic interaction part. The internal energy is studied in chapter 2, where the total internal energy is the sum of the individual energies of the two non-interacting atoms. The next step is to examine the interatomic interaction, which are the potential curves that rise to the presence of bound states. The construction of the singlet potential and the relation between relative bound states is described in chapter 3. As the available interaction potential is not very accurate, we discuss two free potential parameters which vary the positions of the bound states in the potential. In this chapter also the background scattering length as function of these two free parameters is discussed.
So in chapter 2 and 3, all the necessary ingredients to obtain the Feshbach resonance positions are given. In chapter 4 all this information is combined. First the total Hamiltonian is examined, from which the binding energies of the system can be determined. The interaction of the binding energies and the threshold, result in the theoretical resonance positions as function of the free fit parameters. In the end we obtain three free parameters, with which the model can be adjusted to fit the measured resonance spectrum. In order to make the assignment of the theoretical to the measured resonances more manageable, one can divide the system according to its conserved quantum numbers (section 4.2). Together with the positions, the field width ΔB can also be obtained from the total Hamiltonian. The field width is discussed in the last section of chapter 4, where an expression for the ΔB is derived.
In chapter 5, the theoretical values are fitted to the measured values in order to understand the ^{6}Li^{23}Na interactions and finally we will discuss the results of this thesis.

Chapter 2

The non-interacting particles

Feshbach resonances occur at the border between bound and unbound particles. In this chapter the unbound or free particles are discussed when infinitely far separated from one another, which are therefore effectively non-interacting particles.
Both ^{6}Li and ^{23}Na are alkali-metal atoms, which are both considered to be in their electronic ground state. The atoms have one valence electron which has a spin $s = 1/2$ and a nucleus spin i with the value $i = 1$ for ^{6}Li and $i = 3/2$ for ^{23}Na. The total angular momentum of an atom is given by $\vec{f} = \vec{s} + \vec{i}$, where $\vec{s}$ is the quantized intrinsic angular momentum of the valence electron and $\vec{i}$ of the nucleus.

Each intrinsic angular momentum results in a magnetic dipole, which sets up a magnetic field. The interaction between the spin of the electron or nucleus and the induced magnetic field is called the spin-spin coupling. The potential energy caused by the spin-spin interaction of an atom labeled by j can be written as

$$E_j^{hf} = \frac{a_j^{hf}}{\hbar^2} \vec{s_j} \cdot \vec{i_j}, \tag{2.1}$$

$$= \frac{a_j^{hf}}{\hbar^2} \frac{\hbar^2}{2} \left(f_j(f_j+1) - i_j(i_j+1) - s_j(s_j+1) \right), \tag{2.2}$$

where a_j^{hf}/h is the hyperfine constant and has the value 152.1368407 MHz for ^{6}Li and 885.813 MHz for ^{23}Na.[2] For alkali atoms f_j has two possible values, namely $f_j = i_j \pm 1/2$. As a consequence the potential energy due to the spin-spin interaction results into two discrete values, the hyperfine splitting.
In a closed system the total angular momentum is conserved, because there is no net force. In this case, the internal state of the atom is defined by $|f, m_f\rangle$. Each hyperfine manifold is $(2f_j + 1)$-fold degenerate due to m_f. The magnetic quantum number m_f is the quantized projection of f for any given direction. However if there is an external magnetic field, the $|f, m_f\rangle$ combinations are not adequate anymore to label the eigenstates.[10, 11]

If an atom is placed into an uniform magnetic field, the interaction of the spins with the external magnetic field results in the Zeeman energy. The Zeeman energy is given by 2.3.

$$E_j^Z = \left(\gamma_{e,j}\vec{s_j} - \gamma_{n,j}\vec{i_j}\right) \cdot \vec{B}, \tag{2.3}$$

$$= \hbar \left(\gamma_{e,j} m_{s,j} - \gamma_{n,j} m_{i,j}\right) B, \tag{2.4}$$

where $\gamma_{e,j}$ and $\gamma_{n,j}$ are the electron and nuclear gyromagnetic ratios of atom j, which have the values $\gamma_{e,Na} = \gamma_{e,Li} = 1.760859770 \cdot 10^{11}$, $\gamma_{n,Li} = 3.9367 \cdot 10^7$ and $\gamma_{n,Na} = 7.075 \cdot 10^7$ rad s^{-1} T^{-1}.[10,12]

The internal energies for different external magnetic fields are given by the eigenvalues of internal Hamiltonian, which for ^{6}Li and ^{23}Na are shown in figure 2. The total internal Hamiltonian is the combination of the hyperfine and the Zeeman interactions given by the

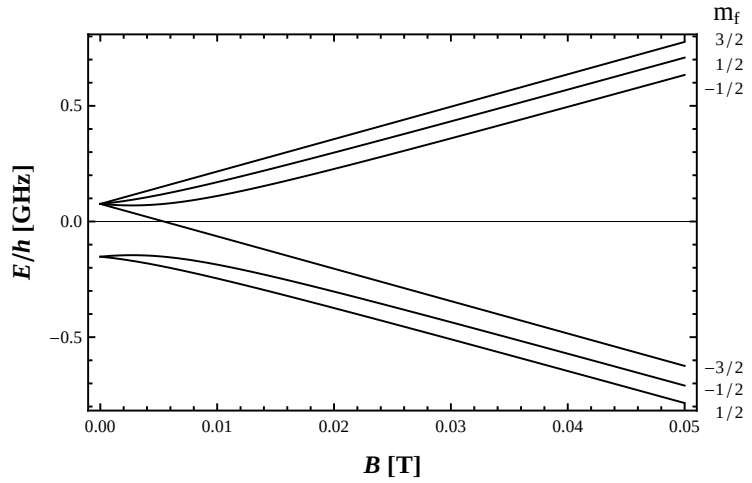

(a)

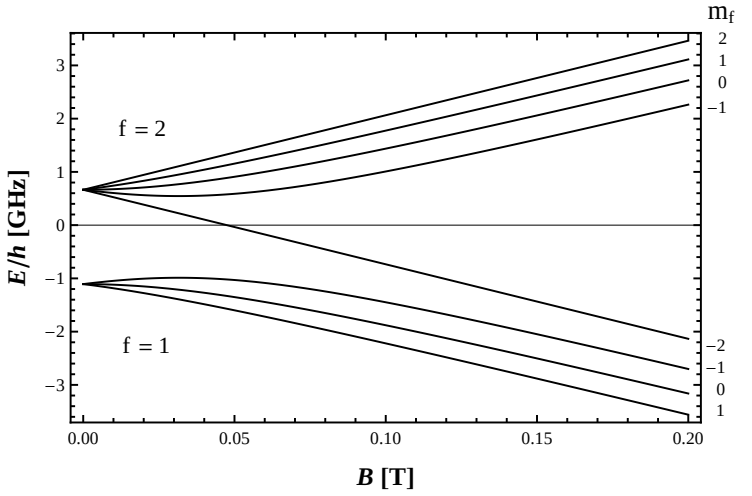

(b)

Figure 2.1: The eigenvalues of the internal Hamiltonian for the non-interacting particles ^{6}Li (a) and ^{23}Na (b).

equations 2.1 and 2.3. The eigenstates are labeled with $|f, m_f\rangle$ which as mentioned before is only correct at $B = 0$, however these labels still indicate where the eigenvalues originates from.

To obtain the total internal energy of the two non-interacting particles, the separate internal energies can be simply added.

Chapter 3

The central interaction between the ^{23}Na and ^{6}Li particles

3.1 The central interatomic interaction

As the separate atoms are able to approach each other, it is no longer correct to consider them as non-interacting particles; therefore the interatomic interaction needs to be considered as well. For structureless atoms this interaction will depend only on the relative distance r between atoms, which is described by the central potential $V_C(r)$ and will be later further explored.
The relative two-body system can be represented by the radial wavefunction $R(r)$. The wavefunction can be obtained by solving the time-independent radial Schrödinger equation. The radial wavefunction $R(r)$ can be replaced by $\psi(r) \equiv rR(r)$; for which the Schrödinger equation holds,

$$-\frac{\hbar^2}{2\mu}\frac{d^2\psi_{S,l}}{dr^2} + \left[V_C(r) + \frac{\hbar^2}{2\mu}\frac{l(l+1)}{r^2}\right]\psi_{S,l} = \epsilon_{S,l}\psi_{S,l} \tag{3.1}$$

where the quantum numbers S and l are respectively the total electron spin and the orbital angular momentum, μ the reduced mass and $\epsilon_{S,l}$ the relative energy. The expression between the square brackets defines the effective potential which consists of the central potential and the centrifugal term. The reduced radial wavefunction $\psi(r)$ will from now on simply referred to as the wavefunction.

The central potential is crucial in solving the Schrödinger equation, which is examined in this section and forms the basis for the rest of this chapter. The potential energy curve of two interacting particles can be divided into a short and a long range part. Dependent on the internuclear separation, different physical interactions dominate. For the short range the most dominant are the coulomb interaction between the nuclei of the atoms and the exchange interaction between the electron spins. When the internuclear separation becomes larger, the coulomb interaction will have less influence and the overlap between the electron clouds will reduce. Then the electric dipole/multipole moment of each atom induced by the other becomes of large importance, also known as the dispersion forces. As a result the potential energy curve at small internuclear distances is repulsive, as the separation becomes larger the attractive forces dominate and for even larger distances the interaction between

the particles becomes negligible.
In short, as function of the relative distance r the potential curve switches from repulsive to attractive and from attractive to none interacting, forming a potential well in the attractive range.[10, 13]

The potential curve of the two-body $^{23}Na^{6}Li$ system is not 'ready-made' available. However the information to gain the curve was published by C.E. Fellows[3]. C.E. Fellows recon-

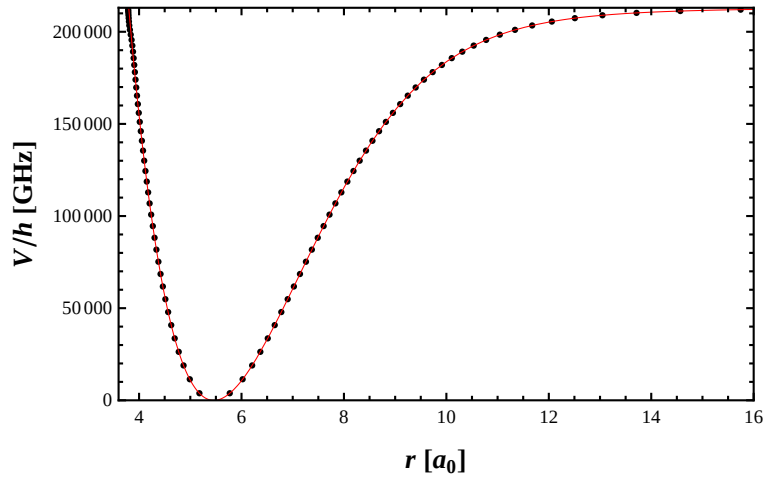

(a) Potential curve

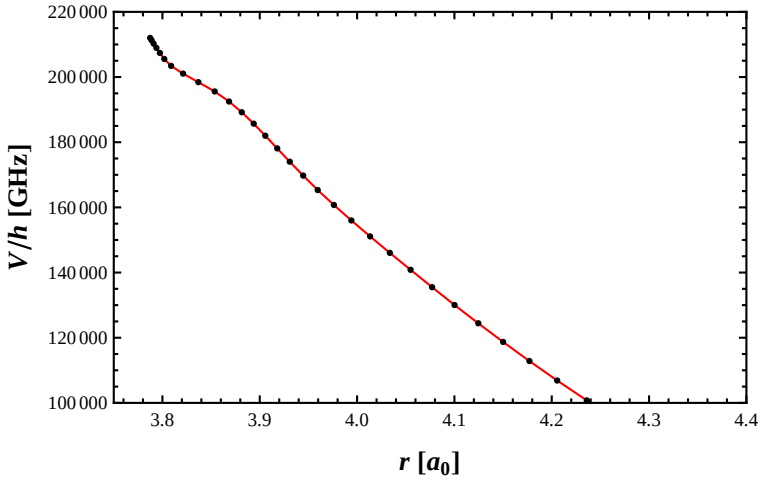

(b) Left side of the potential well

Figure 3.1: Energy levels of different vibrational quantum numbers in the electronic ground state in combination with their maximum and minimum classical turning points (a) and the interpolated data points from left side of the potential well (b).

structs the potential using the energy levels of different vibrational quantum numbers in the electronic ground state. The classical turning points, belonging to each energy level, give shape to the potential curve which is shown in figure 3.1 (a). Through this data a fit

was made, from which the potential at long range was obtained ($r > 11.5$ a_0). The information of the long range potential was published, however a description of the short range ($r < 11.5$ a_0) was not.

For this research the whole potential is needed and not, as first participated, only the long range part; the reason for this will be discussed in the last section of this chapter. The long range potential fit made by C.E. Fellows needs to be expanded for short internuclear distances. The short range is to be constructed by an interpolation curve through the vibrational data points, which make up the potential well and is extrapolated for even smaller distances where no data points were obtained. In the end the extrapolation (short distances), the interpolation (potential well) and the long range fit needs to be 'glued' together.

The short range

Figure 3.1(a) shows the vibrational data points that make up the potential well. The lowest potential energy value in the well is set to zero. The second graph, figure 3.1(b), shows the (joined) data points for small values of r, i.e. the left side of the well. Those data points do not form a nice smooth curve and one should therefore be cautious when constructing the potential curve for even smaller values of r. The fluctuation is examined using the gradient of the inner potential side, which is shown in figure 3.2(a). The gradient increases gradually for internuclear distances larger than 4.15 a_0, for smaller values of r a fluctuation in the gradient appears. The fluctuation is probably caused by the inaccuracy of the measurement. In order to avoid the influence of the fluctuation on the potential curve, the data points till 4.15 a_0 do not qualify for the reconstruction of the short range potential. Through all the remaining data points a fit is made, which is extrapolated to construct the left side of the potential well for r smaller than 4.15 a_0. Figure 3.2(b) shows the result, the purple data points are the ones used for the fit and the red line is the resulting short range potential curve. Probably one would wonder if it is legal to simply erase data points and insert new ones. The influence of alternating the curve is checked and presented in appendix A. In this appendix it is justified that for the purpose of this report, the made corrections are valid.

The long range

The short range potential is now constructed and only needs to be coupled to the long range part. In the paper of C.E. Fellows[3], two long range fit scenarios are examined, case a and b. The difference between the two cases, is the internuclear separation range used for the fits. For the purpose of this report both cases will do, however case b leaves room for the possibility that exchange energy term is mixed with the higher-order van der Waals terms. As a result, case a is chosen to be used as it would give a better description of the different fit terms. For the long range potential fit the dispersion and the exchange interaction are taken into account, the last interaction needs to be taken negative as the potential is fitted by the singlet spin configuration. The long range potential is given by

$$V_{Long} = D_e + \frac{C6}{r^6} + \frac{C8}{r^8} + \frac{C10}{r^{10}} - C_{ex}e^{-ar} \tag{3.2}$$

with the terms given in table 3.1

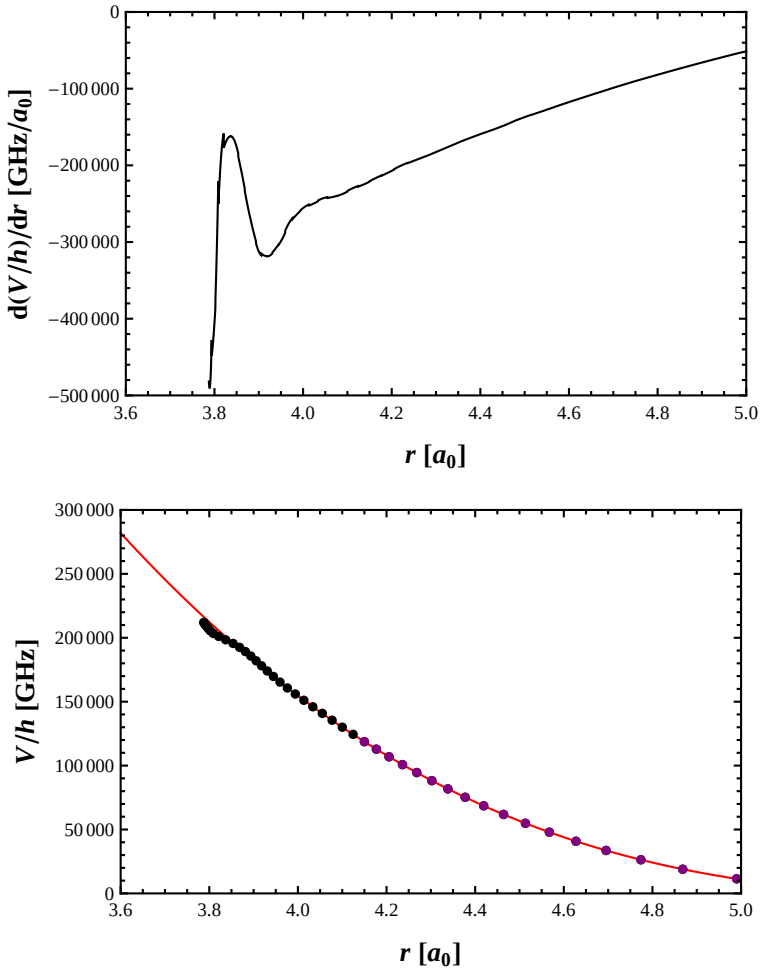

Figure 3.2: (a) Gradient from the interpolated data point that make up the left side of the potential well.(b) To eliminate the fluctuation only the purple data points are used to make a short range potential fit (red curve).

D_e [GHz]	$C6$ [GHz a_0^6]	$C8$ [GHz a_0^8]	$C10$ [GHz a_0^{10}]	C_{ex} [GHz]	a [a_0^{-1}]
213020	9.407×10^9	6.479×10^{11}	1.866×10^{14}	44519	0.494

Table 3.1: The D_e, the van der Waals C_n coefficients and the exchange energy constants obtained from Fellow et al[3].

The full range

The two functions are combined by a switch-function, which enables a smooth transition. Equation 3.3 shows the full potential in which the switch function is incorporated. At the internuclear separation R^* the function is switched from short range to long range. A small vertical shift in the short range potential is given by Δ. The third variable, w, is the width over which the switching is smoothed. The best coupling is made between the curves as

$R^* = 12.1638$ a_0 and $\Delta = 0.020456$ GHz. The width is set at 0.5 a_0.

$$V_{S=0,l=0}(r) = [V_{short}(r) + \Delta]\frac{1 - \tanh(\frac{r-R^*}{w})}{2} + V_{Long}(r)\frac{1 + \tanh(\frac{r-R^*}{w})}{2} \tag{3.3}$$

The result of the coupling between the two potential functions, as described by equation 3.3, is shown in figure 3.3 (left side). The dotted curve is the long range potential, the dashed curve the short range potential (which after 15.74 a_0 extrapolates) and the red curve is the combined potential. The gradient of the combined potential is presented in figure 3.3 (right side).

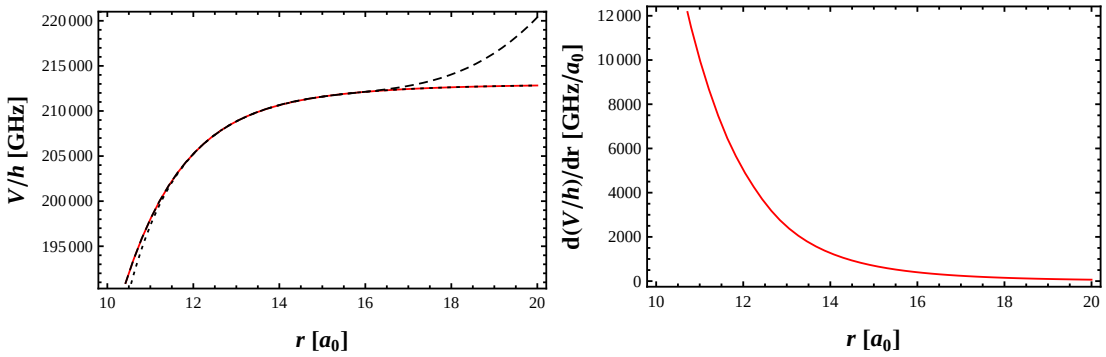

Figure 3.3: The transition between the short and long range potential. The red curve is the $V_{S=0,l=0}(r)$, the long range potential is indicated by the dotted curve and the the short range potential by the dashed (left side). The gradient of the $V_{S=0,l=0}(r)$ is given in the right graph.

The reconstructed full potential is only valid in case of a singlet spin configuration ($S = 0$) with an azimuthal quantum number $l = 0$ (also referred to as s-waves). To expand the potential for other quantum numbers certain adjustments have to be made.
The potential difference between the singlet and triplet spin configuration is twice the exchange energy. In the long range potential the contribution of exchange energy is labeled, which makes it easy to convert the potential to the triplet scenario ($S = 1$) just by adding two times the $+V_{exch}(r) = C_{ex}e^{-ar}$. However this simple correction is not true for small values of r. As the inner potential will already be treated as less precise, we will leave it for now.
In the situation of $l \neq 0$ an other contribution to the potential has to be made to gain the effective potential (equation 3.1); from literature it is known that the angular momentum adds a so-called centrifugal barrier term to the total potential, namely $\frac{\hbar^2}{2\mu}\frac{l(l+1)}{r^2}$.[10]

The last step to adjust the full effective potential is to redefine the zero value. The zero value of the function is still defined at the lowest point of the curve. To redefine the zero of the potential at $V(\infty)$, the dissociation energy D_e-value needs to be subtracted form the function. So, the full effective potential can be written as

$$V^{eff}_{S,l}(r) = V_{S=0,l=0}(r) + 2S \cdot C_{ex}e^{-ar} + \frac{\hbar^2}{2\mu}\frac{l(l+1)}{r^2} - D_e. \tag{3.4}$$

3.2 The relative energy

3.2.1 Accumulated phase method

The central interatomic potential is constructed in the previous section. The short range part is determined by extrapolation and as a result it is not very accurate. However, the interaction between the two atoms is extremely sensitive to the precise form of the interaction potential. Therefore even the smallest changes in the short range potential can have large effects on the interaction. To get around this obstruction and still use equation 3.4, we turn to the accumulated phase method.[14]

The main idea behind the accumulated phase method is the following. In the potential well bound states exist, but the corresponding energy levels are hard to determine due to the inaccurate inner-range potential. However say the energy level of one bound state is known, the potential can be altered in such a way that it gives a bound state at this corresponding energy level. With this correction other energy levels can be obtained. The same result is obtained with the accumulated phase method, however now by altering the wavefunction itself instead of the potential.
The method is demonstrated in the simplified picture of figure 3.4. When a bound state is forced upon a certain energy value, then the corresponding wave function is determined twice. Once with the boundary conditions set in the short range potential and once for proper boundary conditions at long range. At a point r_0 in the potential well, the phases of the two wave functions are compared to one another. The difference between these phases can be expressed in the accumulated phase difference. The next bound state can then be found, by the search for an energy level which enables the same accumulated phase difference.
So the wavefunction of forced energy level does satisfy the boundary conditions, however is altered at r_0 by adding an accumulated phase shift. Other energy levels are found by the search for those wavefunctions which have the same accumulated phase shift.

Criteria for r_0

The internuclear separation r_0, where the accumulated phase difference is determined, has to be chosen carefully and is subjected to four general conditions.
1) The generated wave functions at r_0 needs to be in terms of pure singlet and triplet waves. The coupling between singlet and triplet states is enabled by the hyperfine interaction. As result r_0 must be sufficient small, so that this interaction becomes negligible.
2) On the other hand, the r_0 needs to be so large that the singlet and triplet potentials for $r > r_0$ are precisely known or to be expressed in a small set of parameters.
3) The determination of the accumulated phases relies on the WKB approximation. In order for this approximation to be valid a certain condition should be met, where is stated that the amplitude and the wavelength changes slowly with r.
4) The relative energy E with respect to the threshold and the angular momentum l need to be so small that the accumulated phase can be written as the first order Taylor expansion of E and $l(l+1)$.[11, 14]

To satisfy the first condition, two times the exchange energy needs to be larger then the hyperfine potential energy at r_0. In figure 3.5, twice the exchange energy and the hyperfine potential energy as function of r are shown; from this graph can be concluded that the r_0

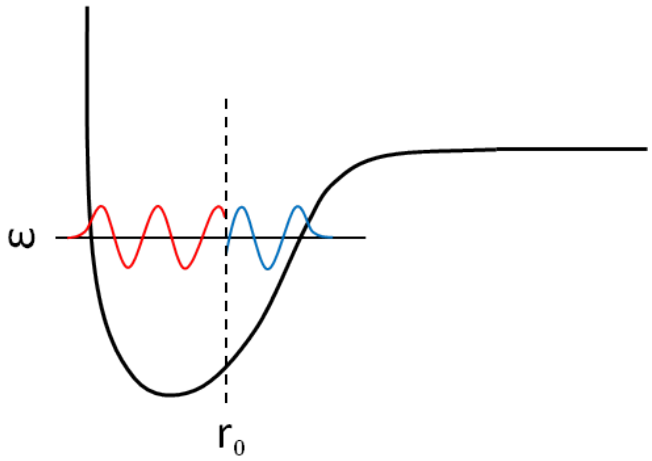

Figure 3.4: Simplified figure of the accumulated phase difference determined at r_0, where the red wave function is calculated with the boundary conditions set on the left side of the potential well and the blue wave function with the boundary conditions set on the right.

needs to be smaller than 24 a_0. The second condition is satisfied if $r_0 > R^*$, so r_0 needs to be larger than 12.16 a_0. The fourth condition requires that $E \approx 0$ with respect to the dept of the potential at r_0 and l should be maximum 4. For r_0 to be between the 12.16 a_0 and the 24 a_0 and l is at most 3, the fourth condition is also met. The third condition will be examined later on in this section, as the wave numbers are required.

Determination of the phase shift

The criteria for the location of r_0 was examined. Now the determination of the phase difference will be highlighted. The first step is to determine the two wavefunctions at a forced bound state energy level ϵ_b. The wavefunction is determined by solving the Schrödinger equation for the two different sets of boundary conditions. The boundary conditions are chosen in such a way that the amplitude of the wave is not too large or too small. Also the point at which the boundary conditions are set should, by changing its position slightly, not influence the logarithmic derivative (ψ'/ψ) inside the well. The boundary conditions of the inner wave are set on the left side of the potential well at $r_{in} = 3.30$ a_0 with $\psi^{in'}[r_{in}]/\psi^{in}[r_{in}] = -0.1$ and $\psi^{in}[r_{in}] = 10^{-3}$. For the outer wave, the boundary conditions are set on the right side of the well at $r_{out} = 135$ a_0. The conditions are $\psi^{out}[r_{out}] = 10^{-4}$ and $\psi^{out'}[r_{out}]/\psi^{out}[r_{out}] = -\frac{\sqrt{2\mu|\epsilon_b|}}{\hbar}$ with μ the reduced mass.

The Schrödinger equation with the above boundary conditions is numerically solved with Mathematica. From this result the accumulated phase can be extracted. In the range of r_0 the wavefunction can be approximated with a real sine. Rewriting then the approximated wavefunction, the equation to gain the accumulated phase with the numerically solved wavefunction at r_0 is obtained.

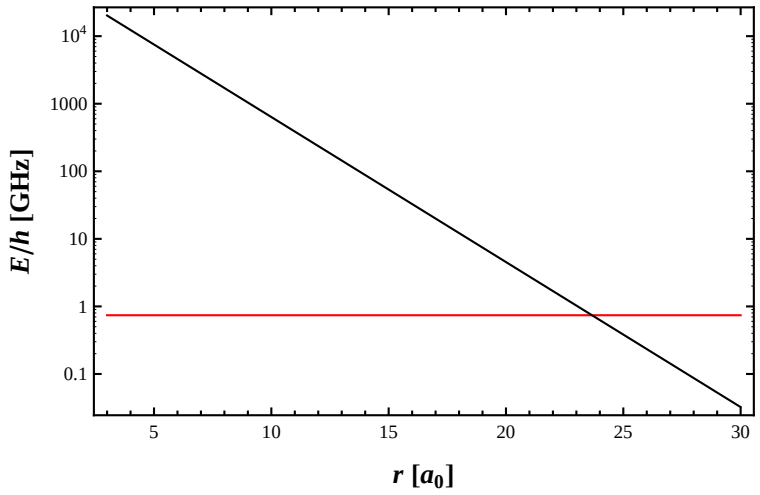

Figure 3.5: The hyperfine energy (red) and twice the exchange energy (black) as function of r.

The real part of radial wavefunction can be written as

$$\psi(r) = A(r)\sin\phi(r), \tag{3.5}$$

where $A(r)$ is the amplitude and $\phi(r)$ is the accumulated phase. As for the moment the S and l dependence of the equations is only important for defining the potential curve. Therefore as matter of convenience when writing the equations we simply ignore the S and l-dependence.

The WKB (Wentzel, Kramers, Brillouin) approximation is the basis to determine the accumulated phase. The method approximates the solutions of the time-independent Schrödinger equation in one dimension. The WKB approximation assumes a slow changing amplitude and phase with r.[10]
Rewriting the Schrödinger equation with the above wavefunction, the amplitude and the phase functions are defined. The amplitude and phase can be written in terms of the local wave number $k(r)$:

$$k(r) = \frac{\sqrt{2\mu(\epsilon - V(r))}}{\hbar}, \tag{3.6}$$

$$A(r) = \frac{C}{\sqrt{k(r)}}, \tag{3.7}$$

$$\phi(r) = \pm\int k(r)dr \tag{3.8}$$

where C is a constant.[10, ?] This approximation is valid by the assumption that $|dk(r)/dr| << |k(r)|^2$. The third condition for r_0, which still needs to be met, results from this assumption. Calculating the wave number and its derivative for several bound state energies, this condition is satisfied for r_0 smaller then roughly $14\ a_0$.

The accumulated phase is determined by integrating the local wave number over r (equation 3.8). However WKB approximation is valid for a limited set of r. To avoid the

integration, the accumulated phase can also be gained by only using the wave information at one specific r. The first step is to determine the logarithmic derivative of $\psi(r)$.

$$\frac{\psi'(r)}{\psi(r)} = k(r)\cot\left(\phi(r)\right) - \frac{k'(r)}{2k(r)} \tag{3.9}$$

The second step is to rewrite equation 3.9, the accumulated phase can be determined by

$$\phi(r) = \operatorname{arccot}\left(\frac{1}{k(r)}\left(\frac{\psi'(r)}{\psi(r)} + \frac{k'(r)}{2k(r)}\right)\right). \tag{3.10}$$

Now all the required information is obtained to calculated the phase mismatch at r_0, which is

$$\Delta\phi_{S,l}(r_0, \epsilon_b) = \mathtt{mod}[\phi^{in}_{S,l}(r_0, \epsilon_b), \pi] - \mathtt{mod}[\phi^{out}_{S,l}(r_0, E_b), \pi] \tag{3.11}$$

for the position of r_0 between 12.16 a_0 and 14 a_0. The accumulated phase is taken modulo π cause every vibrational bound state differs one π in total phase with the next state.

In the next sections the accumulated phase mismatch is used to determine the bound state energy shift due to the centrifugal barrier and to determine the scattering length.

3.2.2 The centrifugal barrier induced energy shift

The angular momentum alters the effective potential for different values of l with the centrifugal barrier term. Due to this term, the position of the bound states in the potential shifts as function of l. To explain the resonance positions measured in Heidelberg, the energy levels of the bound states are necessary with $l = 0, 1$ and 2 (correspond to respectively the partial s-, p-, and d-waves). These can all be taken as free fit parameters, however it is desirable to reduce the number of variables as much as possible.

The accumulated phase method is used to calculate the energy shift in the bound state levels due to the change in l. In other words as the singlet and triplet bound state energy of the s-waves ($l = 0$) are known, the corresponding bound states for the p- and d-waves can calculated with the accumulated phase method. The number of free fit parameters reduces then from six to two.

The s-wave bound states

First the vibrational bound states of the singlet and triplet spin configuration are examined for $l = 0$. As described in the previous section, a bound state forced upon the potential results in an accumulated phase difference. All corresponding vibrational energy levels are then found by the searching for those bound state energies that result in the same accumulated phase difference in the same potential.

In figure 3.6 the accumulated phase difference as function of the forced bound state for singlet and triplet electron spin configuration is shown. The position of r_0 is carefully chosen at 12.5 a_0.

The accumulated phase difference of 0 rad corresponds to energy levels of the 'eigen' vibrational bound states in the potential; i.e. under the assumption that the potential is accurate its bound states are positioned at the energy levels which result in a zero phase difference. The position of the zero phase difference gives an indication where the bound states are

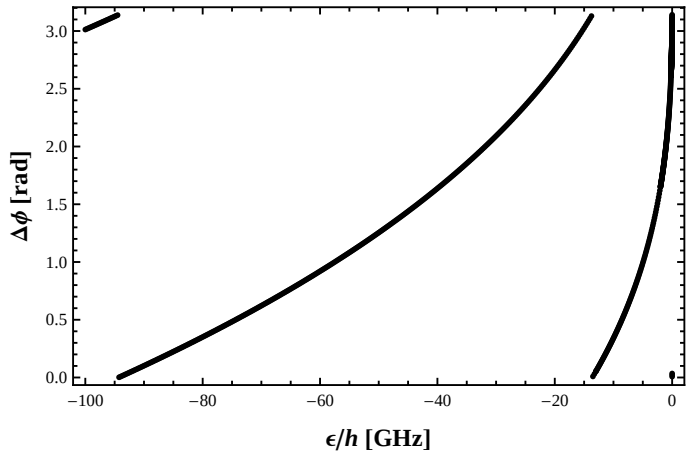

(a) Singlet electron spin configuration

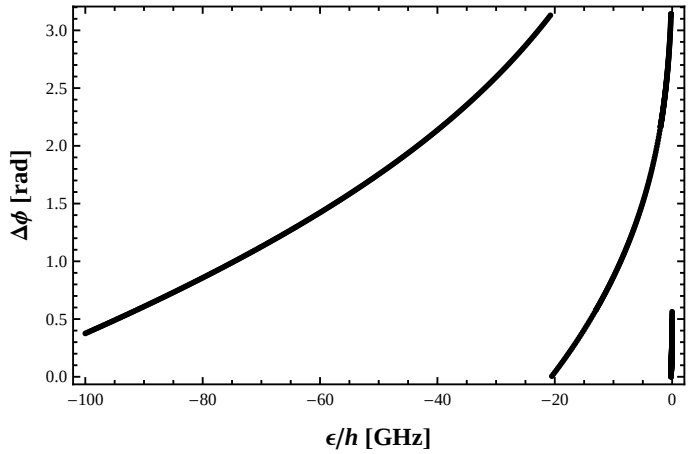

(b) Triplet electron spin configuration

Figure 3.6: Accumulated phase difference at $r_0 = 12.5$ a_0 for $S = 0$ and $l = 0$(a) and $S = 1$ and $l = 0$ (b) as a function of the binding energy.

positioned and the number of bound states in the potential.
The sought-after singlet and triplet bound states do not only differ in vibrational quantum numbers, the inner potential of the triplet spin configuration is less precise than of the singlet. This discrepancy could result in an additional phase difference between the singlet and triplet bound states. Therefore accumulated phase method is not used to reduce these two free fit parameters into one, but treats them separately.

In figure 3.6 for low values of the accumulated phase mismatch a bound state appears between the -0.2 GHz and 0 GHz. For the purpose of this report, these low-lying bound states are neglected. In comparison with a paper of Gacesa et al[2] in which they try to explain only three $^{23}Na^{6}Li$ resonances, they do use this low-lying state as the singlet bound state. However in order to explain the increased set of resonances this vibrational singlet bound state will not suffice and one additional deeper lying state is required.

The p- and d-wave bound states

The s-wave singlet and triplet bound states, which are needed to explain the measurements from Heidelberg, are most likely to be found between the -9.5 and -1 GHz. The corresponding p- and d-wave energy levels are searched for in the same energy regime. As function of the singlet and triplet s-wave bound state energy, the energy shift of the p- and d-waves with respect to the s-waves is shown in figure 3.7. From these figures one can conclude that the energy shift due to the centrifugal barrier, is for the triplet and singlet case almost the same.

So with figure 3.7 the energy levels of p- and/or d-wave bound states can be obtained when the s-wave bound state is known.

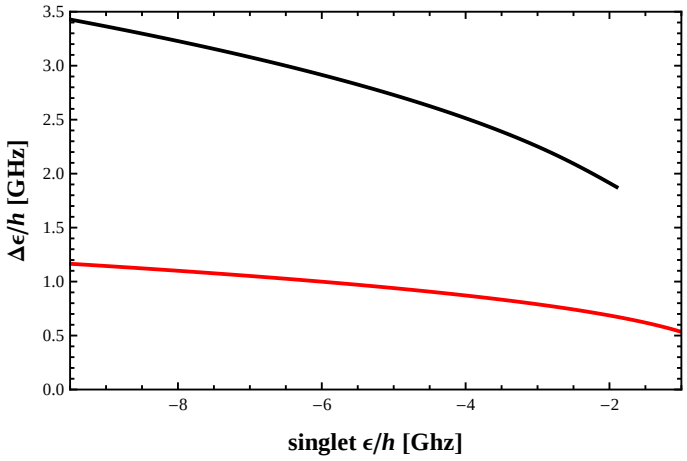

(a) Singlet centrifugal barrier induced energy shift

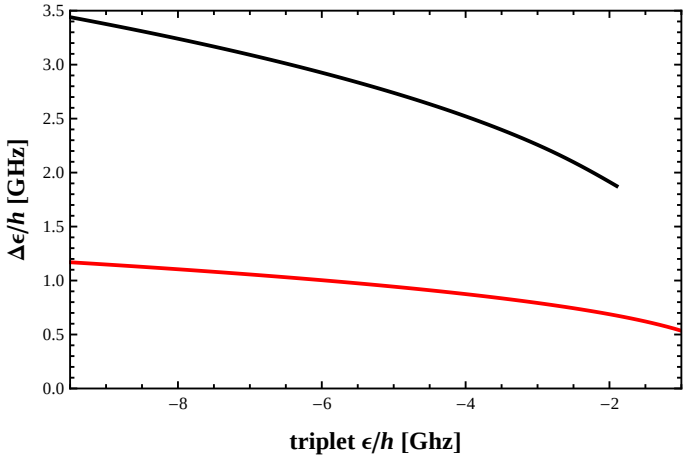

(b) Triplet centrifugal barrier induced energy shift

Figure 3.7: The red and black curve correspond to the bound state energy shift of respectively the p- and d-waves relative to the energy levels of the s-wave for singlet (a) and triplet (b) electron spin configuration.

3.2.3 The scattering length due to direct scattering

The interaction of the particles described by the potential could lead to a bound state or the scattering of the particles with one another. In this section the scattering between the particles is highlighted. For now we will only discuss the interaction of the particles within one channel without the coupling to others, which is called direct scattering. Later we will refer to this contribution to the scattering length as the background scattering length.
For the scattering process with ultracold particles only the s-wave scattering are considered, as higher partial waves are less likely to cross the centrifugal barrier in the ultracold case. A measure for this scattering interaction strength is given by the scattering length. Positive values represent a repulsive interaction and negative scattering lengths an attractive interaction. The scattering length a is defined as

$$a = -\lim_{k\to 0} \frac{\tan \delta_0}{k}, \tag{3.12}$$

where δ_0 is the phase shift of the wavefunction induced by the scattering.[6, 11] Equation 3.12 requires the scattering induced phase shift as function of the wave number k. The phase shift is to be extracted from the numerical determined scattering wavefunction. For the translation from scattering wave to phase shift, we turn to the solutions of the radial Schrödinger equation.

The Schrödinger equation reduces to the form of two free particles if the internuclear separation r is sufficiently large, for the sake of argument the r from which the problem reduces to free particles we shall call r_f. The radial solutions of this free particle equation is a linear combination of the spherical Bessel function $j_l(kr)$ and the spherical Neumann function $n_l(kr)$. The search for the necessary scattering waves is limited to s-waves, with as result that the radial wavefunction $R(r)$ reduces to form

$$R_0(k, r) = B(k) j_0(kr) + C(k) n_0(kr),\ r > r_f \tag{3.13}$$

where $B(k)$ and $C(k)$ are real and independent of r and with the Bessel and Neumann functions,

$$j_0(kr) = \frac{\sin kr}{kr} \tag{3.14}$$

$$n_0(kr) = -\frac{\cos kr}{kr} \tag{3.15}$$

To gain a better inside of the information carried by $B(k)$ and $C(k)$, the wavefunction is written in exponential functions:

$$\psi_0(k, r) = r R_0(k, r) \tag{3.16}$$

$$= B(k)\frac{e^{ikr} - e^{-ikr}}{2ik} - C(k)\frac{e^{ikr} + e^{-ikr}}{2k} \tag{3.17}$$

$$= \frac{1}{2ik}\Big((B(k) - iC(k))e^{ikr} - (B(k) + iC(k))e^{-ikr}\Big),\ r > r_f \tag{3.18}$$

where the e^{ikr} represents the outgoing wave and the e^{-ikr} the incoming one. From these equations, it is clear that one can make a useful substitution for $B(k)$ and $C(k)$ with the following relations,

$$A(k) = \sqrt{B(k)^2 + C(k)^2} \tag{3.19}$$

$$\tan \delta_0(k) = -\frac{C(k)}{B(k)} \tag{3.20}$$

and that the radial wavefunction can be written as a sine with an additional phase of δ_0.

$$\psi_0(k, r) = \frac{A(k)}{k} \sin(kr + \delta_0),\ r > r_f \tag{3.21}$$

The next step is to gain the scattering length from the wavefunction. The logarithmic derivative of the s-wave function $\psi_0(k, r)$ at r_f is determined first:

$$\gamma_0 = \frac{\psi_0'(k, r_f)}{\psi_0(k, r_f)} \tag{3.22}$$

$$= \frac{A(k)k\cos(kr_f + \delta_0)}{k} \frac{k}{A(k)\sin(kr_f + \delta_0)} \tag{3.23}$$

$$= \frac{k}{\tan(kr_f + \delta_0)} \tag{3.24}$$

By rewriting these equations and with the assumption that kr_f goes to zero, the following relations are obtained:

$$\tan(kr_f + \delta_0) = \frac{k}{\gamma_0} \tag{3.25}$$

$$\tan(kr_f + \delta_0) = \frac{\sin(kr_f + \delta_0)}{\cos(kr_f + \delta_0)} \tag{3.26}$$

$$= \frac{\sin(kr_f)\cos(\delta_0) + \cos(kr_f)\sin(\delta_0)}{\cos(kr_f)\cos(\delta_0) - \sin(kr_f)\sin(\delta)} \tag{3.27}$$

$$= \frac{kr_f\cos(\delta_0) + \sin(\delta_0)}{\cos(\delta_0) - kr_f\sin(\delta_0)} \tag{3.28}$$

$$= \frac{kr_f + \tan(\delta_0)}{1 - kr_f\tan(\delta_0)} \tag{3.29}$$

Combining the above equations 3.25 and 3.29, $\tan(\delta_0)$ can be written as

$$\tan(\delta_0) = k\frac{1 - \gamma_0 r_f}{\gamma_0 + k^2 r_f}. \tag{3.30}$$

The combination of this result with equation 3.12 gives in an expression for the scattering length of

$$a = -\lim_{k\to 0}[\frac{1}{\gamma_0} - r_f]. \tag{3.31}$$

Equation 3.31 requires the numerical determined scattering wavefunction. Recall that the wavefunctions of the bound states were determined for two boundary conditions, once in the inner potential and once in the outer potential. Then for a presumed singlet (or triplet) binding energy, the difference in the bound state waves resulted in an accumulated phase difference. Corresponding to the bound state, the scattering wavefunction can be calculated by adding the same accumulated phase to the scattering wave, which has its boundary conditions set only in the inner potential.
The scattering length as function of the forced bound state, is shown in figure 3.8.

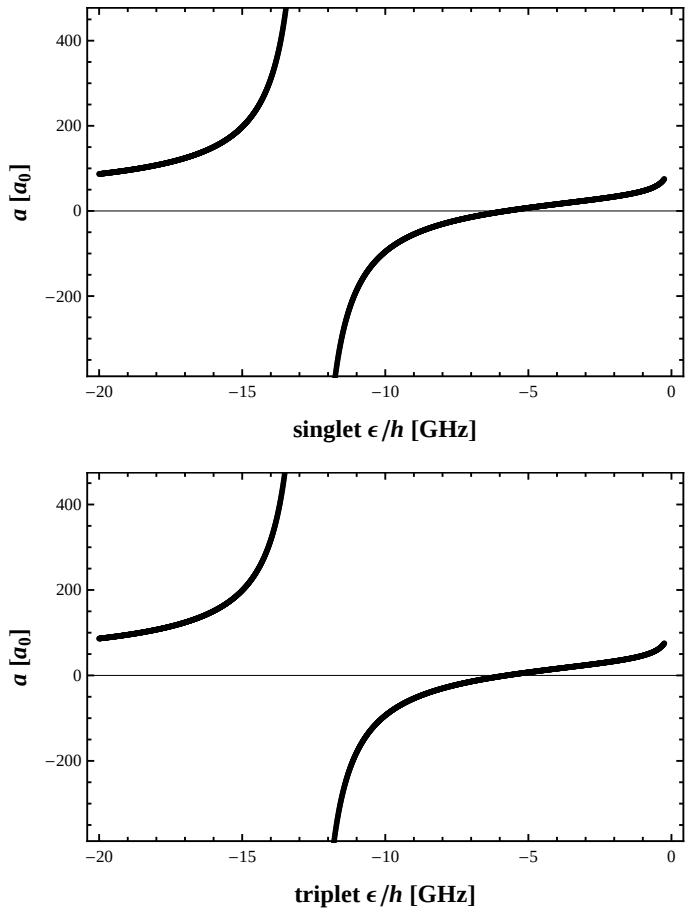

Figure 3.8: The scattering length as function of the bound state energy for the singlet case (a) and triplet (b) electron spin configuration.

3.3 The long range potential sufficient enough?

In the begin stage of this project, it was thought that the centrifugal energy shift could be obtained with only the long range potential. During the project it became clear, that this was not the case. The error which has been made is the main topic of this section. Reason for discussing it in the main part of this report, is to avoid the same mistake in future research.

As the short range potential was unknown only the accumulated phase was sought after and not the accumulated phase difference as we discussed before. The accumulated phase was gained by solving the Schrödinger equation with its boundary conditions set in the long range potential. Then the phase at a r_0 was determined by a forced s-wave energy of ϵ_s and the corresponding p-wave bound state with energy ϵ_p was found by the search for the same accumulated phase.

To see which mistakes this would lead to, recall the WKB approximation with the equations 3.6 and 3.8. The difference between in the phase of the s- and p-wave can be written as:

$$\phi_s - \phi_p = \frac{1}{\hbar}\left(\int_\infty^{r_0} k_s(r)dr - \int_\infty^{r_0} k_p(r)dr\right) \tag{3.32}$$

The chosen position of r_0 should not have an influence on the centrifugal barrier energy shift and meet the four criteria mentioned in subsection 3.2.1. Therefore the phase difference should be independent of r_0. To see if this is the case, the dependence of the phase difference at r_0 is to be further examined and can be written as:

$$\frac{d\left(\phi_s - \phi_p\right)}{dr_0} = k_s(r_0) - k_p(r_0) \tag{3.33}$$

$$= \frac{1}{\hbar}\sqrt{2\mu\left(\epsilon_s + V_s(r_0)\right)} - \frac{1}{\hbar}\sqrt{2\mu\left(\epsilon_p + V_s(r_0) + \frac{\hbar^2 l(l+1)}{2\mu r_0^2}\right)} \tag{3.34}$$

This derivative would be zero, if the centrifugal term and the bound state energy levels are small with respect the long range potential. However this is not the case. It is illustrated in table 3.2, where ϵ_s chosen at -8 GHz and ϵ_p -6.9 GHz. In the table, the r_0 dependence of the phase difference is given for three different long range potential situations: only the C6 part, the full long range potential and the complete potential. The derivative does converges, but in order to use this method, we needed it to be very close to zero. Taken the long range part of the potential into consideration, it does give better results than only using the C6-part of it; however switching from long range to the full potential the result does not improve. So even by taking the full potential this method does not improve.
To give an indication, a phase shift of 0.002 rad in the accumulated p-wave phase corresponds to a rough difference in the bound state energy of 0.015 GHz. So back to the table, a change of one a_0 in the position of r_0 corresponds to a roughly change in phase of 0.00135 rad. So changing the position of r_0 with a couple a_0, the influence on the central barrier shift is in the order of 10^{-2} GHz.
So by assuming that the accumulated phases should be the same, the r_0-dependence of the difference between the two phases is not taken into consideration. This could lead to a crucial error in the calculated barrier shift.

r_0 [a_0]	$\frac{d(\phi_s-\phi_p)}{dr_0}$[rad/$a_0$] $V_s(r) = \frac{C6}{r^6}$	$\frac{d(\phi_s-\phi_p)}{dr_0}$[rad/$a_0$] $V_s(r) = V_{Long}(r)$	$\frac{d(\phi_s-\phi_p)}{dr_0}$[rad/$a_0$] $V_s(r) = V_{S=0,l=0}$
12	0.00190663	0.00121133	0.00121227
12.5	0.00194215	0.00128168	0.00128135
13	0.00197239	0.00134673	0.0013467
13.5	0.00199715	0.00140595	0.00140596
14	0.00201623	0.00145890	0.00145891

Table 3.2: The r_0 dependence of the phase difference between partial waves.

Chapter 4

The ^{23}Na^{6}Li two-body system with the Asymptotic Bound-state Model

Feshbach resonances are caused by two colliding particles in the open channel, interacting with a bound state of the closed space. The interaction will be best if the energy of the two colliding particles is equal to the bound state energy.
The Feshbach resonance positions are obtained at the magnetic field for which the bound state energy of a closed channel is equal to the threshold of the open channel. Recall that the threshold energy is equal to the internal energy of two particles, i.e. the lowest energy possible for free particles in a channel. So the two-body system in the open channel is assumed to have an energy equal to the threshold. This assumption is based on the ultracold circumstances, for which the kinetic energy is neglected.

The bound state energy was studied in the previous chapter, where energies were obtained relative to the central potential at $r = \infty$. However the relative bound state energy of the two-body system is not sufficient and needs to be expanded with the internal energy of the system. In this way the bound state energy and the threshold have the same zero-reference point.

The internal energy of the non-interacting particles, which define the thresholds, was examined in chapter 2. So all the ingredients to determine the resonance properties have been studied and now only need to be combined. The properties of the resonances obtained with ABM is the topic of this chapter. First the total Hamiltonian of the two-body system is required. This will be discussed in the first section, after which the method to find the Feshbach resonance positions will be studied and finally the resonance widths.

4.1 Total Hamiltonian

The Hamiltonian which describes the two-body system is given by equation 4.1, the sum of the internal and relative Hamiltonian. The relative energy is characterized by the wave-function of the two-body system and quantum numbers S, l and ν. The internal energy is defined by its spin combination and its projection on the magnetic axis. Consequently the total basis in which the H^{Tot} needs to be written, can be split into a wave and a spin part.

$$H^{Tot} = H^{Int} + H^{Rel} \tag{4.1}$$

The relative Hamiltonian depends on the effective central potential. From equation 3.1 it is known that the bound state wavefunctions $\psi_\nu^{Sl}(r)$ have a relative energy of ϵ_ν^{Sl}. Consequently, the relative Hamiltonian is diagonal in the $\psi_\nu^{Sl}(r)$ basis (equation 4.2).

$$H^{Rel}\psi_\nu^{Sl} = \epsilon_\nu^{Sl}\psi_\nu^{Sl} \tag{4.2}$$

The extrinsic orbital angular momentum is given by quantum number l, which quantizes the angular part of the Schrödinger equation. The central interaction is isotropic, which means that it has no influence on the angular equation and hence on l. Therefore l is a good quantum number under collisions.
This means that the partial waves do not couple with one another and are therefore treated separately.[6]

The internal Hamiltonian H^{Int} consists out of the hyperfine and the Zeeman contributions (H^{hf} and H^Z), which depend on the electron and nuclear spins of both the ^{23}Na and ^{6}Li atoms:

$$H^{Int} = H^{hf} + H^Z, \tag{4.3}$$

$$H^{hf} = \frac{a_{Na}^{hf}}{\hbar^2}\vec{s}_{Na}\cdot\vec{i}_{Na} + \frac{a_{Li}^{hf}}{\hbar^2}\vec{s}_{Li}\cdot\vec{i}_{Li}, \tag{4.4}$$

$$H^Z = \left(\gamma_e\vec{S} - \gamma_{n,Na}\vec{i}_{Na} - \gamma_{n,Li}\vec{i}_{Li}\right)\cdot\vec{B}. \tag{4.5}$$

Consider the magnetic quantum number m to be the projection of angular momentum on the axis parallel to $\vec{B}$. Then the Zeeman Hamiltonian is diagonal in the $|\sigma\rangle \equiv |SM_S m_{i,Na} m_{i,Li}\rangle$-basis. This is shown by equations 4.6 and 4.7.

$$E_\sigma^Z = \left\langle\sigma\left|H^Z\right|\sigma'\right\rangle \tag{4.6}$$

$$= \hbar\left(\gamma_e M_S - \gamma_{n,Na}m_{Na} - \gamma_{n,Li}m_{Li}\right)B\delta_{\sigma,\sigma'} \tag{4.7}$$

Consequently, the combination of the above wave and spin basis makes a good candidate for the ABM-basis, $\left\{\left|\psi_\nu^{Sl}\right\rangle|\sigma\rangle\right\}$. The total Hamiltonian can then be written as in equation 4.8. This basis is orthonormal, with $\langle\sigma|\sigma'\rangle = \delta_{\sigma,\sigma'}$ and $\left\langle\psi_\nu^{Sl}|\psi_{\nu'}^{S'l}\right\rangle = \eta_{\nu,\nu'}^{S,S'}$ (also known as the Frank-Condon factors). When $\sigma = \sigma'$ it means that $S = S'$ and from the Frank-Condon factors it is known that $\eta_{\nu,\nu'}^{S,S} = \delta_{\nu,\nu'}^{S,S}$ resulting in an orthonormal set.[6]

$$H_{\psi\sigma}^{Tot} = \left\langle\sigma\left|\left\langle\psi_\nu^{Sl}\left|H^{Tot}\right|\psi_{\nu'}^{S'l}\right\rangle\right|\sigma'\right\rangle \tag{4.8}$$

$$= \epsilon_\nu^{Sl}\delta_{\nu\sigma,\nu'\sigma'} + E_\sigma^Z\delta_{\nu\sigma,\nu'\sigma'} + \eta_{\nu,\nu'}^{S,S'}\left\langle\sigma\right|H^{hf}\left|\sigma'\right\rangle \tag{4.9}$$

In this ABM- basis, the Zeeman and the relative bound state energy only contribute to the diagonal of the Hamiltonian matrix (equation 4.9). The third contribution is made by the hyperfine energy.

The hyperfine Hamiltonian can be rewritten as function of the total electron spin, namely $H^{hf} = H^{hf}_{+} + H^{hf}_{-}$ with H^{hf}_{+} and H^{hf}_{-} given by equation 4.10. In case of H^{hf}_{+} the total electron spin S is conserved. The hyperfine part H^{hf}_{-} does not conserve the total electron spin, but couples the singlet to triplet spin configuration and the other way around.
So the hyperfine Hamiltonian written in the ABM-basis has a diagonal part H^{hf}_{+} and an off-diagonal part caused by H^{hf}_{-}.[4]

$$H^{hf}_{\pm} = \frac{a^{Na}_{hf}}{2\hbar^2}\left(\vec{s}_{Na} \pm \vec{s}_{Li}\right)\cdot\vec{i}_{Na} \pm \frac{a^{Li}_{hf}}{2\hbar^2}\left(\vec{s}_{Na} \pm \vec{s}_{Li}\right)\cdot\vec{i}_{Li} \tag{4.10}$$

The eigenvalues of the total Hamiltonian give the discrete set of bound state energies. The eigenvalues are obtained by evaluating the $\det\left|H^{Tot}_{\psi\sigma} - E_b I\right| = 0$, with I the identity matrix. This is shown in equation 4.11, where E_b is the eigenvalue of the system and is to be subtracted of the diagonal in the determinant calculations.

$$\det\left|\left(\epsilon^{Sl}_{\nu} + E^{Z}_{\sigma} - E_b\right)\delta_{\nu\sigma,\nu'\sigma'} + \eta^{S,S'}_{\nu,\nu'}\left\langle\sigma\right|H^{hf}\left|\sigma'\right\rangle\right| = 0 \tag{4.11}$$

Free parameters
For this ^{6}Li^{23}Na-research not all required parameters in equation 4.11 are known. The unknown parameters are the relative bound state energies $\left\{\epsilon^{Sl}_{\nu}\right\}$ and the Frank-Condon factors $\left\{\eta^{S,S'}_{\nu,\nu'}\right\}$.
As discussed in chapter 3, the set of ϵ^{Sl}_{ν} can be reduced into two free parameters, from which the other partial bound state energies can be calculated using the accumulated phase method. The two remaining unknown energies are the singlet and triplet s-wave bound state energies.
The Frank-Condon factors can be approximated for weakly bound states. In that case the overlap between the wavefunctions is mainly determined by the bound state energies instead of the potential shape. The weakly bound states are also called halo states[4], for which their outer classical turning point r_c is much larger than the van der Waals range of the potential r_{vdW}. As a result, the largest probability to find the particle is outside the classical turning point r_c. Therefore the wavefunction can be approximated by $\psi(r) \sim e^{-\kappa r}$ where $\kappa = \sqrt{-2\mu\epsilon/\hbar^2}$. With this approximation and normalization, we obtain $\psi(r) = \frac{1}{\sqrt{2\kappa}}e^{-\kappa r}$. Consequently the Frank-Condon factors can be written as,[4]

$$\langle\psi_0|\psi_1\rangle = 2\frac{\sqrt{\kappa_0\kappa_1}}{\kappa_0 + \kappa_1}. \tag{4.12}$$

For our two-body system the van der Waals range is equal to 35.3 a_0, which is equal to the r_c if the relative bound state energy has the value -5.19 GHz. So for a relative bound state with an energy much larger than -5.19 GHz, equation 4.12 can be used to obtain the Frank-Condon factors. In other cases, $\left\{\eta^{S,S'}_{\nu,\nu'}\right\}$ is taken as one free parameter in case $S \neq S'$, since for $S = S'$ it is a Kronecker delta $\delta_{\nu,\nu'}$.
Thus in short, to find the resonance spectrum of ^{6}Li ^{23}Na system there are only three free

parameters needed to be considered, namely the relative singlet and triplet s-wave bound state energies and the Frank-Condon factor $\eta_{\nu,\nu'}^{S,S'}$.

4.2 Feshbach resonance positions

A Feshbach resonance position is defined as the magnetic field B_0 at which a resonance occurs. At this magnetic field the bound state energy of the system equals the threshold ($E_b(B_0) = E_{thres}(B_0)$), according to ABM. A fictitious case is shown in figure 4.1, where the threshold is plotted as function of the magnetic field as well as the bound state energy levels. The dots represent the location where the theoretically obtained resonances are found.

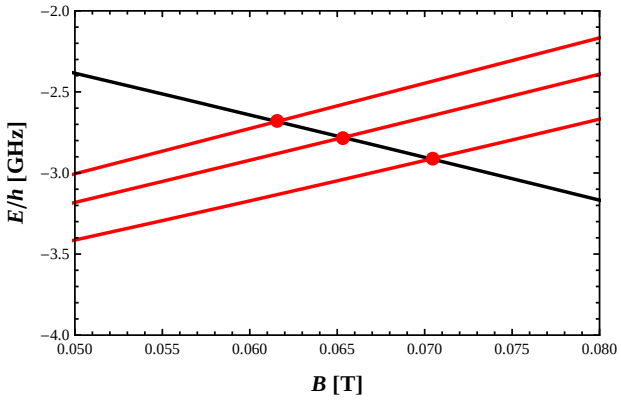

Figure 4.1: Feshbach resonances positions (red dots) of a fictitious case, which occur at the crossing of the bound state energy levels (red curves) with the threshold (black curve).

The eigenvalues of the total Hamiltonian (equation 4.11) gives all the possible bound state energies (E_b) as function of the magnetic field. A simple comparison of those energies with all the possible thresholds as function of B, would give the complete set of resonance positions. However this would lead to more resonances than possible, as the criteria of conserving the good quantum numbers is not taken into account. Also the opportunity arises to classify the resonances in independent sets according to their good quantum numbers. This is makes the problem of comparing the correct measured and calculated resonances more manageable.
Therefore we focus first on the conservation of quantum numbers during a collision in the presence of a magnetic field.

The interactions between the two atoms is described by the isotropic central potential. This potential does not couple the total spin angular momentum $\vec{F} = \vec{f_1} + \vec{f_2}$ to the orbital angular momentum $\vec{l}$, therefore the system is invariant under independent rotations of $\vec{F}$ and $\vec{l}$ in the absence of a magnetic field. In this case there is no net force exerting on the two-body system during collisions and hence the $\vec{F}$ and $\vec{l}$ are conserved.
In the presence of an external magnetic field, the induced torque would lead to rotations of the angular momentum $\vec{F}$ around the axis through the center of mass and parallel to the

magnetic field. Therefore the projections on the axis will be conserved. As already stated l is a good quantum number under collisions and as it is not coupled to $\vec{F}$, it will also be conserved in the presence of a magnetic field. Consequently M_F, m_l and l are good quantum numbers under collisions in external magnetic field. As a result the calculated resonances can be subdivided according to these good quantum numbers.[11]

As earlier mentioned, not all parameters in the determinant of equation 4.11 are known. This leaves room for many possible sets of E_b and hence resonance positions. To obtain the unknown parameters it is necessary that theory and experiment reinforce one another. The unknown parameters must be first found in order to describe the whole system. This search is done by evaluating a (not complete) set of measured resonances. The key factor in this search, is to correctly link the measured to the calculated resonances and vice versa; this is difficult as it is not known which partial wave and spin combination should correspond to a measured resonance. However what can be identified is the entrance channel in which the two-body system is prepared, and this fixes already the value of M_F. The entrance channel of the $|f_1, m_{f_1}\rangle |f_2, m_{f_2}\rangle$-state and does not reveal any information about the partial wave of a resonance. Consequently only one good quantum number is known from measured resonances, which is the total projection of angular momentum $M_F = m_{f_1} + m_{f_2}$. As a result the resonances can only be subdivided by their M_F-value.

NOTE: The interaction between the atoms does not only consists out of the central interaction; the spins also interact via a magnetic dipole-dipole interaction V^{SS}. This additional contribution is in general very small, and we have quietly neglected this term. We won't go into much detail, however this potential contribution is anisotropic and does couple $\vec{F}$ to $\vec{l}$. Hence if this contribution is not to be neglected, M_f, m_l and l aren't good quantum numbers anymore but sum of the projections $M_f + m_l$ is.[6]

4.3 Widths of the resonances

The field width is an important property of a resonance, as it determines the chance of detection and its usability in applications. For s-waves the width is defined by the coupling strength between the bound state and the continuum. However for other partial waves tunneling through the centrifugal barrier is the dominant process. Only the widths of the s-wave resonances can be determined by ABM; this is due to the fact that for $l \neq 0$ other physical process have to be taken into account.[4]
The s-wave widths will be studied in this chapter, as they can be obtained with ABM and we expect that those waves will be the most measured. The field width ΔB can be defined via the dispersive behavior of the scattering length near a resonance position B_0[15]

$$a(B) = a_{bg}\left(1 - \frac{\Delta B}{B - B_0}\right), \tag{4.13}$$

where a_{bg} is the background scattering length, which is caused by the direct scattering processes in the open channel without coupling to the closed channels. In other words close to a resonance, the dispersive behavior of the scattering length is characterized by a_{bg}, the field width ΔB and the resonance position B_0.
One must be careful when comparing the obtained field widths with experiments, as they

are not necessarily the same. The experimental widths are usually defined as the width of the experimental loss feature. However one would expect the same hierarchy; as a broad field width causes the loss feature to be smeared out over a broader magnetic field range.

According to literature[5] the energy of a bound state near the threshold can be written as function of the scattering length, if the two channels are strongly coupled and hence result into large scattering lengths. In that case the binding energy of the system goes as,

$$E = -\frac{\hbar^2}{2\mu a^2}. \tag{4.14}$$

The energy can also be obtained from the poles of the scattering matrix, in which the threshold behavior is incorporated. If then both formulations of the energy are compared, an expression for the scattering length near a resonance point can be obtained. The width ΔB is then just to be gained from this expression in combination with equation 4.13.
In this section it will be shown that the field width can be determined without knowledge of the continuum states. This is based on the scattering behavior in the zero-energy limit close to resonances and is then closely related to the threshold behavior of the bound state.

This section is divided into two subsections. In the first subsection, ΔB is obtained by the execution of the above steps. To gain a feeling where the field width originates from, the scattering or S matrix and its poles are firmly discussed. In the second subsection the focus will be on how to obtain the field width by the use of the coupling between the least bound state in the open channel and the resonant level in the closed channel.

4.3.1 Scattering length close to a resonance

The scattering length near a resonance is to be obtained from the equality of the closed bound state energy with equation 4.14. In ABM we determine the bound state energy by neglecting the coupling to the threshold or continuum states. However for the comparison with equation 4.14 it is crucial to incorporate the coupling. The states for which this coupling is taken into account, are called the dressed states.
To obtain the dressed bound state energies, we first need to turn to the scattering matrix. The scattering matrix contains two process, namely the direct (or background) scattering caused by the interaction with the potential of the open channel and the second by the interaction with a closed channel bound state (causing the Feshbach resonances); an indication of an open and closed channel is given in 1.1. The S-matrix will diverge as the energy of the two-body system is equal to the dressed bound state energy and consequently the dressed bound state energies can be obtained by poles of the S-matrix.
So first we will turn to the origin of the S-matrix, after which the scattering length and the expression for ΔB will be discussed.

S-matrix

The whole derivation of the scattering matrix is based on two papers published by Marcelis et al.[15] and Moerdijk et al.[16]. The two particle system can be divided into two orthonormal subspaces, the closed and open space. The particles are prepared in the open channel space $\mathcal{P}$ and will return to it after the collision. The closed channel space $\mathcal{Q}$, is the space where the particles from $\mathcal{P}$ interact with the bound states of the closed channels. The projection

operators P and Q project respectively to the subspaces $\mathcal{P}$ and $\mathcal{Q}$.
As a result, the total Hamiltonian can be divided into four parts

$$H^{Tot} = \begin{pmatrix} H_{PP} & H_{PQ} \\ H_{QP} & H_{QQ} \end{pmatrix}, \tag{4.15}$$

where $H_{PP} \equiv PHP$ and $H_{QQ} \equiv QHQ$ are the Hamiltonians within each subspace and $H_{PQ} \equiv PHQ$ and $H_{QP} \equiv QHP$ the components which enable the coupling between the subspaces. Consequently the Schrödinger equation $H^{Tot}|\Psi\rangle = E|\Psi\rangle$ can also be divided into two coupled equations, namely

$$(E - H_{PP})|\Psi_P\rangle = H_{PQ}|\Psi_Q\rangle, \tag{4.16}$$
$$(E - H_{QQ})|\Psi_Q\rangle = H_{QP}|\Psi_P\rangle, \tag{4.17}$$

where $|\Psi_P\rangle \equiv P|\Psi\rangle$, $|\Psi_Q\rangle \equiv Q|\Psi\rangle$ and E defined relative to the threshold of the open channel and equal to $\hbar^2k^2/2\mu$. To write the scattering process as function of the incoming and outgoing waves, $|\Psi_Q\rangle$ needs to be eliminated from equation 4.16. Equation 4.17 can be rewritten as

$$|\Psi_Q\rangle = \frac{1}{E^+ - H_{QQ}} H_{QP}|\Psi_P\rangle, \tag{4.18}$$

where $\frac{1}{E^+ - H_{QQ}}$ is the resolvent or Green's operator G^+_{QQ} and $E^+ = E + i\delta$ with δ approaching zero from positive values. The imaginary part is added to E in case there are open channels included into $\mathcal{Q}$.[17] This expression for $|\Psi_Q\rangle$ can be substituted in equation 4.16 which results in $(E - H_{eff})|\Psi_P\rangle = 0$, where

$$H_{eff} = H_{PP} + H_{PQ}\frac{1}{E^+ - H_{QQ}} H_{QP}. \tag{4.19}$$

In words the effective Hamiltonian H_{eff} is devided into two parts, the first term results from the direct scattering process in $\mathcal{P}$ and the second term describes the journey from $\mathcal{P}$ to $\mathcal{Q}$, propagating through $\mathcal{Q}$, and finally returning back to $\mathcal{P}$.
The next step is to rewrite the resolvent operator in terms of discrete and continuum eigenstates of H_{QQ},

$$\frac{1}{E^+ - H_{QQ}} = \sum_i \frac{|\phi_i\rangle\langle\phi_i|}{E - \epsilon_i} + \int \frac{|\phi(\epsilon)\rangle\langle\phi(\epsilon)|}{E^+ - \epsilon} d\epsilon, \tag{4.20}$$

where $|\phi_i\rangle$ and $|\phi(\epsilon)\rangle$ are the eigenstates of the H_{QQ} respectively the discrete (bound) and continuum (scattering) states with the eigenvalues ϵ_i and ϵ.
Equation 4.20 can be simplified, under the assumption that one bound state of $\mathcal{Q}$ with energy ϵ_Q is so close to E, that the other discrete and continuum states can be neglected. It follows that the resolvent operator G^+_{QQ} can be written as $\frac{|\phi_Q\rangle\langle\phi_Q|}{E - \epsilon_Q}$ and equation as4.16

$$(E - H_{PP})|\Psi_P\rangle = H_{PQ}\frac{|\phi_Q\rangle\langle\phi_Q| H_{QP}|\Psi_P\rangle}{E - \epsilon_Q}. \tag{4.21}$$

The solution to this relation has a homogeneous and a particular part and is given by equation 4.22, where $\frac{1}{E^+ - H_{PP}}$ is the resolvent operator G^+_{PP}. The homogeneous solution $|\Psi^+_P\rangle$

is the uncoupled solution in $\mathcal{P}$ space according to H_{PP} and satisfies the outgoing wave boundary conditions (after the collision the system will be in $\mathcal{P}$ again without interaction to the closed channels).

$$|\Psi_P\rangle = \left|\Psi_P^+\right\rangle + \frac{1}{E^+ - H_{PP}} H_{PQ} \frac{|\phi_Q\rangle \langle\phi_Q| H_{QP} |\Psi_P\rangle}{E - \epsilon_Q} \tag{4.22}$$

The next step is to write $|\Psi_P\rangle$ as function of only $\left|\Psi_P^+\right\rangle$, as it represents the influence of the collision on the incoming wave $\left|\Psi_P^+\right\rangle$. This can be done by multiplying equation 4.22 with $\langle\phi_Q| H_{QP}$, from which an expression for $\langle\phi_Q| H_{QP} |\Psi_P\rangle$ is to be obtained. This leads to the solution

$$|\Psi_P\rangle = \left|\Psi_P^+\right\rangle + \frac{1}{E^+ - H_{PP}} H_{PQ} \frac{|\phi_Q\rangle \langle\phi_Q| H_{QP} \left|\Psi_P^+\right\rangle}{E - \epsilon_Q - \mathcal{A}(E)}, \tag{4.23}$$

were $\mathcal{A}(E)$ is defined as

$$\mathcal{A}(E) \equiv \langle\phi_Q| H_{QP} \frac{1}{E^+ - H_{PP}} H_{PQ} |\phi_Q\rangle . \tag{4.24}$$

To obtain the scattering matrix, the incoming (+) and outgoing (-) wavefunctions $\left|\Psi_P^\pm\right\rangle$ needs to defined. The Lippmann-Schwinger equation[17] dictates that

$$\left|\Psi_P^\pm\right\rangle = |\chi_P\rangle + \frac{1}{E^\pm - H_{PP}} V_{PP} |\chi_P\rangle , \tag{4.25}$$

where $|\chi_P\rangle$ are the unscattered states, so the states where the particles are prepared in and finally return to. The Hamiltonian of subspace $\mathcal{P}$, can be divided into H_{PP}^0, which is the internal energy Hamiltonian and V_{PP} the interatomic interactions. Thus in other words $|\chi_P\rangle$ is an eigenstate of H_{PP}^0.

From the transition or T- matrix the S-matrix can be obtain with $\mathcal{S} = 1 - 2\pi i \mathcal{T}$, where $S = \langle\chi_P| \mathcal{S} |\chi_P\rangle$ and $T = \langle\chi_P| \mathcal{T} |\chi_P\rangle$. So lets turn to the transition matrix first. The transition matrix gives the transition probability from one state to another. The transition operator $\mathcal{T}$ is defined[18] as

$$\mathcal{T} \equiv V_{eff} + V_{eff} \frac{1}{E^+ - H_{eff}} V_{eff}, \tag{4.26}$$

$$= V_{eff} \left(1 + \frac{1}{E^+ - H_{eff}} V_{eff}\right), \tag{4.27}$$

where $V_{eff} = H_{eff} - H_{PP}^0$ and $G_{eff}^+ = \frac{1}{E^+ - H_{eff}}$. Hence the transition matrix becomes,

$$T = \langle\chi_P| V_{eff} \left(1 + G_{eff}^+ V_{eff}\right) |\chi_P\rangle . \tag{4.28}$$

Part of the right side can be substituted by $|\Psi_P\rangle = \left(1 + G_{eff}^+ V_{eff}\right) |\chi_P\rangle$, the relation is obtain by inserting the Lippmann-Schwinger into equation 4.22. The transition matrix results

in

$$T = \langle \chi_P | \left[V_{PP} + H_{QP} \frac{1}{E^+ - H_{QQ}} H_{QP} \right] | \Psi_P \rangle , \tag{4.29}$$

$$= \langle \chi_P | V_{PP} | \Psi_P^+ \rangle + \langle \Psi_P^- | H_{QP} \frac{1}{E^+ - H_{QQ}} H_{QP} | \Psi_P \rangle , \tag{4.30}$$

where $|\Psi_P\rangle$ is replaced by equation 4.22. The expression for the S-matrix can be then be written as

$$S(k) = S_P(k) - 2\pi i \frac{\langle \Psi_P^- | H_{PQ} | \phi_Q \rangle \langle \phi_Q | H_{QP} | \Psi_P \rangle}{E - \epsilon_Q}, \tag{4.31}$$

where $S_P(k) = \langle \Psi_P^-(E) | \Psi_P^+(E) \rangle$ and originates from the direct scattering process. Just as before, $\langle \phi_Q | H_{QP} | \Psi_P \rangle$ can be substituted (the substitution originates from multiplying equation 4.22 with $\langle \phi_Q | H_{QP}$). The scattering matrix finally results into,

$$S(k) = S_P(k) \left(1 - 2\pi i \frac{\left| \langle \phi_Q | H_{QP} | \Psi_P^+ \rangle \right|^2}{E - \epsilon_Q - \mathcal{A}(E)} \right). \tag{4.32}$$

The $S_P(k)$ contribution originates from the eigenstates from H_{PP}. Those states are often referred to as the Gamow states $|\Omega_n\rangle$, which have an energy $\epsilon_{P_n} = \hbar^2 k_n^2/(2\mu)$, with $k_n = i\kappa_n$ and κ_n is real.
Lets assume that we only need to consider one single bound state of the open channel. The direct scattering contribution to the S-matrix can therefore be written as,

$$S_P(k) = e^{-2ika_{bg}} \tag{4.33}$$

$$= e^{2ia_{bg}^P} \frac{\kappa_p - ik}{\kappa_p + ik} \tag{4.34}$$

where $a_{bg} = a_{bg}^P + a^P$. The scattering length a_{bg}^P is caused by non resonant scattering and is in the order of the van der Waals potential range. The second term a^p is the scattering length caused by a resonance of the direct scattering and has the value $1/\kappa_P$.

Scattering length
The poles of the S-matrix indicate the values of E of the dressed (quasi) bound state energies of the system. The poles are given by equation 4.35, which hold under the condition that E is near the threshold, where one open and one closed bound state are dominant.

$$(k - i\kappa_P) \left[E - \epsilon_Q - \mathcal{A}(E) \right] = 0. \tag{4.35}$$

The term $\mathcal{A}(E)$ is determined by the propagator $\frac{1}{E^+ - H_{PP}}$ (equation 4.24). This propagator can be written in Gamow resonance states and as a summation of its poles, the Mittag Leffler expansion[15]

$$\frac{1}{E^+ - H_{PP}} = \frac{\mu}{\hbar^2} \sum_{n=1}^{\infty} \frac{|\Omega_n\rangle \langle \Omega_n^D|}{k_n(k - k_n)}, \tag{4.36}$$

where $\left|\Omega_n^D\right\rangle$ is a dual state of $|\Omega_n\rangle$ and defined as $|\Omega_n\rangle^*$. The assumption that only one bound state of the open channel dominates, reduces the equation 4.36 to situation of only one state $|\Omega_P\rangle$. Then $\mathcal{A}(E)$ can be written as

$$\mathcal{A}(E) = \frac{\mu}{\hbar^2}\frac{-iA}{\kappa_p(k-i\kappa_p)}, \tag{4.37}$$

with $A \equiv \langle\phi_Q| H_{QP} |\Omega_P\rangle \left\langle\Omega_P^D\right| H_{PQ} |\phi_Q\rangle$. The $\mathcal{A}(E)$ can be split into a real and imaginary part (equation 4.40). The real part shifts the unperturbed value ϵ_Q of equation 4.35 with Δ, caused by the coupling. The imaginary part $\Gamma(E)/2$, the energy decay width, determines the lifetime $\tau = \hbar/\Gamma$ of the bound state above the threshold and the coupling to the continuum states. If $E < 0$, then E is below the threshold of the open channel and the bound state in the $\mathcal{Q}$ space cannot couple to the continuum states of the $\mathcal{P}$ space. As a result the imaginary part of $\mathcal{A}(E)$ is zero, for $E > 0$ it is non-zero, and defines a decay width that describes the decay of the bound state into continuum states of $\mathcal{P}$.[6,15]

$$\mathcal{A}(E) = \frac{\mu}{\hbar^2}\frac{-iA(k+i\kappa_p)}{\kappa_P(k^2+\kappa_P^2)} \tag{4.38}$$

$$= \frac{\mu}{\hbar^2}\frac{A}{(k^2+\kappa_P^2)} - i\frac{\mu}{\hbar^2}\frac{Ak}{\kappa_P(k^2+\kappa_P^2)} \tag{4.39}$$

$$= \Delta + \frac{i}{2}\Gamma \tag{4.40}$$

In the low energy limit, $k \to 0$, the real and imaginary components of $\mathcal{A}(E)$ result into $\Delta = A/(2|\epsilon_P|)$ and $\Gamma = 2Ck$ with $C = A/(2\kappa_P|\epsilon_P|)$. Near the threshold $\epsilon_Q + \Delta$ can be linearly approximated by $\mu_{rel}(B - B_0)$ with $\mu_{rel} \equiv \frac{\partial\epsilon_Q}{\partial B}$ and B_0 is the field at which the dressed state crosses the threshold.[6] Near the threshold, the dressed state energy is almost zero. Therefore the S-matrix diverges as the relation holds,

$$\mu_{rel}(B - B_0) + \frac{i}{2}\Gamma = 0, \tag{4.41}$$

$$\mu_{rel}(B - B_0) + \frac{iAk}{2\kappa_P|\epsilon_P|} = 0 \tag{4.42}$$

Now k can be substituted by $\sqrt{2\mu E/\hbar^2}$, which leaves the expression for the dressed bound state energy as

$$E = -\left(\frac{2|\epsilon_P|^{3/2}\mu_{rel}(B - B_0)}{A}\right)^2 \tag{4.43}$$

The dressed bound state energy as function of the magnetic field for a fictitious two-body system, is given in figure 4.2. The figure is obtained from the PhD thesis of M. Goosen[6]. In this figure, the uncoupled open and closed bound states are given by respectively ϵ_P and ϵ_Q. The pure ABM energy levels, which we use to determine the resonance positions throughout this thesis, are given by the dotted gray curves. In the inset one can see that the dressed energy levels go quadratically with the magnetic field and that the coupling to the threshold shifts the ABM resonance positions.

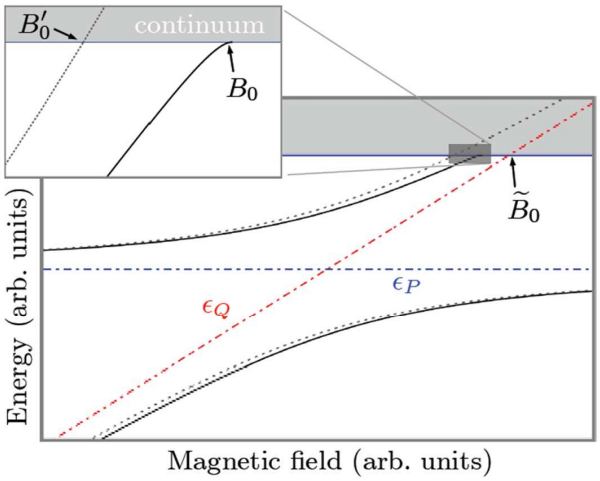

Figure 4.2: The energy levels, relative to the threshold, for a fictitious two-body system. The dressed ABM energy levels are given by black solid curves. The dressed resonance position is given by B_0. Near the resonance the dressed energy level goes quadratically with the magnetic field, as shown in the inset. The gray dotted line is the ABM bound state energy level, which is of course without coupling to the threshold, and its resonance position is given by B_0'. The two uncoupled open and closed energy levels are respectively given by the blue ϵ_P and red ϵ_Q curves. This figure is reproduced from the PhD thesis of M. Goosen.[6]

The next step is to set equation 4.43 equal to equation 4.14, and as a result the scattering length near the resonance goes as

$$a(B) = \frac{A}{2\kappa_P \left|\epsilon_P\right| \mu_{rel}(B - B_0)}. \tag{4.44}$$

Near a resonance equation 4.13 becomes $a(B) = a_{bg}\frac{\Delta B}{B-B_0}$. Consequently ΔB can be written as

$$\Delta B = \frac{A}{a_{bg} 2\kappa_P \left|\epsilon_P\right| \mu_{rel}}. \tag{4.45}$$

Under the assumption that only one bound state is dominant in the open, and one is dominant in the closed subspace, the field width can be written without the actual use of the continuum states.

4.3.2 To obtain the field width ΔB

In this thesis a variation of equation 4.45 is used to obtain the field width, as a substitution is made for parameter A.

Recall that A is equal to $\langle\phi_Q| H_{QP} |\Omega_P\rangle \langle\Omega_P^D| H_{PQ} |\phi_Q\rangle$, which represents coupling between an eigenstate of H_{PP} and H_{QQ} by H_{PQ} and H_{QP}. To obtain its value, we need to return to the total Hamiltonian.

The total Hamiltonian written in the pair basis of the internal Hamiltonian, allows the different open and closed channels to be identified.[6] Hence H^{Tot} can be easily divided into its

four parts (equation 4.15). At the diagonal the 'bare' bound states are positioned, the binding energies in the absence of coupling between the channels. The energies are defined relative to the threshold of the entrance channel.
It is assumed that in $\mathcal{P}$ only one channel exists, from which one single bound state needs to be considered. As a result H_{PP} has only one single element, which is equal to ϵ_P with bare bound state $|\Omega_P\rangle$.
Parameter A is a function of (amongst others) the eigenstates of $\mathcal{Q}$. Therefore H_{QQ} is written in its eigenstate basis $\{|\phi_{Q_1}\rangle, |\phi_{Q_2}\rangle, \ldots\}$ and as consequence has the eigenvalues $\{\epsilon_{Q_1}, \epsilon_{Q_2}, \ldots\}$ on its diagonal. This diagonalisation is to be done without affecting the $\mathcal{P}$ subspace. After the basis transitions, H_{PP} and H_{QQ} are diagonal in the $\{|\Omega_P\rangle, |\phi_{Q_1}\rangle, |\phi_{Q_2}\rangle, \ldots\}$-basis. The coupling strength between the open and closed eigenstates is then given by H_{PQ} and H_{QP}.
The field width is determined under the assumption that only one open and one closed bound state are near the threshold. This means that if we identify the bound state of closed channel $|\phi_{Q_i}\rangle$, $\langle\phi_{Q_i}| H_{QP} |\Omega_P\rangle$ is equal to the ith entry of H_{QP} which is defined as $\mathcal{K}$.
In short, H^{Tot} has to be written in the pair basis of the internal Hamiltonian to identify the open and closed subspaces. Then by rewriting H^{Tot} in such a way that independent from one another H_{PP} and H_{QQ} are diagonal in the basis of their eigenstates, the coupling elements of H_{PQ} and H_{QP} give the value for A, namely $A = \mathcal{K}^2$.[4]

The dressed bound state crosses the threshold at B_0, at the threshold $E = 0$ and equation 4.35 results into

$$\epsilon_P \epsilon_Q = \frac{\mathcal{K}^2}{2}. \tag{4.46}$$

By substituting this relation into the expression for ΔB (equation 4.45), one can rewrite the equation as

$$\Delta B = \frac{2\epsilon_P \epsilon_Q}{a_{bg} 2\kappa_P |\epsilon_P| \mu_{rel}}, \tag{4.47}$$

$$= \frac{a^P}{a_{bg}} \frac{-\epsilon_Q}{\mu_{rel}}, \tag{4.48}$$

$$= \frac{a^P}{a_{bg}} \left(B_0 - \tilde{B}_0\right), \tag{4.49}$$

where $a^P = 1/\kappa_P$ and $\tilde{B}_0$ is the magnetic field at which ϵ_Q crosses the threshold.

So instead of using equation 4.45 to determine the field width, equation 4.49 is used. At the threshold one can search the magnetic field for which the relation of equation 4.46 holds and the resulting magnetic field is B_0. This is done by evaluating H^{Tot} as stated above, the $\mathcal{K}$ element is obtained from the H_{QP} or H_{PQ} and ϵ_P and ϵ_Q are gained at the diagonal of the matrix. The magnetic field at which ϵ_Q crosses the threshold, results in the value for $\tilde{B}_0$. The bound state of the open channel is the only element of H_{PP} from which a^P can be obtained. So all information to obtain the field width is included in the Hamiltonian, it is just a matter of finding it.

Chapter 5

Towards solving the puzzle

The search for the right values of the three free parameters is presented in this chapter. A consistent set of values should give resonance positions which agree with the measured resonances. Before the analysis is presented, the experimental results are introduced in the first section of this chapter.

In the next section, the solution space of the three free parameters is identified and reduced. These three free parameters are the relative singlet and triplet s-wave bound state energies (ϵ_S and ϵ_T) and the Frank-Condon factor η for which $S \neq S'$. The Frank-Condon factor will be left to fine-tune the system and hence the reduction of the solution space focuses on the values of ϵ_S and ϵ_T.
The reduction of the triplet parameter is based on the analysis of one resonance, which gives a discrete set of possible values. For the singlet parameter an upper and lower bound is found.

The resonances are then studied in the reduced solution space. Each measured resonance can be explained by a bound-state energy curve for which its intersection with the threshold corresponds to the resonance. Therefore all possibilities will be studied for which a selected set of resonances is represented by a combination of bound-state energy curves. The selected set of resonances is first divided into two subsets according to the magnetic field range, for which the results are later combined. In the end several possible assignments are found, each describes a different scenario.

In the third section the different scenarios are further explored. First the best values for the free parameters are found, for each scenario. The best scenarios are then explored in the light of the remaining resonance spectrum (for which only the resonances in the lowest energetically channels are considered). Then for each final scenario the parameter values are found, for which most of the spectrum can be explained.
Finally the final scenarios are tested using the field width description, and the obtained width information for each case is compared to experimental information.

5.1 Measured resonances

To analyze the ^{23}Na^{6}Li system, experimental data is crucial. Due to the inaccurate potentials, reliable predictions can only be made with the use of experimental determined resonances. Two earlier publications were based on the analysis of only three resonances by Gacesa et

al.[2] and Stan et al.[1]. When in Heidelberg more resonances were measured, it became clear that the predictions from these analyses were incorrect. However, these newly measured resonances also give us the opportunity to do a better analysis of the interaction parameters, which are consistent with all measurements.

The three resonances on which the two earlier publications rely on are given in table 5.1.

M_F 3/2	
$\|1,1\rangle \|1/2,1/2\rangle$	
B_0 [G]	Ramp speed [G/s]
746.0	15
759.6	0.3
795.6	10

Table 5.1: The three resonances obtained from Stan et al.[1]

These resonances where found by sweeping the magnetic field across a resonance. The atomic loss was recorded and the sweep rate was chosen in such a way that 50% of the atoms was converted into molecules. The faster the sweep rate the stronger the interaction strength, hence the broader the field width (equation 4.45). Therefore this sweep-rate can be taken as a measure to determine the hierarchy of field widths, the faster the sweep-rate the broader the width.

In the group of Prof. Oberthaler, they were able to measure up to 24 resonances, divided over several entrance channels. An overview of those resonances is shown in figure 5.1. Each curve represents the threshold of an entrance channel as function of the magnetic

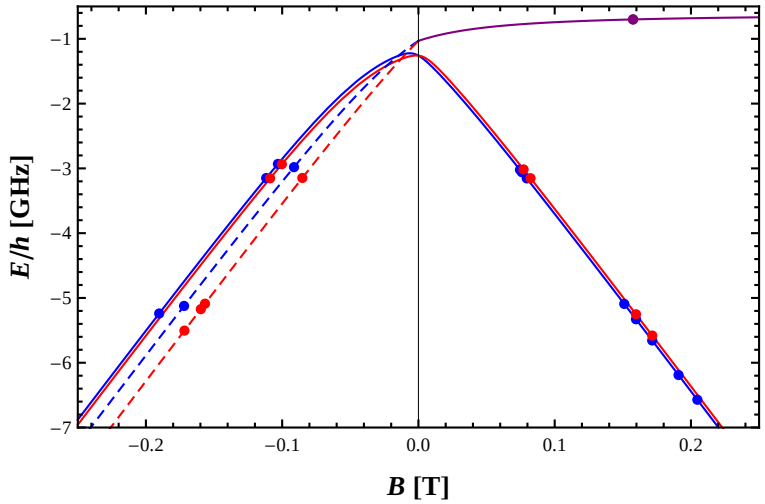

Figure 5.1: The entrance channels (curves) with the corresponding measured Feshbach resonances (dots) as function of the magnetic field. The different colors indicate different M_F-values (blue $M_F = 1/2$, red $M_F = 3/2$ and purple $M_F = 5/2$). The line styles distinguishes the different M_F channels of the different two particle states (the purple solid $|1,1\rangle|3/2,3/2\rangle$, the red solid $|1,1\rangle|1/2,1/2\rangle$, the red dashed $|1,0\rangle|3/2,3/2\rangle$, the blue solid $|1,1\rangle|1/2,-1/2\rangle$ and the blue dashed $|1,-1\rangle|3/2,3/2\rangle$).

field. The measured resonances are represented by the dots. The channels have been divided by their good quantum number M_F and every M_F has been subdivided by their two particle representation, $|f_{Na}, m_{f_{Na}}\rangle\,|f_{Li}, m_{f_{Li}}\rangle$.
The data of the figure is also given in table 5.2. In this table the position B_0 and the hold time τ of each resonance is given. The hold time is basically equivalent to the decay time on resonance. The value of τ gives an indication of the broadness of the field width. As the hold time is large it indicates a small interaction strength (and vice versa), the smaller the interaction strength the smaller ΔB, hence $\Delta B \sim \frac{1}{\tau}$. This relation will not give the exact value of ΔB, but it does point out the hierarchy of resonances according to their field width.

When this work was going on, more and more resonances were measured. The three most recently measured resonances are not yet completely characterized. They are therefore not as accurate as the other measurements. These three points are only used to verify the predictions based on the other resonances. These three resonances are given in the table 5.2 by in a bold font representation.
Note that, both tables give the same results for the three resonances in position and width hierarchy.

M_F 1/2				M_F 3/2				M_F 5/2	
$\|1,1\rangle\,\|1/2,-1/2\rangle$		$\|1,-1\rangle\,\|3/2,3/2\rangle$		$\|1,1\rangle\,\|1/2,1/2\rangle$		$\|1,0\rangle\,\|3/2,3/2\rangle$		$\|1,1\rangle\,\|3/2,3/2\rangle$	
B_0 [G]	τ [ms]	B_0 [G]	τ [ms]	B_0 [G]	τ [ms]	B_0 [G]	τ [ms]	B_0 [G]	τ [ms]
771.8	100	-852.0	1000	745.2	25	-913.2	190	1575.8	500
822.9	1000	-1566.3	1000	759.0	2000	**-1720**			
1596.75	100	**-1597**		795.2	90				
1716		-1717.3	750	1510.4	250				
-1002.3	50			1596.5	25				
-1088.5	50			1715.6	250				
				1908.9	1500				
				2046.9	50				
				-1031.69	50				
				-1117.3	150				
				-1902.4	750				

Table 5.2: The 24 resonances measured in the group by Prof. Oberthaler.

5.2 Exploring and reducing the solution space

As stated before, the focus of this study is to find the values of the three free fit parameters with which the whole system can be described. Those free fit parameters are the relative singlet and triplet s-wave bound state energies (ϵ_S and ϵ_T) and the Frank-Condon factor (η) when $S \neq S'$, respectively referred to as singlet and triplet energy and the overlap.

Resonances caused by bound-states with partial waves with $l > 2$ are not taken into consideration while analyzing the system. They are neglected as their chance to be detected is very small due to the presence of the centrifugal barrier. Hence the system is examined considering only s-, p- and d-wave molecular states. Each partial wave leads to a spectrum of bound-state energy curves as a function of the magnetic field. The curve spectrum is in essence the same for all three partial waves, only energetically shifted (due to centrifugal barrier).
When the three parameters are correctly determined, the intersection of the energy curves with the threshold should agree to the measured resonances. In the search for this correct set, the many energy curves and measured resonances would lead to a case of numerous of possible situations which all need to be considered. It would be hard to keep an overview while evaluating the system. Therefore it is necessary to reduce the solution space of the three free parameters as much as possible, and hence the number of possible situations. This will be the purpose of the first subsection after which the assignment of the energy curves to the measured resonances will be studied.

5.2.1 Systematically reducing the solution space

First the solution space needs to be defined. From figure 3.6 one can see that if the bound states are lower than -13 GHz in the potential well, a 'new' bound state enters the well and is thereby the least bound state. As a result the least bound states will be positioned in the relative energy region between 0 and -13 GHz.
The overlap or Frank Condon factor lies between -1 and 1. The overlap value is necessary to solve the determinant of equation 4.11, however a positive or negative overlap value results in the same determinant. Therefore to solve the resonance spectrum, the absolute value of the overlap is sufficient.

However the solution space gives room for a large set of possible parameter combinations and hence should be minimized. The solution space can be systematically reduced by evaluating several resonances, from which an overall conclusion can be drawn. It appears that the options for the triplet parameter can be reduced to six discrete values due to a single resonance in the $M_F = 5/2$ channel. The measured resonances of the $M_F = 3/2$ channel are also a dominant factor in reducing values for the singlet parameter. This process will now be evaluated.
The overlap value will be left as fit parameter between 0 and 1.
The road map of this subsection in reducing the solution space will be:

- A) Reducing the triplet parameter to a limited set of values.
- B) Set the upper bound for the singlet parameter.
- C) Gain a lower bound for the singlet parameter.

Step A: Reducing the triplet parameter to a limited set of values.

In the $M_F = 5/2$ channel, there is only one resonance measured at 1575.8 G. In this channel each partial wave has two bound-state energy curves which cross the threshold by positive magnetic fields. This is shown in the left graph of figure 5.2; the different colors resemble different partial waves, blue for s-waves, green for p-waves and pink for d-waves.

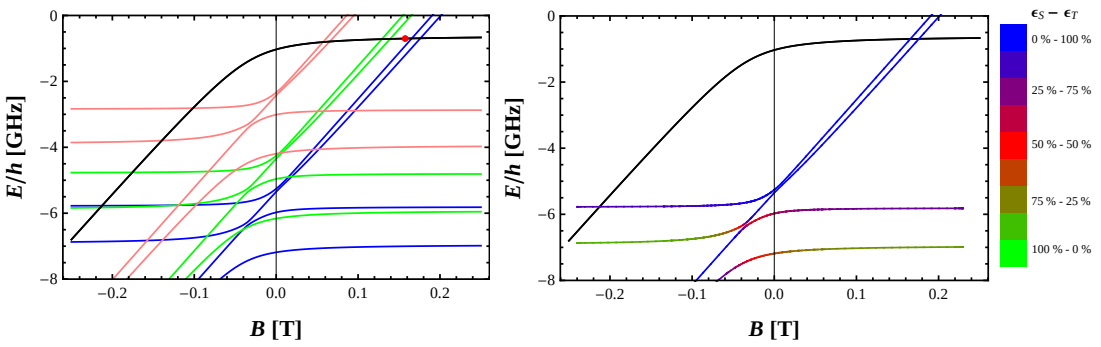

Figure 5.2: The $M_F = 5/2$ channel with one measured resonance at 1575.8 G. The left graph shows the bound state energy curves and the threshold; blue for s-waves, green for p-waves, pink for d-waves and black for the threshold. The right figure shows the energy curves of one partial wave and their dependence on ϵ_S and ϵ_T, which is indicated by the different colors given in the legend. (The graphs are made by the parameter combination $\epsilon_S = -6.73$ GHz, $\epsilon_T = -6.0$ GHz and $\eta = 0.74$.)

The right graph of figure 5.2 shows the fraction of ϵ_S and ϵ_T to each energy curve, as each coupled bound-state is a superposition of the ϵ_S and ϵ_T-states. This singlet and triplet parameter distribution over the curves has the same behavior for all three the partial waves. The right graph demonstrates that if the singlet parameter has a low enough value, then the energy curves passing the threshold are only determined by the triplet parameter (only positive magnetic fields are considered). Hence the positions of intersection will be mainly defined by ϵ_T. Note that the graphs just give an indication of the bound-state energy landscape, as their parameter combination is chosen more or less arbitrary.
In total there are six energy curves which could explain the resonance. Hence the triplet parameter could reduce to six discrete possibilities. This is shown in figure 5.3, where the singlet and triplet parameter span the solution space. Since the overlap parameter is of lesser importance than the two other parameters, we don't put this third parameter explicitly in the solution space with a third axis. However, we keep in mind that the curves in the solution space are connected to a certain value of the overlap, where the latter is in between 0 and 1. The figure is obtained by evaluating the system for three different values of the overlap, namely $\eta = 0.4$, 0.7 and 1. By each overlap value, the combination of ϵ_S and ϵ_T is determined for which an energy curve intersects the threshold at 1575.8 G.
The six different lines are labeled according to their partial wave and order of bound-state crossing with the threshold.
The different overlap values give an indication of its influence on the system. The overlap value only matters as the singlet energy approaches -0.7 GHz.

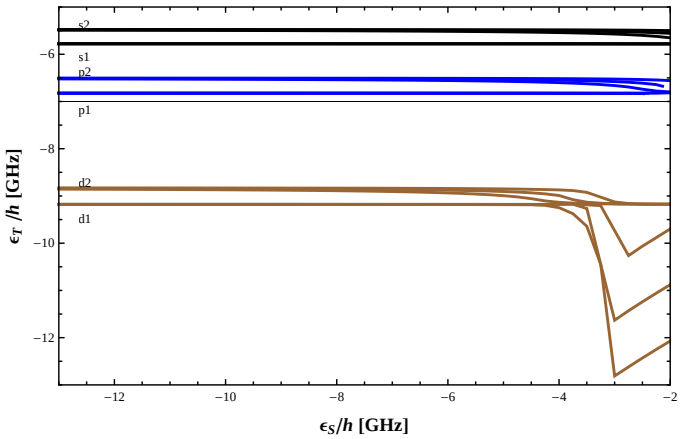

Figure 5.3: The singlet and triplet parameter combinations for which one resonance is obtained at 1575.8 G. The combinations are made for three fixed values of the $\eta = 0.4$, 0.7 and 1, where the most curved lines have the largest overlap value. As smaller overlap values, result in less interaction between ϵ_S and ϵ_T. The sets are labeled by the energy curve that accounts for the measured resonance. The energy curve is given by the combination of partial wave (black s-waves, blue p-waves and brown d-waves) and a number, which indicates the order of crossing the threshold (from low to high magnetic fields).

The combinations resulting from the d-waves (the brown sets) seems to behave strange for the smallest singlet energies in the plot. However, this is caused by the horizontal energy curves approaching the threshold as the singlet energy approaches -0.7 GHz.

So there are six possible scenarios which can explain the resonance in the $M_F = 5/2$ channel and are mainly characterized by the value of ϵ_T. From figure 5.3 it is found that three scenarios are almost independent of ϵ_S and overlap and result into the triplet energies of -5.78 GHz, -6.82 GHz and -9.18 GHz. The error bar in these triplet values will be mainly determined by the measurement uncertainty and the interaction with the threshold. If there is for instance a 10 G deviation in the measurement and/or calculation, the error will be at max 0.05 GHz. The other three go asymptotically to -5.47 GHz, -6.50 GHz and -8.83 GHz for low values of the singlet energy. The maximum deviation which needs to be considered with respect to these asymptotic values depends mainly on how far the singlet parameter can be reduced.

An additional channel needs to be considered in order to excluded at least one of the six triplet scenarios. Therefore the next step is to review the $M_F = 3/2$ channel.
The bound-state energy landscape in the $M_F = 3/2$ channel is indicated by the curves of figure 5.4. At first glance it may look like spaghetti, but do not get discouraged. The color coding is the same as the previous representation of the $M_F = 5/2$ channel. For positive magnetic field, there are eight resonances measured and each partial wave has seven bound-state energy curves which are able to cross the threshold.

The ϵ_S,ϵ_T-mixing figure (the right plot of figure 5.4) indicates that curves can be divided into sets, from high energetic to low, the first three are mainly determined by the triplet

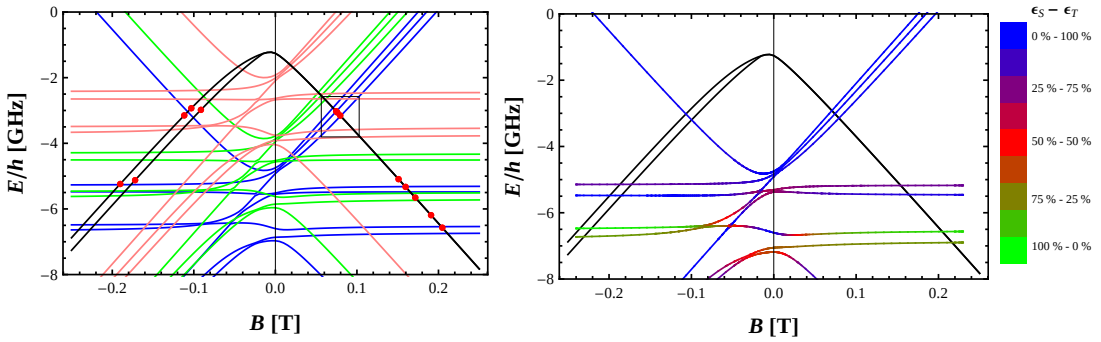

Figure 5.4: The $M_F = 3/2$ channel which has for positive magnetic fields eight measured resonances. Each partial wave has seven bound state energy curves which can cross the threshold by positive magnetic fields. The left graph shows the distribution of the different partial energy curves (s-waves blue, p-waves green, d-waves pink and threshold black), with three measured resonances in the black square. The graph on the right, demonstrates the ϵ_S and ϵ_T contribution of each curve, obtained for one partial wave and given by the different colors in the legend. (The graphs are made by the parameter combination $\epsilon_S = -6.5$ GHz, $\epsilon_T = -5.49$ GHz and $\eta = 1$.)

energy provided that the singlet energy has a low value. The other four come into sets of two, for which one set is determined mainly by the singlet energy and the other by the triplet value (the order of appearance depends on the ϵ_S and ϵ_T-values). These last four states will be more mixed as the given singlet and triplet parameter approach the same value.

So the six triplet scenarios determine mainly all possible positions of the first three bound-state energy curves. It turns out that for all six cases, the first three energy curves of one particular partial wave are near the first three measured resonances. The resonances are highlighted by the black square in figure 5.4 (left side). The partial wave which describes one of the six triplet scenarios is also the partial wave which has its energy curves near the resonances. However in each case, when the threshold crossings are compared to the measured resonances, the measured resonances are closer to each other than the energy curves indicate (shown in figure 5.5 for the d-waves).

Now we consider the resonance of the $M_F = 5/2$ channel explained by a d-wave, so either d1 or d2, and consequently the first three resonances of the $M_F = 3/2$ are surrounded by d-waves. Figure 5.4 shows that the centrifugal barrier shift, puts the d-wave curves energetically much higher than the s- and p-waves. As a result it is not an option, to combine this triplet scenario with the presence of other partial waves to explain the three resonances. (It could do the trick if the singlet energy is positioned high in the potential well around -4 GHz, however as we will show later this value lies outside the singlet solution space.) The remaining option for this triplet scenario is that the three resonances are caused by only d-waves, for which the singlet energy enables an avoided crossing of the energy curves near the threshold.

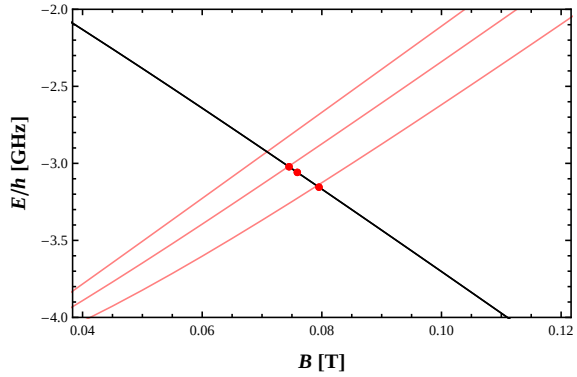

Figure 5.5: A zoom-in of the three resonances indicated by the black square in Figure 5.4. The set of three bound-state energy curves as the ϵ_T is set to -8.86 GHz, as function of the magnetic field. The threshold is given by the black curve and the first three measured resonances by the red dots.

It results in two options for which the three resonances are explained by only d-waves and ϵ_T has a value in the range of -9 GHz. The two possible cases are given by the parameter combinations:

$$\epsilon_S = -6.406 \text{ GHz}, \epsilon_T = -9.387 \text{ GHz and } \eta = 0.849,$$
$$\epsilon_S = -6.730 \text{ GHz}, \epsilon_T = -9.077 \text{ GHz and } \eta = 0.741.$$

Both cases are shown in figure 5.6.
The triplet energy calculated for both cases does not correspond to one of the earlier found values (-8.86 GHz and -9.18 GHz). Next to that the two scenarios are also not able to explain the other five resonances measured in the channel. In appendix B.1, the energy curve distribution in the $M_F = 3/2$ channel of both cases is presented, from which we conclude that these parameter combinations should be excluded from the solution space.

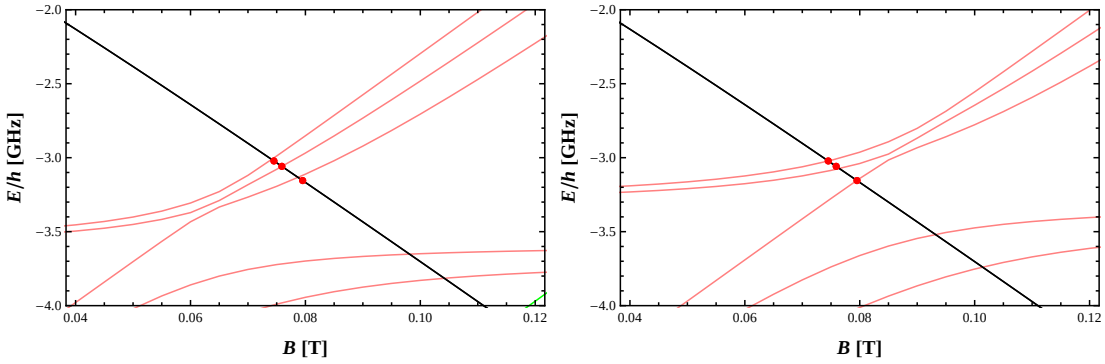

Figure 5.6: The two options for the first three resonances of the $M_F = 3/2$ channel to be explained by the d-waves. Left graph is given for the parameter combination $\epsilon_S = -6.73$ GHz, $\epsilon_T = -9.077$ GHz and $\eta = 0.741$ and the right graph for the combination $\epsilon_S = -6.406$ GHz, $\epsilon_T = -9.387$ GHz and $\eta = 0.849$

Consequently the measured resonance in the $M_F = 5/2$ channel can not be explained by a d-wave, as it leaves no option to explain the resonances measured in the $M_F = 3/2$ channel. Therefore the triplet parameter candidates can be limited to four possibilities.

Out of curiosity, the possibility that the first three resonances in the $M_F = 3/2$ channel are caused by pure s- or p-waves is also examined. Those would lead again to two options per partial wave. However based on the overall picture of the channel, those combinations would not lead to explanation of the other resonances. The corresponding figures are shown in Appendix B.2 and B.3.
So the first three resonances of the $M_F = 3/2$ channel can only be caused by a combination of different partial waves.

Step B: The upper bound of the singlet parameter

The triplet parameter is narrowed down to four small energy regions, however the singlet parameter could be any value between 0 and -13 GHz. Again the $M_F = 3/2$ channel could lead to reduction. Now the last five resonances need to be examined. An indication of the channel is given in the case of a high value for the singlet energy, by figure 5.7 where the five resonances are indicated by the black box.

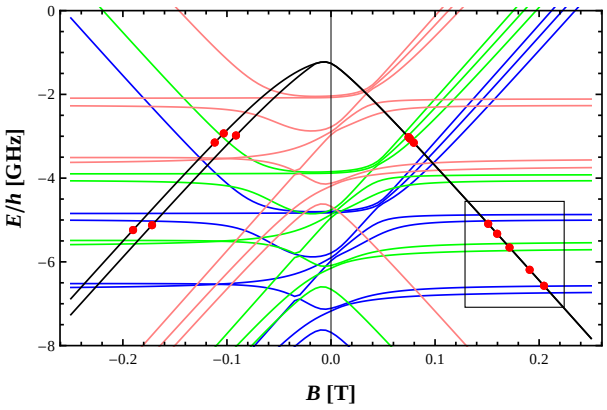

Figure 5.7: The $M_F = 3/2$ channel in case of a low value for the triplet energy and a high value for the singlet energy. The figure is made with the parameter combination of $\epsilon_S = -5$ GHz, $\epsilon_T = -6.53$ GHz and $\eta = 1$.

There are two criteria to be found from these resonances. The first is that the lowest s-wave energy curve must cross the threshold at or below the last resonance in the channel. If this is not the case, there are no threshold crossings which are able to explain the last resonance as they are all positioned at lower magnetic fields. The second results from the scenario that ϵ_T has a low value and ϵ_S a high value. In that case below the 5^{th} s-wave, there could be at max six energy curves, namely two s-waves, two p-waves and two d-waves. However due to the centrifugal barrier shift, the vertical distance between the two d-waves and two s-waves curves exceeds the size of the black box. As a result there are below the 5^{th} s-wave only four options to explain the five resonances. Therefore the second criteria states that the 5^{th}

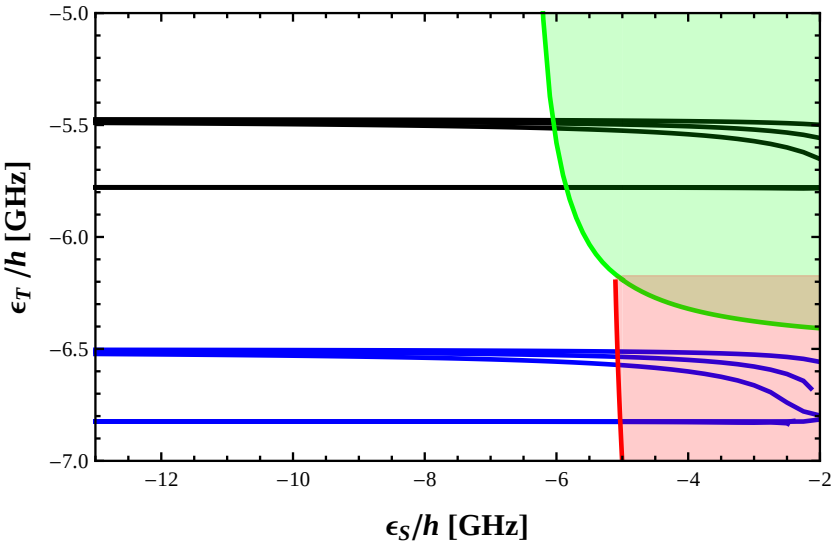

Figure 5.8: The upper bound for the singlet parameter. The green curve is border based on the first criteria, all parameter combinations above the green curve (green area) are excluded from the solution space. The red curve is the upper boundary resulting from the second criteria; which excludes all combinations in the red area from the solution space.

s-wave energy curve must be positioned at or below the first resonance of the set of five. The results of these criteria are indicated in figure 5.8 by exclusion zones, where also the four options for the triplet energy are shown. The green curve is obtained for those singlet and triplet energy combinations, which lead to last s-wave crossing at the last resonance by an overlap of 1. The green area above the curve, contains all the combinations which positions the last s-wave crossing above the last resonance. Therefore the green area marks the region which can be ruled out of the solution space, due to criteria one. The overlap value of 1 was chosen for the boundary criteria as it encloses only the minimal area which can be excluded. It also shows that if the triplet energy would have a value lower than roughly -6.4 GHz, the singlet energy is not limited anymore. However for high values of the singlet energy, there are way too less states to explain the five resonances.

This is covered by the second criteria, given by the red curve. This curve is obtained by those triplet and singlet combinations that yield in the 5^{th} s-wave crossing at the first resonance in the set of five. The overlap value is again set to 1, it would give the minimal criteria as the triplet and singlet values are not too close together. So due to criteria two all combinations for singlet values lower than -5 GHz, would lead to no solutions for the system.

In other words, the two criteria give us the upper bound of singlet energy, and it can safely be said that the singlet energy must be below the -5 GHz.

Step C: The lower bound of the singlet parameter

The upper bound has been obtained however nothing is said of the lower bound. It is hard to give a lower bound from which it is clear that a certain solution area is eliminated. However, when plotting the graphs for the reduced values of the triplet energy and shifting the singlet energy from -13 GHz to higher values, it becomes clear that just by eye the lowest values do not make sense for ϵ_S. It can not explain the last five measured resonances in the $M_F = 3/2$ channel.
So by hand, the singlet energy is shifted upwards from -13 GHz and the result is examined carefully. As there are no hard borders and examination is done by hand, the lower bound is drawn at a place where it is safe to say that certainly no solutions can be found. The result is that for a triplet energy in between -5 and -7 GHz, the singlet energy must be above -8 GHz by all possible overlap values. This process explained by graphs can be found in Appendix B.4.

Conclusions so far

To summerize, the following conclusion can be drawn from evaluating the initial solution space:

- The overlap value should be between 0 and 1.
- The triplet energy has four options, namely -5.78 GHz,-6.82 GHz, between the -5.47 till -5.52 GHz and -6.50 till -6.57 GHz, all with an error bar of 0.05 GHz.
- The singlet energy lies in the range between the -8 and -5 GHz.
- The first three resonances in the $M_F = 3/2$ channel can only be caused by a combination of partial waves.

5.2.2 Assigning the resonances

The measured resonances correspond to bound-state energy curves intersecting the threshold. The solution to the measured resonance spectrum requires therefore the correct assignment of the resonances to the energy curves.
Each resonance can be justified with at least one energy curve. In case of the measured resonances, each of their positions can be explained by several options. Therefore not only the candidates per resonance must be considered but also their consistency with respect to the whole resonance spectrum. As a result, it is possible to exclude scenarios as they lead to inconsistent results with the spectrum. In the ultimate case there would be one explanation left, i.e. only one energy curve combination with which all resonance positions will be explained and the three free parameters uniquely determined. It is the purpose of this subsection to find those energy curve combinations that lead to an explanation of a selected set of resonance positions.

The analysis is made as follows, first one resonance is selected for which all possible partial bound states are identified. For each bound state, the intersection with the threshold is calculated as function of the singlet and triplet energy by a fixed value for the overlap (0.4, 0.7 or 1). From those results all the singlet and triplet combinations are obtained for which the intersection at the threshold corresponds to the measured resonance. Due to the three different overlap values there are three different combination sets per resonance-energy curve assignment. The solution space enclosed by the three different combination sets, gives all the possible singlet and triplet combinations for which its overlap value varies between 0.4 and 1. From working with the system for almost a year, experience tells that the overlap value should probably be found above the 0.5. Just to be sure, overlap values of 0.4 are even considered.
The possible two parameter combinations (singlet and triplet energy) can be visualized in a contour plot. The contour plot has on its axis the singlet and triplet energy, the overlap value is not explicitly given. This means that even though three free parameters are searched after, the information is translated into a two dimensional plot. In other words, if a parameter combination is drawn in the contour plot, it says that there is an overlap value for which the combination explains the resonance but does not define it.
As several resonances are analyzed, the results are combined. The selected resonances can be explained by those energy curve combinations for which their solution area overlap the same singlet and triplet energy combination.

In the previous subsection, the solution space has been reduced. The singlet parameter was found between -8 and -5 GHz. For the triplet value four different options were obtained, based on the one resonance in the $M_F = 5/2$ channel. Each of these options result in a subdivision of solution space. When a solution is found in one of these subspaces, it determines the energy curve which should explain the resonance in the $M_F = 5/2$ channel. The solution subspaces are visualized as gray area's in the contour plot. From high to low triplet energy, the first subspace is characterized by the 2^{nd} s-wave in the $M_F = 5/2$ channel, the second subspace by the 1^{st} s-wave, the third by the 2^{nd} p-wave and the last subspace by the 1^{st} p-wave (figure 5.3).

For this analysis only the resonances in the lowest energy channels are considered. The reason for this is that for resonances in energetically higher entrance channels, the bound-state energy curves has to intersect at least two thresholds. The influence of the additional intersection with the lower lying threshold on the calculated resonance positions in the higher entrance channel is not known.

To consider all the resonances at once it would result in a numerous set of combinations, and the overview is quickly lost. Therefore a selected set of resonances is analyzed. This set is divided into two groups, one contains the last five resonances of the $M_F = 3/2$ channel by $B > 0$ and the other the 1^{st} resonances in the lowest energy channels with $M_F = 1/2$ and $M_F = 3/2$ for $B < 0$.

The last five resonances in the $M_F = 3/2$ channel for $B > 0$.

The last five resonances in the $M_F = 3/2$ channel at positive magnetic field are analyzed first. It forms a firm basis as there are a good number of resonances measured and there is a more limited set of energy curves available with respect to the $M_F = 1/2$ channel. For each resonance its options are studied in combination with the four solution subspaces. The results are then combined and examined in the light of the whole resonance subset.

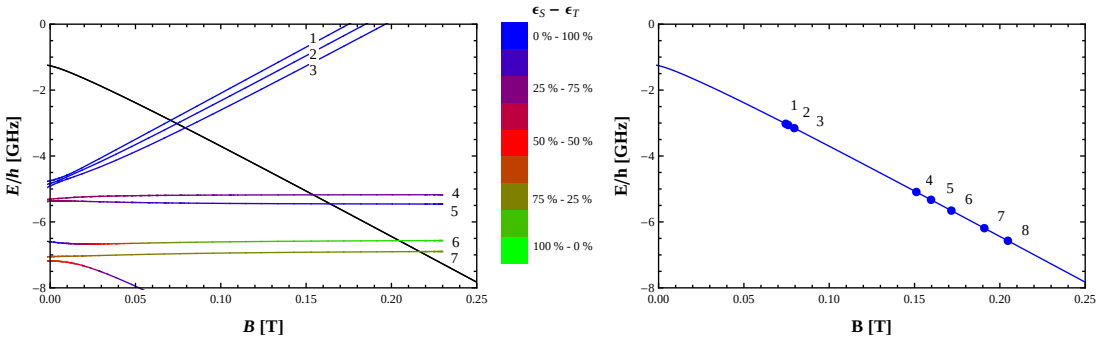

Figure 5.9: The $M_F = 3/2$ channel for $B > 0$. The left graph shows the energy curve distribution of one partial wave. The colors indicate the singlet and triplet energy mixing and are given in the legend. The energy curves are plotted by a parameter combination $\epsilon_S = -6.5$, $\epsilon_T = -5.49$ and $\eta = 1$. The right curve shows the numbering of the eight resonances.

In order to keep an overview the resonances and the energy curves are labeled. Each energy curve is given the letter of the corresponding partial wave (s, p and d) and a number obtained from the order of their appearance, from high energy to low. The numbering is shown in the left graph of figure 5.9. In this graph the energy curves are plotted for one partial wave with their colors indicating the ϵ_S,ϵ_T-dependence.
The resonances are labeled by "Res" followed by a number, which is determined from the order of appearance on the threshold from high to low energy and a distinction is made between positive and negative magnetic fields. The numbering is shown in right graph of figure 5.9.
All possible energy curves that could explain one of the five last resonances are given by the table 5.3. The table must be read row for row, so each row gives all the possible energy curves of the resonance, which is stated in the first column. The color indication is used later in contour plots.

The resonances and possible energy curves are now identified, and each resonance can be examined in the solution space. The result of the analysis of these five resonances is shown in figure 5.10, page 52. Each graph represents one resonance for which its possible energy curves are studied in the contour plot for three overlap values (0.4, 0.7 and 1). Each energy curve is indicated by a color stated in table 5.3. The combinations given by the lighter colors, are those combinations for which the theoretically determined position and measured resonance position have a separation of 10 G. It widens the solution area for each energy curve and hence room for an error in the calculations is incorporated.
These graphs can be combined to gain those energy curve combinations which are able to

Resonance	Bound state energy curve								
Res4			s5	s4	p7	p6	p5	p4	d7
Res5			s5	s4	p7	p6	p5	p4	
Res6			s5	s4	p7	p6	p5		
Res7		s6	s5	s4	p7	p6			
Res8	s7	s6	s5	s4	p7	p6			
color	green	brown	purple	blue	red	orange	magenta	cyan	black

Table 5.3: The last five measured resonances in the $M_F = 3/2$ channel, and each partial wave bound-state energy curve which could explain the resonance. The color indication is used in the following contour plots to indicate the energy curve which is used to explain a measured resonance.

explain the five resonances. It would be one big mess to show it, however carefully all possible combinations are compared one by one. The final result is shown in table 5.4. There are in total six scenarios obtained based on these five resonances. From these scenarios it is concluded that the total solution space is reduced from four subspaces into three, as solutions are only found in three of the four subspaces.

Res1 $M_F = 5/2$	s1			s2	p2	
Res8 $M_F = 3/2$	s7	s7	s7	s7	s6	s6
Res7 $M_F = 3/2$	s6	s6	s6	s6	s5	s4
Res6 $M_F = 3/2$	s5	s5	s4	p7	p6	p6
Res5 $M_F = 3/2$	s4	p7	p7	s5	p5	p5
Res4 $M_F = 3/2$	p6	p6	p6	s4	p4	p4

Table 5.4: All possible explanations for the last five resonances in the $M_F = 3/2$ channel by the energy curves. The possibilities have been divided by the solution subspaces.

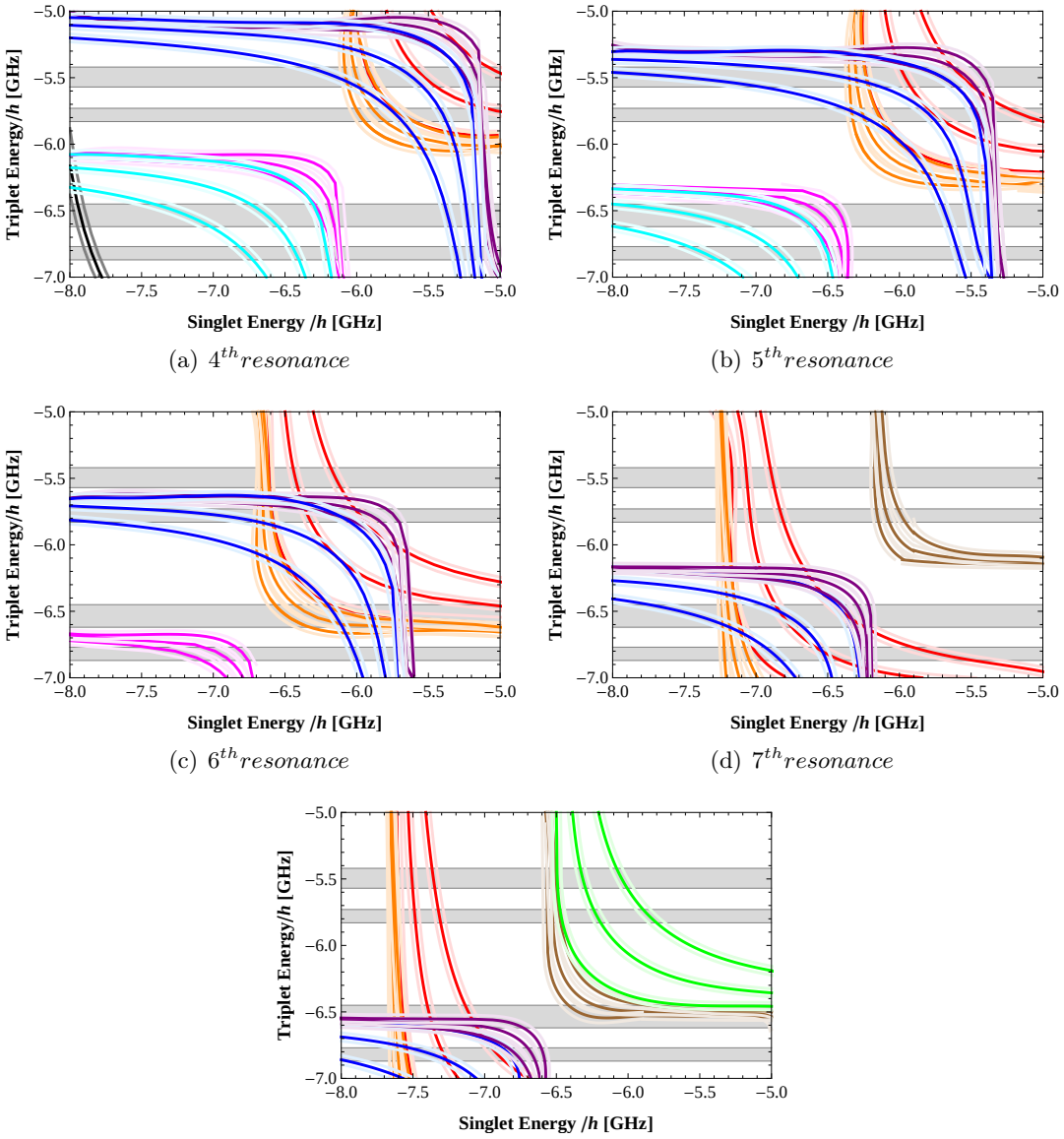

(a) $4^{th} resonance$

(b) $5^{th} resonance$

(c) $6^{th} resonance$

(d) $7^{th} resonance$

(e) $8^{th} resonance$

Figure 5.10: The contour plots made to explain the last five measured resonances in the $M_F = 3/2$ channel. Each singlet and triplet energy combination is made for the overlap values of 0.4, 0.7 and 1. The lighter curves indicate a theoretical and experimental mismatch of 10 G. The color coding is explained by table 5.3. The plots are named after the resonance which is analyzed.

The 1^{st} resonances in the lowest energy channels with $M_F = 1/2$ and $M_F = 3/2$

The second group of resonances is evaluated along the same line. This group only contains two resonances, which were measured at negative magnetic fields in the lowest channels of $M_F = 1/2$ and $M_F = 3/2$. During earlier evaluations, it was always hard to explain these resonances, therefore these resonances are considered for the second group.
The overview of the energy curves in each channel and the resonances is given in figure 5.11. The labeling is done the same way as with the previous resonance group.

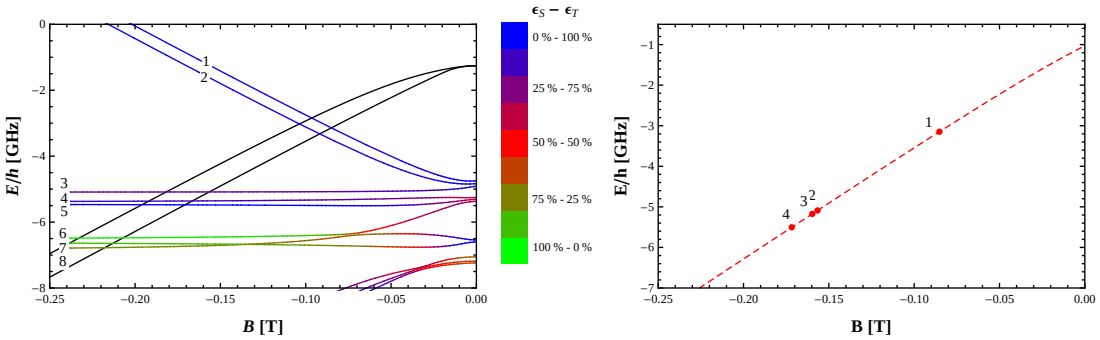

(a) $M_F = 1/2$

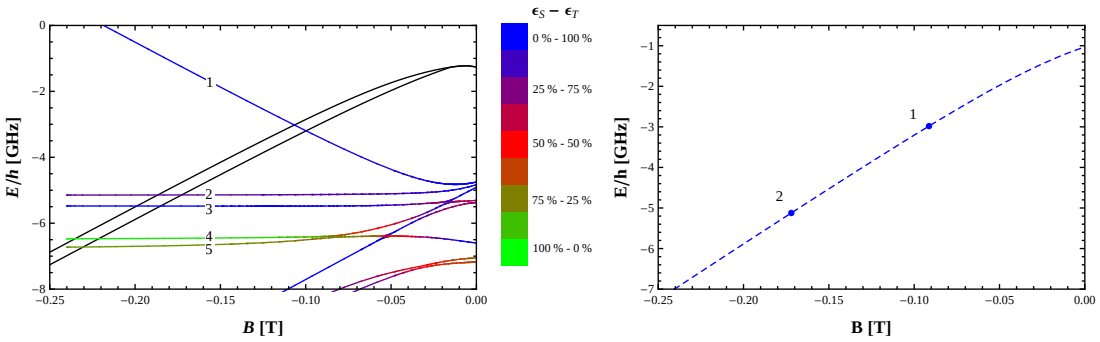

(b) $M_F = 3/2$

Figure 5.11: The lowest $M_F = 1/2$ and $M_F = 3/2$ channel for $B < 0$. The left graphs show the energy curve distribution of one partial wave. The colors indicate the singlet and triplet energy mixing, given in the legend. The energy curves are plotted by a parameter combination of $\epsilon_S = -6.5$, $\epsilon_T = -5.49$ and $\eta = 1$. The right curves show the numbering of the resonances in the channel.

Each resonance is assigned to a set of energy curves, which are stated in table 5.5. Note that the two resonances are explained by different energy curves in different channels, the labels could be the same however they are only valid within a given channel. As the number of possibilities exceeds the page width for the resonance in the $M_F = 1/2$ channel, they are divided over two rows.

Resonance	Bound state energy curve					
Res1 $M_F = 1/2(B < 0)$	s2	s1	p2	p1		
color	purple	blue	red	orange		
	d8	d7	d6	d5	d4	d3
	black	magenta	cyan	yellow	brown	green

Resonance	Bound state energy curve					
Res1 $M_F = 3/2(B < 0)$	s1	p1	d5	d4	d3	d2
color	blue	red	orange	purple	green	brown

Table 5.5: The assignment of measured resonances of the second selected group to all their possible energy curves.

Again each of these resonances are analyzed for the selected energy curves. The results are shown in the contour plots of figure 5.12. As there are many energy curve candidates for the resonance in the $M_F = 1/2$ channel, the contour plot became overcrowded. Therefore the results are divided over two plots.

Just as before the results are combined, and the combinations of energy curves are obtained for which both resonances are explained.

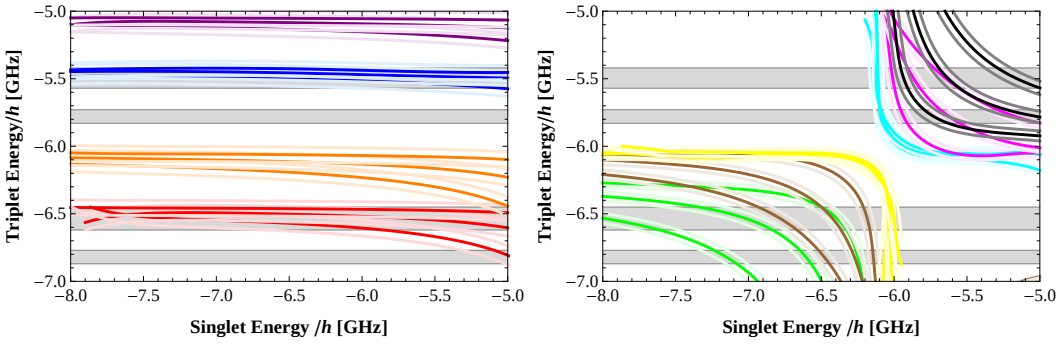

(a) 1^{st} resonance $M_F = 1/2$

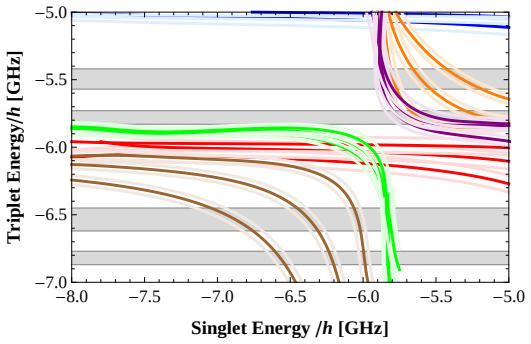

(b) 1^{st} resonance $M_F = 3/2$

Figure 5.12: The contour plot made to explain the measured 1^{st} resonance in the $M_F = 3/2$ channel for $B < 0$. Each singlet and triplet energy combination is made for the overlap values of 0.4, 0.7 and 1. The lighter curves indicate a theoretical and experimental mismatch of 10 G. The color coding is explained by table 5.5.

Those results are presented in table 5.6. One of the striking things obtained from this table is that $M_F = 3/2$ resonance can only be explained by d-waves.

Res1 $M_F = 5/2$	s1				s2					
Res1 $M_F = 1/2(B < 0)$	d8	d7	d8	d7	s1	d8	d7	s1	d8	d7
Res1 $M_F = 3/2(B < 0)$	d5	d5	d4	d4	d5	d5	d5	d4	d4	d4
Res1 $M_F = 5/2$	p1				p2					
Res1 $M_F = 1/2(B < 0)$	d5	d4	d3		p1	p1	d5	d4	d3	
Res1 $M_F = 3/2(B < 0)$	d2	d2	d2		d3	d2	d2	d2	d2	

Table 5.6: All possible energy curve combinations for the resonances of the second group.

The combination of the two subsets

So for the two selected resonance sets all the possible energy curve combinations are obtained. To come one step closer to solution for the whole system, both results are combined. This is shown in table 5.7. In this table all possible energy curve combinations are given which could explain the position of in total eight resonances (the resonance in the $M_F = 5/2$ channel is considered as well). The eight possible scenarios are numbered and given in table 5.7, where now each row indicates a possible energy curve combination.

nr	resonances							
	Res1 $M_F = 5/2$ $B > 0$	Res8 $M_F = 3/2$ $B > 0$	Res7 $M_F = 3/2$ $B > 0$	Res6 $M_F = 3/2$ $B > 0$	Res5 $M_F = 3/2$ $B > 0$	Res4 $M_F = 3/2$ $B > 0$	Res1 $M_F = 1/2$ $B < 0$	Res1 $M_F = 3/2$ $B < 0$
1	s1	s7	s6	s5	p7	p6	d8	d4
2	s1	s7	s6	s5	p7	p6	d7	d4
3	p2	s6	s5	p6	p5	p4	p1	d2
4	p2	s6	s5	p6	p5	p4	d4	d2
5	p2	s6	s5	p6	p5	p4	d3	d2
6	p2	s6	s4	p6	p5	p4	p1	d2
7	p2	s6	s4	p6	p5	p4	d4	d2
8	p2	s6	s4	p6	p5	p4	d3	d2

Table 5.7: All possible energy curve combination, for which the position of eight resonances is explained.

5.3 The most favorable scenarios

In the previous section, eight energy curve combinations were found for which it could explain the eight selected resonance positions. Those combinations could be divided into two sets. The best combination per set is obtained by evaluating the fits made for each curve combination to the corresponding resonances.
It is expected that the answer to the resonance spectrum, results in the best fit with the smallest χ^2. As a result in the first subsection the eight energy combinations are analyzed by fitting. The best solution(s) are then complemented with the remaining resonances in the lowest entrance channels (section 5.3.2). At last the calculated widths will be compared to the inverse of the measured hold times.

5.3.1 Fitting

The results of the last section can be divided into two sets, as both sets are located in different subspaces. The energy curve combinations in each set is very similar, there is a maximal difference of two resonances in the assignment of the eight resonances. As a result from each set one ultimate combination can be obtained by evaluating the best fit values for each scenario. The fit gives the best values for the three free parameters to explain the resonances for each combination.
The fitting has been done twice. Once for which the eight resonances are fitted by the three free fit parameters and for which two additional parameters are included. Those additional parameters are introduced to incorporated a possible error in the centrifugal barrier shift. The centrifugal barrier shift is determined by the assumption that the long range potential is sufficiently accurate. However, errors could result in a small difference in the barrier shift. To avoid that a possible error, would prohibit the finding of the best solution to the system these additional terms are added. They are indicated by δ_p and δ_d, respectively the change in the centrifugal barrier shift in case of p-waves and d-waves. The easiest way to incorporate these terms into the system, is by adding the δ to the centrifugal barrier shift function. The shift is given as function of the s-wave bound state energy, however with the additional terms the shift is now determined by the s-wave energy corrected by the δ-term.

The eight scenarios of table 5.7 are fitted with the three free fit parameters. The results are presented in the table 5.8, for which the numbers directly link to the scenario numbers in table 5.7. For each fit parameter the standard error is obtained and for every fit scenario the χ^2 of the system. The χ^2 is the sum of the squared difference between the theoretical and experimental resonance positions, that are considered for the fit. The value of the χ^2 gives an indication how well the fit could be made.
The first two combinations differ in one resonance assignment. This means that these scenarios are almost the same, only the assignment of one resonance is not decided yet. The best fit was found for scenario two.
The fit scenarios 3 till 8 have only differ on the assignment of two resonances. One can see that the fit scenarios 3, 4 and 6 are best. For which the χ^2 of the scenario 6 is slightly better.

The same scenario's are fitted for the second time, now with the additional parameters. The results are presented in table 5.9, as the table would exceed the page width the parame-

nr	ϵ_S [GHz]	$\Delta\epsilon_S$ [GHz]	ϵ_T [GHz]	$\Delta\epsilon_T$ [GHz]	η	$\Delta\ \eta$	χ^2 [G^2]
1	-5.92	0.20	-5.77	0.14	0.70	0.19	14939.6
2	-5.89	0.18	-5.78	0.12	0.75	0.16	10494.6
3	-6.35	0.09	-6.51	0.06	0.57	0.10	3691.17
4	-6.35	0.09	-6.51	0.06	0.58	0.10	3703.8
5	-6.32	0.10	-6.53	0.07	0.49	0.11	5556.92
6	-6.45	0.11	-6.49	0.07	0.56	0.08	3402.14
7	-6.44	0.12	-6.49	0.08	0.57	0.08	3929.29
8	-6.44	0.13	-6.50	0.08	0.52	0.08	4477.68

Table 5.8: The fit results for the eight scenarios of table 5.7 for the three free fit parameters.

ters of each case are divided over two rows.
The smallest χ^2 were obtained for the resonances with the nr 2 and nr 4. Those two fit cases are further analyzed in the following subsection, in which the result is generalized for the whole resonance spectrum. The fit scenario 4 is chosen above scenario 6 as, the χ^2 in the latest fit is much better for scenario 4.

nr	ϵ_S [GHz]	$\Delta\epsilon_S$ [GHz]	ϵ_T [GHz]	$\Delta\epsilon_T$ [GHz]	η	$\Delta\eta$
1	-6.11	0.09	-5.74	0.06	0.70	0.10
2	-6.07	0.08	-5.76	0.05	0.75	0.09
3	-6.34	0.05	-6.43	0.05	0.57	0.06
4	-6.34	0.04	-6.40	0.05	0.61	0.05
5	-6.33	0.13	-6.40	0.13	0.59	0.15
6	-6.44	0.08	-6.49	0.06	0.50	0.06
7	-6.44	0.08	-6.49	0.07	0.50	0.07
8	-6.43	0.16	-6.50	0.13	0.48	0.13

nr	δ_p [GHz]	$\Delta\delta_p$ [GHz]	δ_d [GHz]	$\Delta\delta_d$ [GHz]	χ^2 [G^2]
1	0.14	0.08	0.29	0.09	2234.75
2	0.13	0.06	0.23	0.07	1488.87
3	-0.10	0.04	0.03	0.07	568.49
4	-0.13	0.03	-0.03	0.05	403.54
5	-0.13	0.10	-0.12	0.16	3494.7
6	-0.01	0.05	0.17	0.07	991.67
7	-0.02	0.05	0.14	0.06	1130.19
8	-0.02	0.09	0.06	0.13	3934.44

Table 5.9: The fit results in case the eight combinations of table 5.7 with the two additional fit parameters δ_p and δ_d.

5.3.2 Results of the fits

The two best parameter solutions are first plotted into the E, B-graphs. The graphs show nicely that several energy curves intersect with the measured resonance positions. With the help of these figures the remaining resonances in the lowest entrance channel are assigned. The figures on which the assignments are based, are placed into appendix C.
There are two possible scenarios which explain the resonance spectrum. The first best scenario is based on case of fit number 2 and second on fit number 4 of the previous subsection; respectively they will be referred to as final scenario one and two.

Final scenario one

The identification of the resonance spectrum in the lowest energy channels is shown in table 5.10, which are based on the E, B-graphs of fit case nr 2 (appendix C). The obtained assignment of resonances is fitted twice, once without and once with adding the correction parameters for the centrifugal barrier shift. However the latest three obtained resonances (indicated by the bold representation) are not considered for the fit, as their position is not determined as accurate as the others.
The results are shown in table 5.11 and 5.12. For the values of the last fit, the background scattering length of the singlet and triplet potentials are determined as $a_S = -3.03 \pm 0.66 a_0$ and $a_T = 0.53 \pm 0.41 a_0$.

M_F 1/2		M_F 3/2		M_F 5/2	
B_0 [G]	energy curve	B_0 [G]	energy curve	B_0 [G]	energy curve
771.8	d7	745.2	s1	1575.8	s1
822.9	s1	759.0	d6		
1596.75	4s	795.2	s2		
1716	5s	1510.4	p6		
-852.0	d7	1596.5	p7		
-1566.3	p7	1715.6	s5		
-1597	p8	1908.9	s6		
-1717.3	s4	2046.9	s7		
		-913.2	d4		
		-1720	p5		

Table 5.10: The assignment of energy curves to the resonances measured in the lowest entrance channels, in case of final scenario one.

ϵ_S [GHz]	$\Delta\epsilon_S$ [GHz]	ϵ_T [GHz]	$\Delta\epsilon_T$ [GHz]	η	$\Delta\eta$	χ^2 [G^2]
-5.86	0.10	-5.75	0.07	0.73	0.07	18242.7

Table 5.11: Resonance fit of final scenario one for the three fit parameters.

The best parameter values to describe the system are given by table 5.12. The system is plotted in the E, B-graphs figure 5.13, in which the final result of this scenario is presented.

ϵ_S [GHz]	$\Delta\epsilon_S$ [GHz]	ϵ_T [GHz]	$\Delta\epsilon_T$ [GHz]	η	$\Delta\eta$
-6.06	0.06	-5.71	0.04	0.77	0.05
δ_p [GHz]	$\Delta\delta_p$ [GHz]	δ_d [GHz]	$\Delta\delta_d$ [GHz]	χ^2 [G^2]	
0.14	0.06	0.24	0.06	5684.59	

Table 5.12: Resonance fit of final scenario one with the additional fit parameters

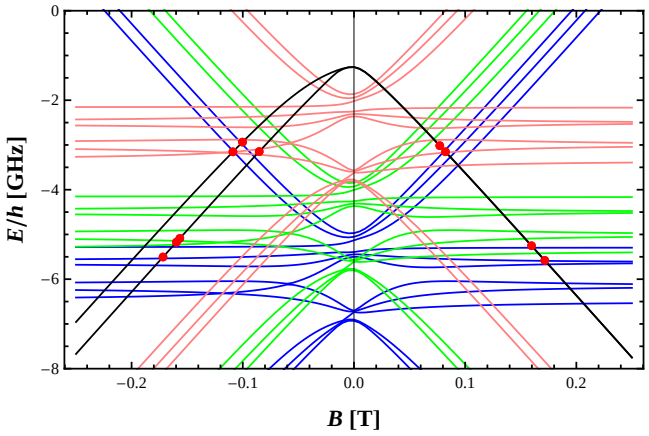

(a) The $M_F = 1/2$ channel

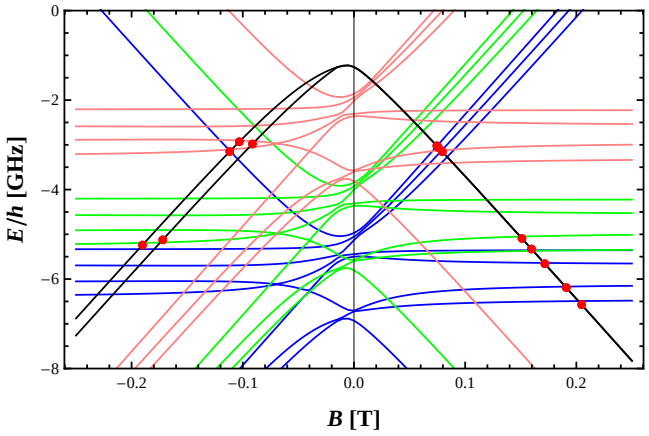

(b) The $M_F = 3/2$ channel

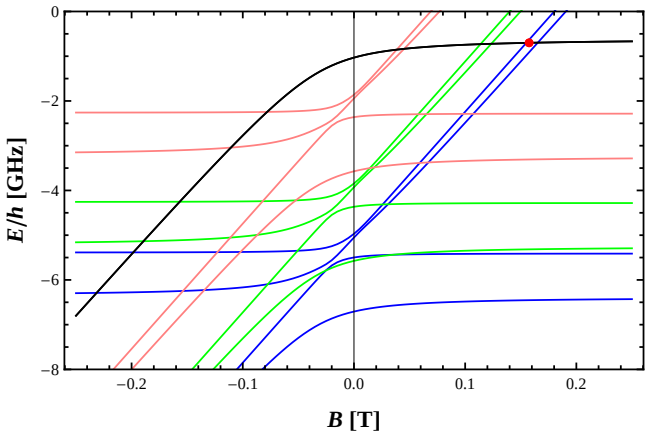

(c) the $M_F = 5/2$ channel

Figure 5.13: The E, B-graphs for the best fit parameters of final scenario one (table 5.12)

Final scenario two

Based on the fit nr. 4, the identification of the resonance spectrum can be made for the final second scenario. This is shown for the resonances in the lowest entrance channels by table 5.13, which is based on the E, B-graphs of fit case nr 4 (appendix C).
Again the resonances are fitted twice, the results of both fits are shown in table 5.14 and 5.15. For the values of the last fit, the background scattering length of the singlet and triplet bound-state was obtained at $a_S = -6.17 \pm 0.35 a_0$ and $a_T = -7.34 \pm 0.36 a_0$.

M_F 1/2		M_F 3/2		M_F 5/2	
B_0 [G]	energy curve	B_0 [G]	energy curve	B_0 [G]	energy curve
771.8	p1	745.2	d4	1575.8	p2
822.9	p2	759.0	p2		
1596.75	p5	795.2	p3		
1716	p7	1510.4	p4		
-852.0	d4	1596.5	p5		
-1566.3	p3	1715.6	p6		
-1597	p4	1908.9	s5		
-1717.3	p6	2046.9	s6		
		-913.2	d2		
		-1720	p2		

Table 5.13: The assignment of energy curves to the resonances measured in the lowest entrance channels, in case of final scenario two

ϵ_S [GHz]	$\Delta\epsilon_S$ [GHz]	ϵ_T [GHz]	$\Delta\epsilon_T$ [GHz]	η	$\Delta\eta$	χ^2 [G^2]
-6.35	0.06	-6.52	0.03	0.56	0.06	6090.92

Table 5.14: Resonance fit of final scenario two for the three fit parameters.

ϵ_S [GHz]	$\Delta\epsilon_S$ [GHz]	ϵ_T [GHz]	$\Delta\epsilon_T$ [GHz]	η	$\Delta\eta$
-6.34	0.03	-6.42	0.03	0.55	0.04
δ_p [GHz]	$\Delta\delta_p$ [GHz]	δ_d [GHz]	$\Delta\delta_d$ [GHz]	χ^2 [G^2]	
-0.1	0.03	0.04	0.04	1435.81	

Table 5.15: Resonance fit of final scenario two with the additional fit parameters.

The final result given in table 5.15 of this scenario is plotted for each channel. Those graphs are shown in figure 5.14.

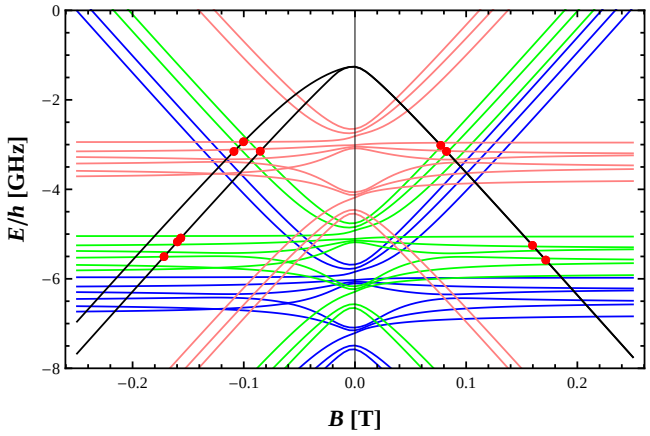

(a) The $M_F = 1/2$ channel

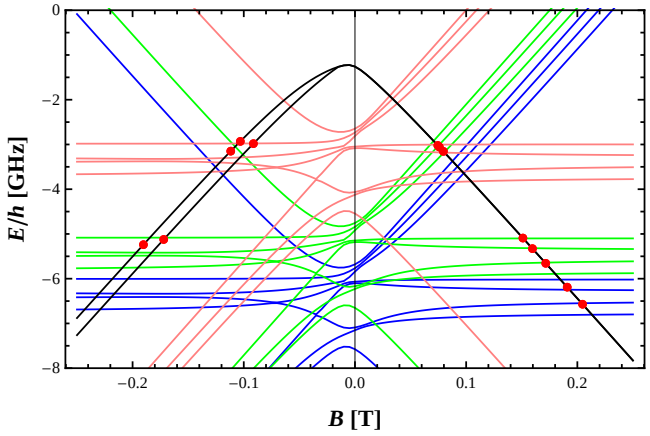

(b) The $M_F = 3/2$ channel

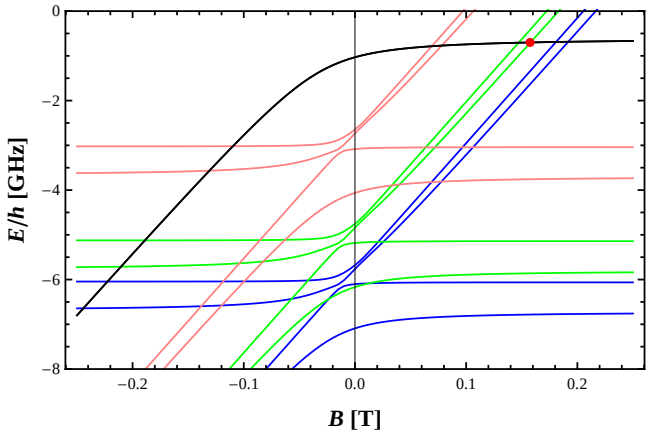

(c) the $M_F = 5/2$ channel

Figure 5.14: The E, B-graphs for the best fit parameters of final scenario two (table 5.15)

Comparison

The figures of final scenario one show a nice explanation for the measured resonances in the energetically higher positioned entrance channels. However the drawback of this scenario is that the positions of the 2^{nd} and 8^{th} resonance in the $M_F = 3/2$ channel by positive magnetic fields are not well described.
The second scenario does not well explain the resonances measured in the higher entrance channels. However a better fit result, smaller χ^2, was obtained for this scenario than that of the first.

5.3.3 Comparison of the calculated and measured widths

The field width of the resonances are determined as described in section 4.3.2. This method is only valid in case of s-waves. Both final solutions use s-waves to explain the resonance spectrum. It is expected that the resonances with the broadest widths are most easily measured.
The different channels are scanned for resonances by different range of magnetic fields. It is only expected that a broad resonance is measured as it is positioned into the scanned field range. This can be compared to the experimental results. Another approach to evaluate the two scenarios is to compare the resonance hierarchy according to the field width and the inverse hold time (stated in table 5.2). They should lead to the same result.

Final scenario one

The absolute values for the field width in case of scenario one are shown in table 5.16. The resonance positions that do fall into the measured magnetic field areas are underlined. The measured area in the $M_F = 5/2$ for positive magnetic fields was not stated in data sheets from Heidelberg. Therefore we will leave this channel ($B > 0$) for what is and do not incorporate it further in the field width analysis.
So lets examine the channel of $M_F = 1/2$, the scenario predicts three measured s-wave resonances by positive magnetic fields and one by negative fields. Those would be caused by the energy curves: s1, s4 and s5 for $B > 0$ and $s4$ in case $B < 0$. The inverse hold times would suggests a hierarchy in the field width from high to low: s4 ($B > 0$), s4 ($B < 0$) and s1 ($B < 0$). The hold time of the resonance assigned to the s5 is not known.
The field width of the resonances positioned in the measured areas are calculated and stated in table 5.16. The hierarchy in those resonances according to their field width from high to low, is: s4 ($B < 0$), s5 ($B > 0$), s2 ($B > 0$), s4 ($B > 0$), s1 ($B < 0$), s1 ($B > 0$), s5 ($B < 0$), s3 ($B < 0$), s2 ($B < 0$) and s3 ($B > 0$). This hierarchy does not correspond to a ranking of the inverse holding time. The 4 measured resonances belong to the broadest five resonances, however the question arises why the s2 ($B > 0$) is not measured.

In the channel of $M_F = 3/2$ all the calculated s-wave resonances are positioned in the measured area by positive magnetic fields (table 5.16). In case of negative magnetic field there is only one s-wave resonance which qualifies to be measured. Scenario one, identifies five resonances to be caused by s-waves in this channel, those are the s1, s2, s5, s6 and s7 for $B > 0$.

The field width hierarchy form high to low values is given by the series, s6 ($B > 0$), s5 ($B > 0$), s7 ($B > 0$), s1 ($B < 0$), s3 ($B > 0$), s4 ($B > 0$), s2 ($B > 0$) and s1 ($B > 0$). From the widths ranking it would be most likely that the first five would have been found. The first do correspond to the measured resonances. However resonances are also measured for which the smallest width is obtained and some with a broader width are not found.
However in case those broader widths were missed the ranking of the resonances according to their inverse hold time should at least correspond to the field width series. The ranking from large to small values for the inverse hold times gives the series s1, s7, s3, s5 and s6. However one must conclude that the field width hierarchy does also not correspond to the hierarchy of resonances obtained by the inverse hold times.

As last the $M_F = 5/2$ channel is evaluated. In this channel is one resonance measured by positive magnetic fields, it is assumed to be caused by the first s-wave. The measured area

M_F 1/2					
$B < 0$			$B > 0$		
nr	B_0 [G]	ΔB[G]	nr	B_0 [G]	$\Delta B[G]$
s1	-895.95	0.000271	s1	814.94	0.000032
s2	-965.29	$7.883 * 10^{-7}$	s2	866.53	0.000307
s3	-1635.58	$3.516 * 10^{-6}$	s3	936.42	$5.329 * 10^{-7}$
s4	-1729.09	0.008167	s4	1613.38	0.000272
s5	-1785.24	$4.082 * 10^{-6}$	s5	1719.73	0.007633
s6	-1919.48	$1.123 * 10^{-7}$	s6	1748.1	$1.138 * 10^{-6}$
s7	-1991.07	0.037746	s7	1901.4	$6.122 * 10^{-6}$
s8	-2038.95	$4.925 * 10^{-8}$	s8	1945.16	0.039415
			s9	2065.83	0.001066

M_F 3/2					
$B < 0$			$B > 0$		
nr	B_0 [G]	ΔB[G]	nr	B_0 [G]	$\Delta B[G]$
s1	-1044.8	0.000439	s1	746.63	$3.736 * 10^{-7}$
s2	-1796.58	$5.170 * 10^{-8}$	s2	786.75	0.000031
s3	-1931.29	0.000044	s3	838.65	0.000339
s4	-2059.35	0.070020	s4	1606.93	0.000271
s5	-2165.88	$9.065 * 10^{-6}$	s5	1709.61	0.006610
			s6	1901.62	0.041625
			s7	2018.40	0.001030

M_F 5/2					
$B < 0$			$B > 0$		
nr	B_0 [G]	ΔB[G]	nr	B_0 [G]	$\Delta B[G]$
s1	-1984.6	0.010403	s1	1550.13	0.001210
s2	-2315.15	0.050831	s2	1653.62	0.045344

Table 5.16: The calculated resonance positions B_0 for the s-waves with corresponding field widths ΔB of final scenario one. The underlined values for B_0, indicate those resonances which are positioned in the measured magnetic field range.

by positive magnetic field was not listed, however for negative magnetic fields it was. One resonance in the measured area was found with a field width larger than the s1. Therefore this resonance was expected to be measured if this scenario describes the ^{23}Na^{6}Li system.

Final scenario two

Again all the s-wave resonances are underlined for which their position is stated in the measured magnetic field range (table 5.17). In total there are only six s-waves resonances which could have been measured. From those six, two resonances have a large magnetic field width. Those are the 5^{th} and the 6^{th} s-wave in the $M_F = 3/2$ channel.
These two partial waves are the only s-waves which scenario two predicts that have been measured. So far this scenario corresponds to the field width picture.
However when comparing the ranking of the resonances according to the field width, it

M_F 1/2					
$B < 0$			$B > 0$		
nr	B_0 [G]	ΔB[G]	nr	B_0 [G]	$\Delta B[G]$
s1	-1034.22	0.000138	s1	$\underline{949.84}$	0.000019
s2	-1104.55	$2.870 * 10^{-8}$	s2	$\underline{1005.48}$	0.000153
s3	-1884.27	$5.710 * 10^{-7}$	s3	1076.29	$3.191 * 10^{-7}$
s4	-1956.74	0.152547	s4	1859.72	0.003623
s5	-2009.03	$2.332 * 10^{-6}$	s5	1943.63	0.165839
s6	-2056.06	$2.156 * 10^{-6}$	s6	1968.13	$7.496 * 10^{-7}$
s7	-2122.88	0.130167	s7	2041.34	$7.394 * 10^{-6}$
s8	-2158.54	$1.303 * 10^{-6}$	s8	2080.42	0.12353
			s9	2173.71	0.004522
M_F 3/2					
$B < 0$			$B > 0$		
nr	B_0 [G]	ΔB[G]	nr	B_0 [G]	$\Delta B[G]$
s1	-1185.01	0.000181	s1	$\underline{876.88}$	$2.114 * 10^{-7}$
s2	-2042.86	$3.210 * 10^{-6}$	s2	$\underline{922.00}$	0.000019
s3	-2164.75	0.404625	s3	$\underline{978.00}$	0.000167
s4	-2191.58	0.026423	s4	$\underline{1847.61}$	0.003631
s5	-2290.3	$7.568 * 10^{-8}$	s5	$\underline{1930.69}$	0.182622
			s6	$\underline{-2039.25}$	0.113698
			s7	$\underline{-2131.57}$	0.004275
M_F 5/2					
$B < 0$			$B > 0$		
nr	B_0 [G]	ΔB[G]	nr	B_0 [G]	$\Delta B[G]$
s1	-2226.44	0.169075	s1	1808.23	0.002321
s2	-2444.00	0.205086	s2	1918.66	0.098112

Table 5.17: The calculated resonance positions B_0 for the s-waves with corresponding field widths ΔB of final scenario two. The highligthed values for B_0, indicate those resonances which are positioned in the measured magnetic field range.

is not consistent with the inverse of the hold times. The hold times predict that the 7^th resonance has a smaller field width than the 8^{th} resonance in the channel. Table 5.17 shows that the 7^{th} resonance has a broader width than the 8^{th} resonance (caused by relatively s5 and s6).

Chapter 6

Discussion and Conclusion

In this thesis the Feshbach resonance spectrum of the ^{23}Na^{6}Li system is examined. In the group of prof. Oberthaler at the university of Heidelberg, 24 Feshbach resonances in this system were measured.
Our approach was to analyze these Feshbach resonances by using the Asymptotic Bound-state model (ABM). Due to the inaccurate inner range potentials, the model has three free input parameters namely: the relative s-wave bound state energy with a singlet electron spin configuration (ϵ_S) and a triplet electron spin configuration (ϵ_T) and the Frank-Condon factor η for $S' \neq S$. The goal was to find these three parameters which make the model consistent with the measured resonance positions.
The system has been analyzed for the resonances found in the energetically lowest entrance channels. Resonances in other channels were also measured, however, we excluded these since the ABM does not anticipate on possible threshold effects when a bound state is actually unbound. This happens an ABM solution passes a second threshold. In the end two possible solutions have been found. The best results were obtained if an error in the centrifugal barrier shift was incorporated. It suggests that the energy shift between partial waves induced by the centrifugal barrier, is not precise enough determined. The reason for this is probably that the long range potential is not yet accurate enough available. The best fit results for the two scenarios, for the three parameters combined with two additional barrier shift parameters (δ_p for p-waves and δ_d for d-waves):

Final scenario one: $\epsilon_S = -6.06$, $\epsilon_T = -5.71$, $\eta = 0.77$, $\delta_p = 0.14$ and $\delta_d = 0.24$
Final scenario two: $\epsilon_S = -6.34$, $\epsilon_T = -6.42$, $\eta = 0.55$, $\delta_p = -0.1$ and $\delta_d = 0.04$

The two scenario's, each have their pro's and con's. In *final scenario one* the resonances in the energetically higher positioned entrance channels are nicely explained, even though they were not considered in the analysis. However the fit values have a relative large χ^2, almost four times larger than scenario two. Next to that, the calculated field width for the predicted s-wave resonances does not give a consistent story when compared to the measurement. One would expect that in the scanned magnetic field range, the resonances with the broadest field width would have been observed. However this scenario states, that a few of those resonances are missed. However, this is inconsistent with that some resonances with smaller widths are measured and in general when the hierarchy in field width of the

measured resonances is compared to the hierarchy based on the inverse measured hold times no consistency is found.

The resonances obtained with *final scenario two*, describe the measured resonance positions better which is reflected in a smaller χ^2. However this scenario does not explain the resonances measured in the energetically higher positioned channels.
For these free parameters only six s-wave resonances are positioned in the scanned magnetic field range. This scenario states that only two measured resonances are caused by s-waves and the other resonances are caused by p- and d-waves. These two resonances correspond to the calculated resonances with the broadest field width of the six. So far the resonance spectrum totally agrees with scenario two. However when evaluating the hierarchy of the field width in comparison with the inverse hold time of the two resonances the results do not agree.

It is interesting to compare these two scenarios to other experimental results found in Heidelberg for the ^{6}Li^{23}Na mixture, which are not connected to Feshbach resonances. From the overlap between the clouds of ^{6}Li and ^{23}Na, an off-resonant scattering length equal to $a_{bg} = -7$ a$_0$ was found. Also, from the non-resonant background losses, a value for the difference between the singlet and triplet scattering lengths could be estimated: $|a_S - a_T| = 3 \pm 1$ a$_0$. This information, in combination with the Feshbach resonance analysis, allows us to make some statements on the accuracy of the long-range part of the potential, in particular on the long-range C_6 coefficient. In table 6.1 the values of the ^{6}Li^{23}Na singlet and scattering length, and the change of the p-wave barrier shift compared to the default value C_6^0 are given, for a 25% variation of this value.

C_6	a_S (a$_0$)	a_T (a$_0$)	δ_p (GHz)
$0.75C_6^0$	6	8	+0.07
C_6^0	-3	1	0
$1.25C_6^0$	-13	-8	-0.05

Table 6.1: Singlet and triplet scattering length a_S and a_T and correction to the p-wave barrier shift δ_p, calculated for three different values of C_6. The interaction parameters are chosen from *final scenario one*, and the calculation is done following the lines in chapter 3.

For *final scenario one*, we find $a_S = -3.03$ a$_0$ and $a_T = 0.53$ a$_0$. The difference is consistent with the measured value, however, the values are more than a factor of two different from the background value. From table 6.1 we can see that a 25% larger value of C_6 brings the scattering lengths to the measured value of a_{bg}. However, this change in C_6 results in a shift of the barrier shift which is not consistent with the fitted δ_p in *final scenario one*, as a positive shift is required. However the shift is consistent with the fitted δ_p in *final scenario two*.
For *final scenario two*, we find $a_S = -6.17$ a$_0$ and $a_T = -7.34$ a$_0$. The difference is now not consistent with the measured value, however, the two values are consistent with the measured background value. Therefore, for this scenario a change of C_6 would not be needed.
Although a 25% variation of C_6 does not yet give a fully consistent picture between measurements and the analysis, it can be concluded that within these variations, the from analysis

obtained values of scattering lengths and barrier shifts could be obtained. However, it does not yield yet a preference for one of the two final scenarios.

Outlook

Recently, coupled channels calculations for the s-wave Feshbach resonances have been performed by Eberhard Tiemann. He concluded that it is hard to explain the five last resonances in the $M_F = 3/2$ channel ($B > 0$). Also he suggested that the long range potential was not very accurate and more work should be done to obtain better long-range coefficients.
The most promising thing what could now be done is to search experimentally for a broad p-wave splitting. This p-wave splitting originates from the weak magnetic dipole-dipole interaction which splits the p-wave resonance position according to its two projections $m_l = \pm 1$ and $m_l = 0$[19]. Within a coupled channels calculation, this interaction is incorporated and one can search for the broadest p-wave splitting in both scenarios. All resonances should again be carefully measured in search for this duplicate structure. This way some resonances can be identified as p-waves and could confirm one of the two scenario's.

Appendix A

Justification of inner potential adjustment

The fitted inner potential does not correspond to the data points for small values of r. To see if these adjustments in the potential are permitted, the influence of the adjustments on the barrier shift is studied. For this five different inner potential candidates are used:

- Extrapolation of the interpolation function through all data points (P1)
- The potential curve which was fitted through the data points for $r > 4.15$ a_0 (P2)
- A linear potential curve with gradient (-237500, -250000 and -275000 GHz/ a_0) till 4.15 a_0 and beyond this distance the interpolation function is used (P3)

The obtained inner potentials are shown in figure A. The barrier shift found for the five scenarios, is shown below.

The maximum difference in the barrier shift with Swave Energy of -8 GHz is 7 MHz. So the adjustments to the inner potential do not have a great influence on the shift barrier, therefore the P2 potential is used without much concern in further calculations.

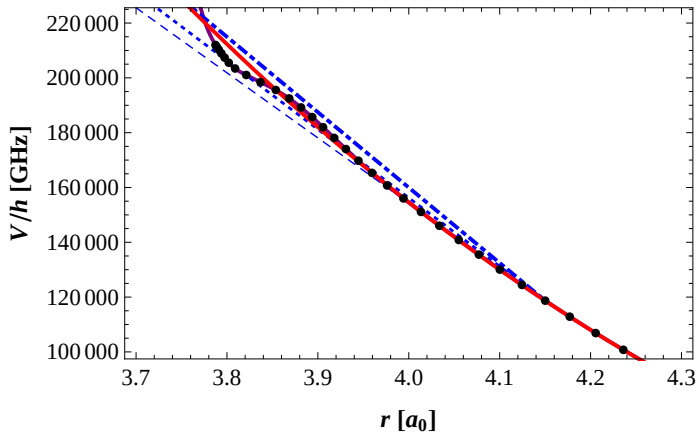

Figure A.1: The five different variations for the inner potential, with purple P1, Red P2 and the three Blue P3.

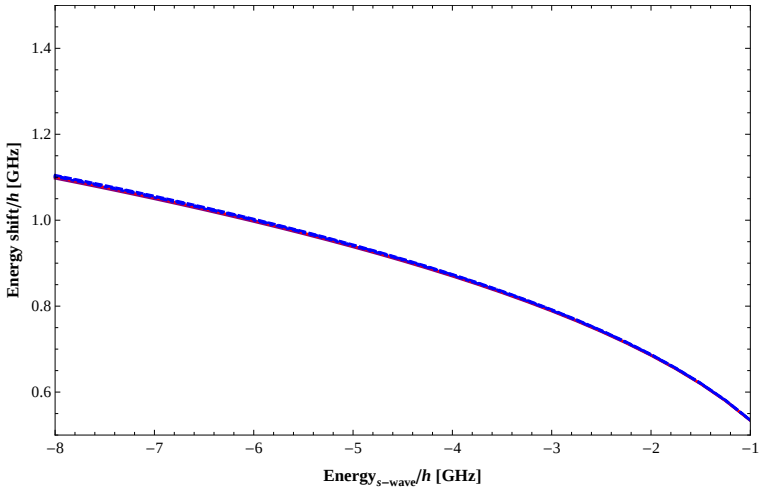

Figure A.2: The energy barrier shift for the p-waves as function of the singlet bound state energy.

Appendix B

Additional information of chapter 5

B.1 D-waves solutions for the first three resonances of the $M_F = 3/2$ channel

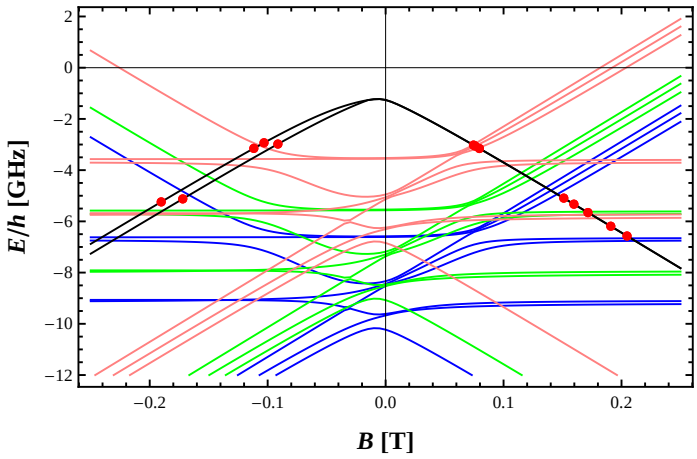

Figure B.1: The $M_F = 3/2$ channel with the parameter combination $\epsilon_S = -6.73$ GHz, $\epsilon_T = -9.077$ GHz and $\eta = 0.741$.

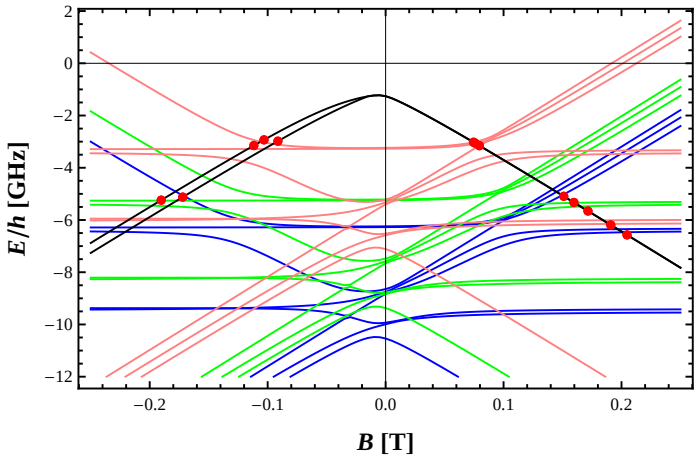

Figure B.2: The $M_F = 3/2$ channel with the parameter combination $\epsilon_S = -6.73$ GHz, $\epsilon_T = -9.077$ GHz and $\eta = 0.741$.

B.2 S-waves solutions for first three resonances of the $M_F = 3/2$ channel

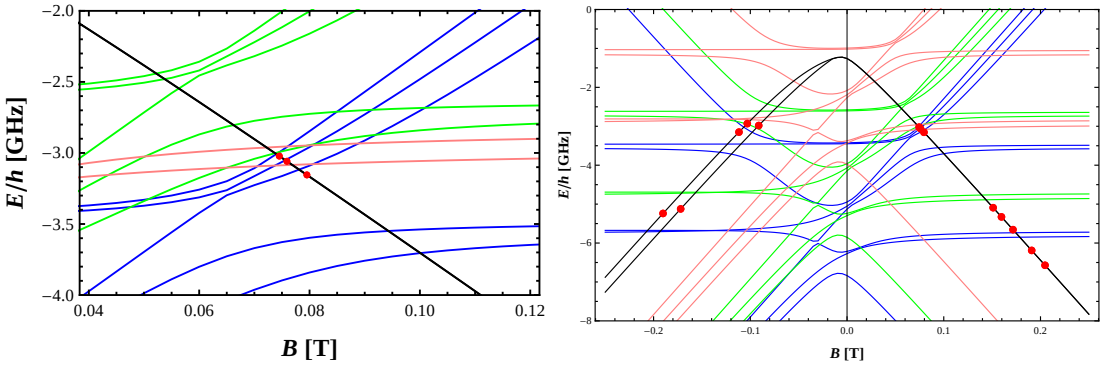

Figure B.3: The $M_F = 3/2$ channel with the parameter combination $\epsilon_S = -3.429$ GHz, $\epsilon_T = -5.767$ GHz, $\eta = 0.686$.

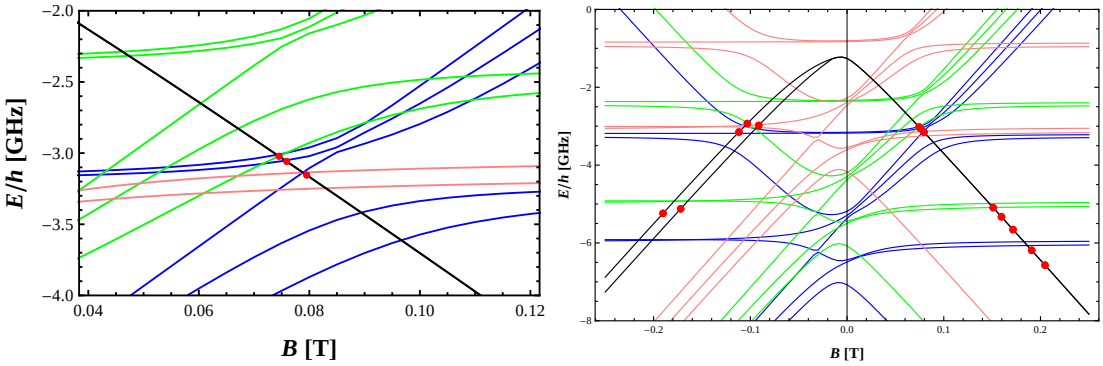

Figure B.4: The $M_F = 3/2$ channel with the parameter combination $\epsilon_S = -3.273$ GHz, $\epsilon_T = -5.926$ GHz, $\eta = 0.680$.

B.3 P-waves solutions for the first three resonances of the $M_F = 3/2$ channel

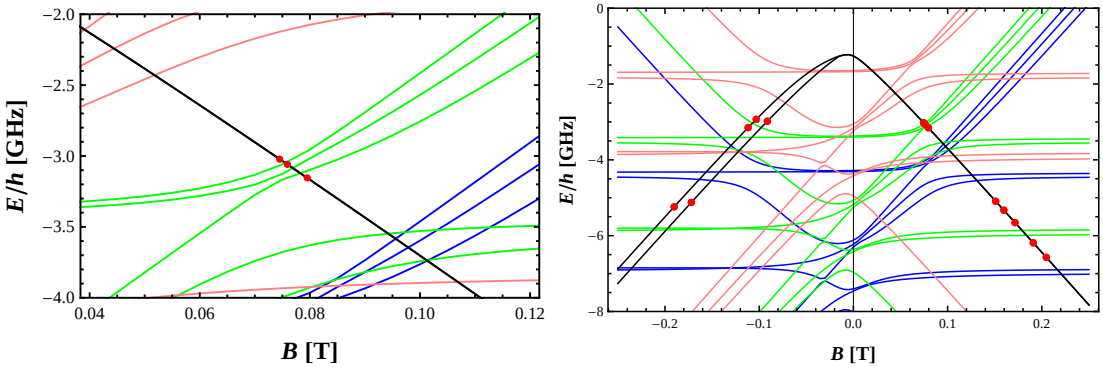

Figure B.5: The $M_F = 3/2$ channel with the parameter combination $\epsilon_S = -4.440$ GHz, $\epsilon_T = -6.86$ GHz, overlap $= 0.767$.

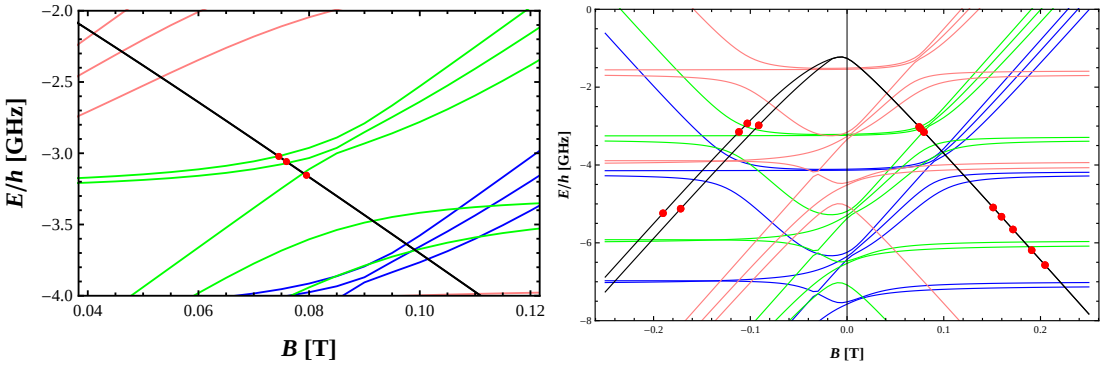

Figure B.6: The $M_F = 3/2$ channel with the parameter combination $\epsilon_S = -4.254$ GHz, $\epsilon_T = -6.985$ GHz, $\eta = 0.773$.

B.4 Lower border of the singlet energy

The lower bound is created by shifting the singlet energy from -13 GHz upwards by the four options of the triplet energy (overlap 1). By eye one can see that till -8 GHz it is safe to say, no solutions can be found. This is shown in the figures below, for each triplet case the singlet case of -13 GHz and -8 GHz are plotted.

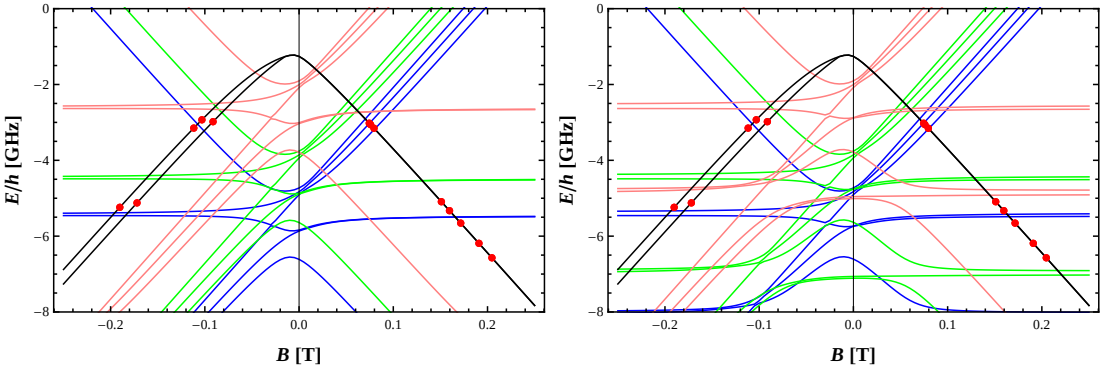

Figure B.7: The $M_F = 3/2$ channel with the parameter combinations, with left $\epsilon_S = -13$ GHz, $\epsilon_T = -5.47$ GHz, overlap $= 1$ and for the right graph $\epsilon_S = -8$ GHz, $\epsilon_T = -5.47$ GHz, $\eta = 1$.

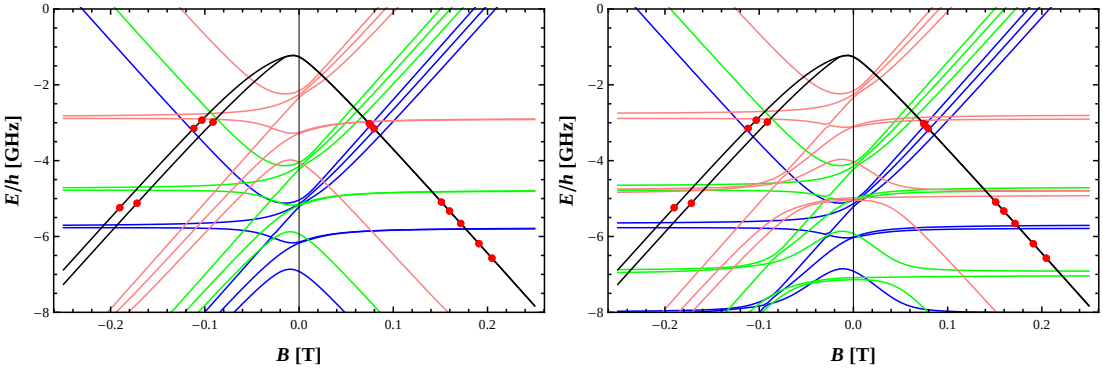

Figure B.8: The $M_F = 3/2$ channel with the parameter combinations, with left $\epsilon_S = -13$ GHz, $\epsilon_T = -5.78$ GHz, overlap $= 1$ and for the right graph $\epsilon_S = -8$ GHz, $\epsilon_T = -5.78$ GHz, $\eta = 1$.

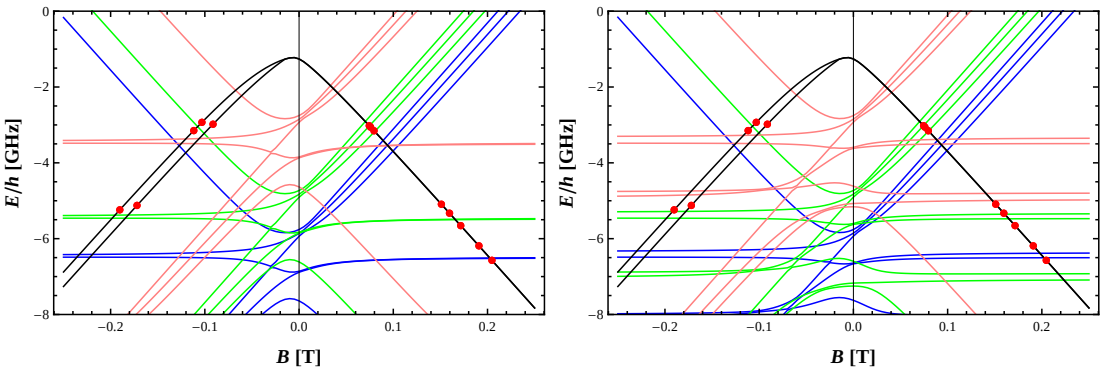

Figure B.9: The $M_F = 3/2$ channel with the parameter combinations, with left $\epsilon_S = -13$ GHz, $\epsilon_T = -6.50$ GHz, overlap $= 1$ and for the right graph $\epsilon_S = -8$ GHz, $\epsilon_T = -6.50$ GHz, $\eta = 1$.

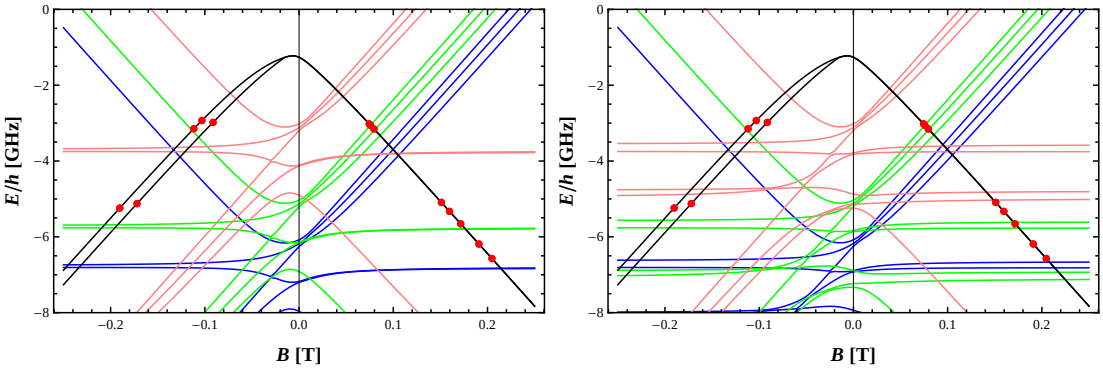

Figure B.10: The $M_F = 3/2$ channel with the parameter combinations, with left $\epsilon_S = -13$ GHz, $\epsilon_T = -6.82$ GHz, overlap $= 1$ and for the right graph $\epsilon_S = -8$ GHz, $\epsilon_T = -6.82$ GHz, $\eta = 1$.

Appendix C

The assignment of the resonance spectrum

There are two final fit scenarios gained for a selected set of resonances. The key question is how does the result looks like in the light of the whole resonance spectrum. This is shown in figure C.4 The left graphs are those graphs obtained by fit scenario one and the right column of graphs by fit scenario two.

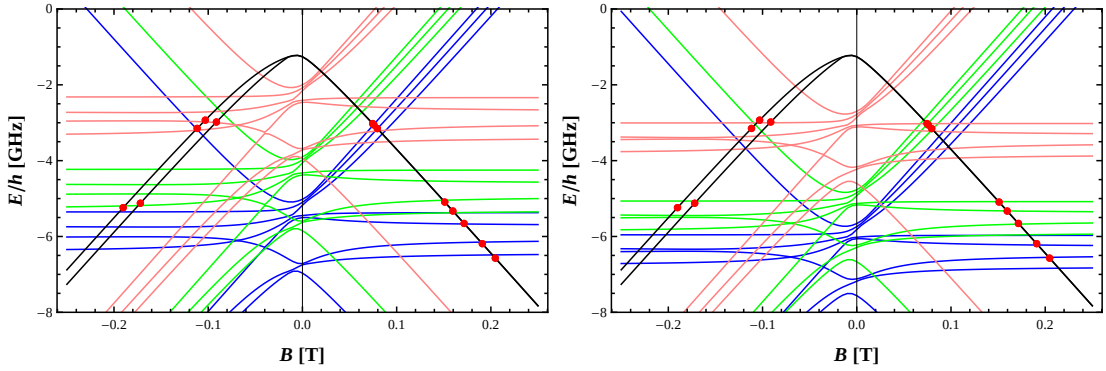

Figure C.1: $MF = 1/2$ channel

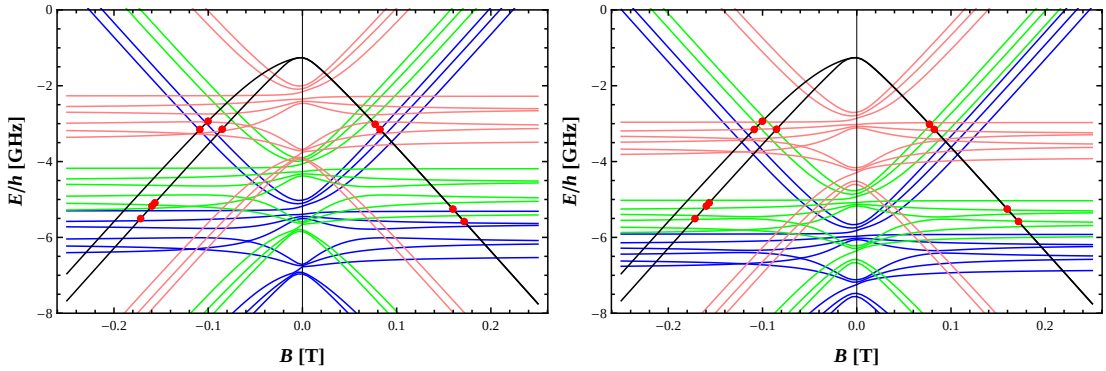

Figure C.2: $MF = 3/2$ channel

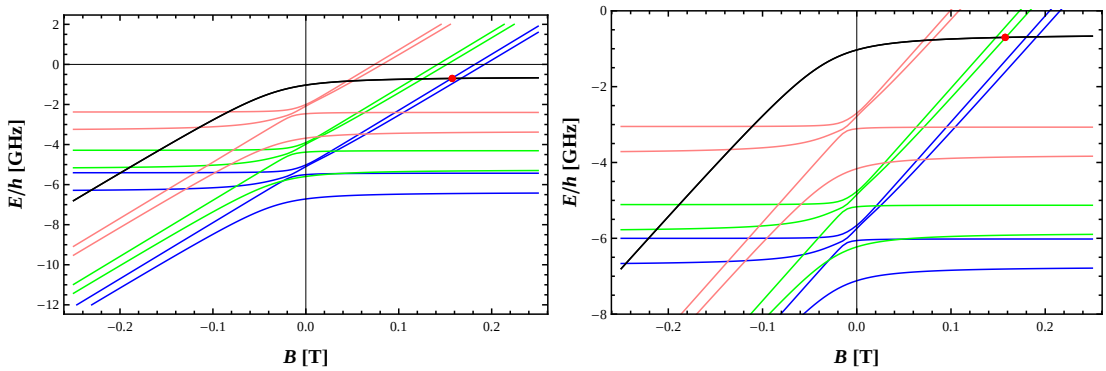

Figure C.3: $MF = 5/2$ channel

Figure C.4: The channel overviews for the two fit scenarios based on eight resonances. The left column is obtained by scenario one the right column by scenario two. In each row the same M_F channel is viewed. Scenario one has the parameter combination $\epsilon_S = -6.07$ GHz, $\epsilon_T = -5.76$ GHz, overlap $= 0.75$, $\delta_p = 0.13$ GHz and $\delta_d = 0.23$ and scenario two $\epsilon_S = -6.34$ GHz, $\epsilon_T = -6.40$ GHz, overlap $= 0.61$, $\delta_p = -0.13$ GHz and $\delta_d = -0.03$.

Bibliography

[1] C.A. Stan, M.W. Zwierlein, C.H. Schunck, S.M.F. Raupach, and W. Ketterle. Observation of feshbach resonances between two different atomic species. *Phys. Rev. Lett.*, 93: 143001, 2004.

[2] M. Gacesa, P.Pellegrini, and R. Cote. Feshbach resonances in ultracold ^{6,7}li+ ^{23}na atomic mixtures. *Phys. Rev. A*, 78:010701, 2008.

[3] C.E. Fellows. The nali electronic ground-state dissociation limit. *J. Chem. Phys.*, 94(9): 5855–5864, 1991.

[4] T.G. Tiecke, M.R. Goosen, J.T.M. Walraven, and S.J.J.M.F. Kokkelmans. Asymtotic-bound-state model for feshbach resonances. *Phys. Rev. A*, 00:002700, 2010.

[5] C. Chin. Feshbach resonances in ultracold gases. *Rev. Mod. Phys.*, 82:1225, 2010.

[6] Maikel Robert Goosen. *Universal relations between Feshbach resonances and molecules.* PhD thesis, Technische Universiteit Eindhoven, 2011.

[7] S. Knoop, T. Schuster, A. Trautmann, J. Appmeier, M.K. Oberthaler, E. Tiesinga, and E. Tiemann. Feshbach spectroscopy and analysis of the interaction potential of ultracold sodium. *Phys. Rev. A*, 83:042704, 2011.

[8] E.Wille, F.M.SpiegelHalder, G. Kerner, D.Naik, A. Trenkwalder, G. Hendl, F.Schreck, R.Grimm, T.G. Tiecke, J.T.M. Walraven, S.J.J.M.F. Kokkelmans, E.Tiesinga, and P.S. Julienne. Exploring an ultracold fermi-fermi mixture: Interspecies feshbach resonances and scattering properties of ^{6}li and ^{4}0k. *Phys. Rev. Lett.*, 100:053201, 2008.

[9] R.V. Krems, W.C. Stwalley, and B. Friedrich. *Cold molecules: theory, experiment, applications.* Boca Raton: Taylor and Francis, 2009.

[10] David J. Griffiths. *Introduction to Quantum Mechanics.* Pearson Prentice Hall, 2005.

[11] Eric van Kempen. *Feshbach resonances in cold atomic gases.* PhD thesis, Technische Universiteit Eindhoven, 2006.

[12] P. J. Mohr, B.N. Taylor, and D.B. Newell. *CODATA Recommended Values of the Fundamental Physical Constants: 2006.* NIST, 2006.

[13] B.H. Bransden and C.J. Joachain. *Physics of Atoms and Molecules.* Pearson Education Limited, 2003.

[14] B.J. Verhaar, E.G.M. van Kempen, and S.J.J.M.F. Kokkelmans. Predicting scattering properties of ultracold atoms: Adiabatic accumulated phase method and mass scaling. *Phys. Rev. A*, 79:032711, 2008.

[15] B. Marcelis, E.G.M. van Kempen, B.J. Verhaar, and S.J.J.M.F. Kokkelmans. Feshbach resonances with large background scattering length: Interplay with open-channel resonances. *Phys. Rev. A*, 70:012701, 2004.

[16] A.J. Moerdijk, B.J. Verhaar, and A. Axelsson. Resonances in ultracold collisions of ^{6}li, ^{7}li and ^{2}3na. *Phys. Rev. A*, 51:4853, 1995.

[17] H. Feshbach. *Theoretical nuclear physics*. Wiley-Interscience, 1992.

[18] Dževad Belkić. *Principles of quantum scattering theory*. Institute of Physics Publishing, 2004.

[19] C. Ticknor, C.A. Regal, D.S. Jin, and J.L. Bohn. Multiplet structure of feshbach resonances in nonzero partial waves. *Phys. Rev. A*, 69:042712, 2004.